ABSTRACT

THE FEYNMAN-x DEPENDENCE OF $D^{\pm}$ MESONS IN pi^{-}-NUCLEON INTERACTIONS

Zhongxin Wu
Yale University
December 1991

The x_F distribution of $D^{\pm}$ was measured from Fermilab experiment E769 using the decay mode $D^{\pm} \rightarrow K^{\mp}\pi^{\pm}\pi^{\pm}$. The experiment was performed using a 250 GeV tagged hadron beam incident on thin target foils of Be, Al, Cu and W. The measurement was based 554 ± 33 reconstructed $D^{\pm}$ mesons from 200 million triggers induced by a π^{-} beam. Fitting the distribution to the form $C(1-|x_F|)^n$, the fit parameter n was determined to be 3.21 ± 0.24. However, we observed no significant leading particle effect suggested by earlier experiments. We also observed that the x_F distribution does not dramatically depend on atomic number. Our result is consistent with the perturbative QCD predictions.

THE FEYNMAN-x DEPENDENCE OF $D^{\pm}$ MESONS IN pi^{-}-NUCLEON INTERACTIONS

A Dissertation
Presented to the Faculty of the Graduate School
of
Yale University
in Candidacy for the Degree of
Doctor of Philosophy

By
Zhongxin Wu
December 1991

Contents

List of Figures

List of Tables

Chapter 1

Hadroproduction of Charm

1.1 Introduction

Charm experiments using e^+-e^- and photon-nucleon collisions have led to significant progress[1][2][3][4] in the knowledge of both charmed particle properties and production mechanisms. In hadronic production of charm, however, it is relatively difficult to extract clean charm signals, because the charm signal relative to the background is about 1000 times smaller than in e^+-e^- collisions and 10 times smaller than in photon-nuclei interactions. As a result, the understanding of the hadroproduction of charm has been limited.

The Fermilab experiment E769 was designed to produce and reconstruct a large sample of charm events to study the hadroproduction properties including the total cross section, beam flavor dependence, atomic number dependence, x_F and p_T dependences. In this thesis, I concentrate on the x_F distribution of $D^\pm$ production in π^--nucleon collisions using the decay $D^\pm \rightarrow K^\mp\pi^\pm\pi^\pm$.

It is important to study the hadroproduction mechanisms, so we can compare the measurements with the perturbative QCD calculations. This is not only relevant for charm but also for bottom and top production, because the physical processes involved are the same.

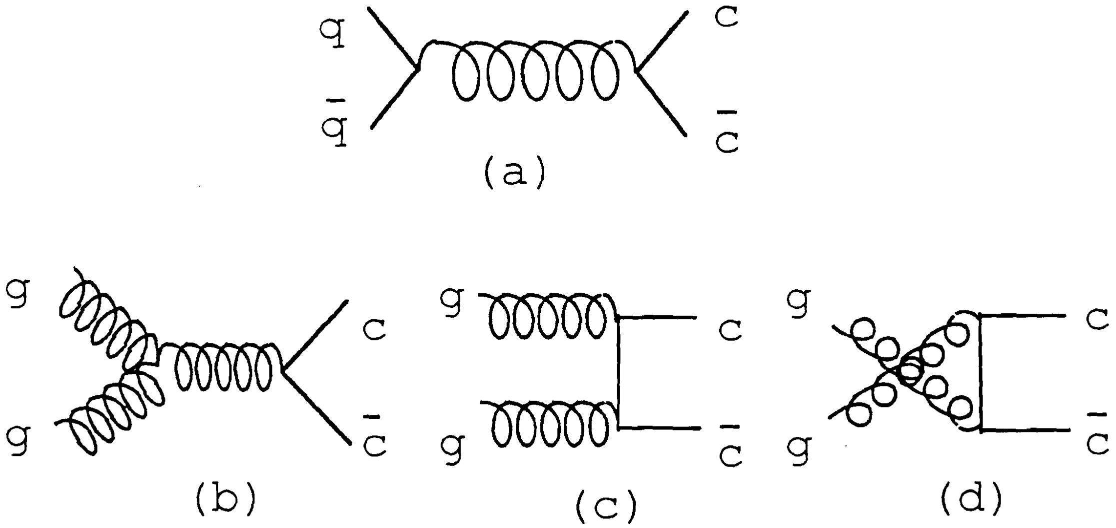

Figure 1.1: Lowest order Feynman diagrams for hadroproduction of charm (a) quark-antiquark annihilation, (b)-(d) gluon-gluon fusion.

1.2 Theory

Figure 1.1 shows the lowest order QCD diagrams ($O(\alpha_s^2)$) for the hadroproduction of charm quarks. These diagrams represent gluon-gluon fusion and quark-antiquark annihilation processes. Based on these diagrams a number of authors (Georgi, Glashow, Machacek and Nanopoulos[5], Combridge[6], Barger, Halzen and Keung[7], Ellis and Quigg[8]) calculated the total charm cross section ($\sigma(\alpha_s^2)$), and the x_F and p_T distributions.

More recently, K. Ellis, P.Nason and S. Dawson[9][10][11] have calculated the charm production cross sections including the processes of order α_s^2 and α_s^3. This calculation gives a total cross section that is three times larger than that using only the lowest order processes ($O(\alpha_s^2)$). This is discussed later in this chapter. However, both calculations give about the same dependence on x_F and p_T apart from the normalization.

An inclusive production process of a charm quark c is depicted in figure 1.2. Incident particles with momenta P_A and P_B have partons with longitudinal momentum fractions of $x_A P_A$ and $x_B P_B$. The interaction of these partons produces a $c\bar{c}$ pair.

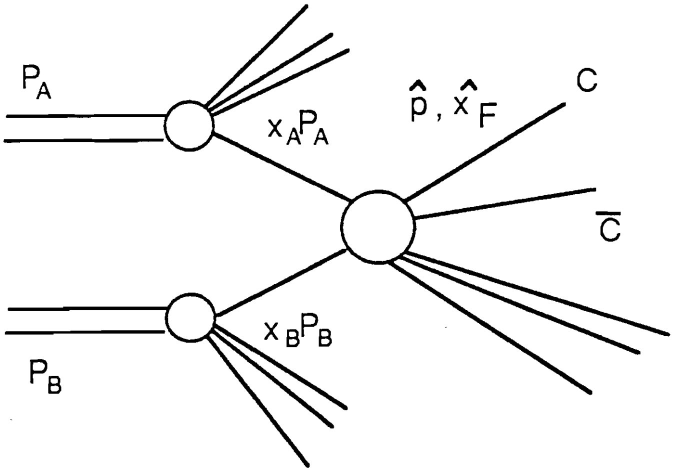

Figure 1.2: An inclusive production process of a charm quark in hadron-hadron collisions.

The c quark carries a momentum $\hat{p}$ in the parton-parton center of mass system. The QCD differential cross section $d\sigma/d\hat{x}_F$ is

$$\frac{d\sigma}{d\hat{x}_F} = \sum_{i,j} \int dx_A dx_B \left[\frac{d\hat{\sigma}_{ij}(x_A P_A, x_B P_B, \hat{p}, m_c, Q^2)}{d\hat{x}_F} \right] F_i^A(x_A, Q^2) F_j^B(x_B, Q^2), \tag{1.1}$$

where $F_i^{A,B}$ are the structure functions of light partons (gluons and light quarks and antiquarks) of A and B. $\hat{\sigma}_{ij}$ denotes the short-distance charm quark cross section of the two partons. m_c is the mass of the produced charm quark. Q is a typical transverse momentum transfer between the initial state parton and the produced charm quark. Q^2 is on the order of m_c^2. The Feynman x variable[12] $\hat{x}_F$ of the charm quark, is defined in the center of mass system as:

$$\hat{x}_F = \frac{\hat{p}_z}{p_{max}} \simeq \frac{2\hat{p}_z}{\sqrt{s}} \tag{1.2}$$

where $\hat{p}_z$ is the component of the charm quark momentum parallel to the beam direction (the z axis), p_{max} is the maximum momentum carried by the initial parton and $\sqrt{s}$ is the center of mass energy. Similarly, the Feynman x_F of the final state

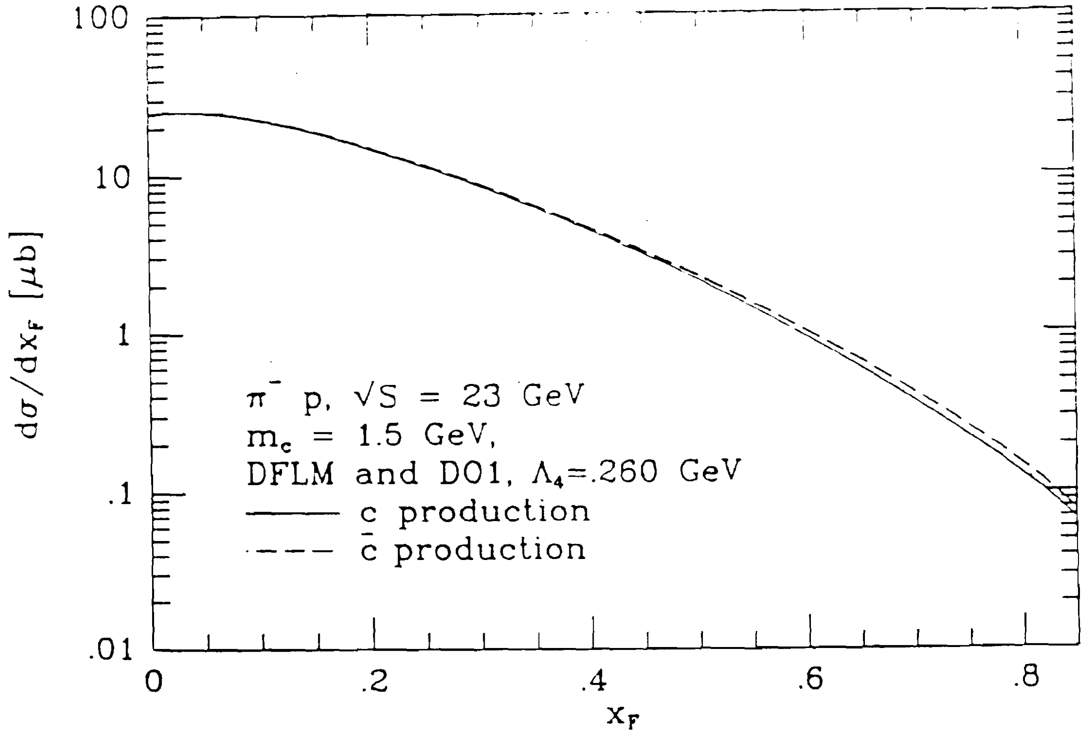

Figure 1.3: The theoretical x_F distribution calculated to O(α_S^3) for charm quarks in π^-p interactions[10].

charm hadron, used frequently in this thesis, is defined as:

$$x_F = \frac{p_z}{p_{max}} \simeq \frac{2p_z}{\sqrt{s}} \tag{1.3}$$

where p_z is the z component of the charm hadron momentum.

The cross section $\hat{\sigma}_{ij}$ can be calculated as a power series expansion in terms of the strong running coupling constant $\alpha_S(Q^2)$ whose dependence on Q^2 is expressed as:

$$\alpha_S(Q^2) = \frac{12\pi}{(33 - 2n_f)ln(Q^2/\Lambda^2)} \tag{1.4}$$

where n_f is the number of flavors. Λ is the QCD mass scale. For Q^2 much larger than Λ^2, the coupling constant $\alpha_S(Q^2)$ is small, so we can describe the interactions of the "asymptotically free" quarks and gluons perturbatively in terms of the QCD processes with different orders of α_S, and we can ignore the higher order processes in calculating the interaction cross sections. For Q^2 of order Λ^2, the coupling constant $\alpha_S(Q^2)$ is large; our perturbative description of the interactions of quarks and gluons are no longer valid. Thus, the mass scale Λ can be considered as the energy marking the boundary between the perturbative regime of the interactions of quarks and gluons and the non-perturbative regime. It is a free parameter to be determined from

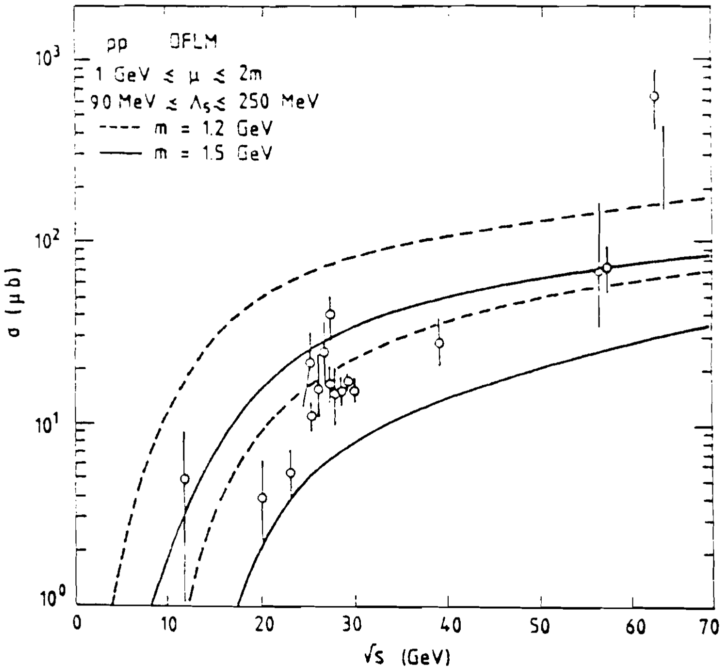

Figure 1.4: Cross sections for $pp \rightarrow c\bar{c}$ as a function of center of mass energy for two choices of charm quark mass m_c[16].

experiment. It is about 200 Mev (a typical light hadron mass). For charm production, $Q^2 \simeq m_c^2 \simeq 2.25 GeV^2$ ($m_c \simeq 1.5 GeV$), α_S is about 0.3. The perturbative calculation of the cross section may still be valid, but the uncertainty of neglecting corrections of order higher than α_S^3 may be large. Figure 1.3 illustrates the $d\sigma/d\hat{x}_F$ calculated up to the order α_S^3.

The large higher order corrections to charm quark production are mostly due to the fragmentation process,

$$\begin{array}{l} g+g\rightarrow g+g. \\ \qquad\qquad \llcorner\!\!\longrightarrow c+\bar{c} \end{array} \tag{1.5}$$

Because the cross section of $gg \rightarrow gg$ is about a hundred times larger than that of $gg \rightarrow q\bar{q}$ and a gluon fragments into a $c\bar{c}$ pair with a probability $\alpha(m_c^2)/2\pi$, the contribution of the process 1.5 can be numerically as large as the lowest order processes, even though it is of order α_S^3. It is possible but not guaranteed that the next order corrections(α_S^4) will be small.

The theoretical predictions of the total cross section are subject to several sources of uncertainty including the choice of the charm quark mass, forms of parton structure functions, and the specification of the momentum transfer squared Q^2. The

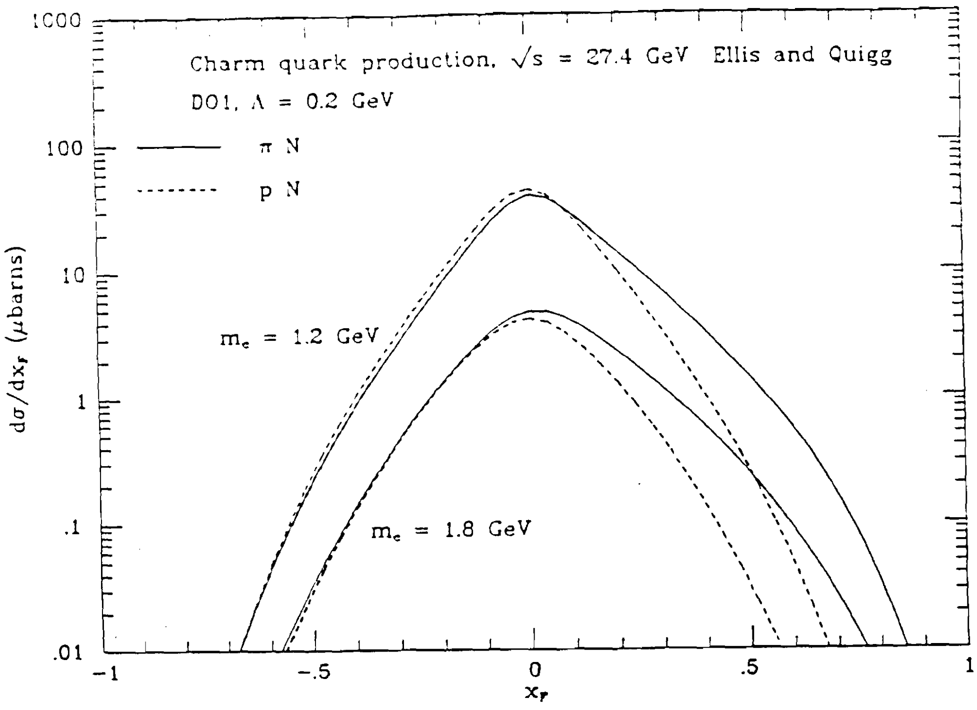

Figure 1.5: Differential cross section $d\sigma/dx_F$ calculated to $O(\alpha_S^2)$ for the production of charm quarks in πN (solid lines) and pN (dashed lines) collisions for two choices of the charm quark mass[8].

theoretical cross section is very sensitive to the charm quark mass; figure 1.4 shows that a decrease of the charm quark mass from 1.5 to 1.2 GeV results in an increase in the cross section by about a factor of 3. For a given charm quark mass m_c, the cross section calculated using the Duke-Owens set 1 (DO1) [13] parton structure functions is two times larger than that using the Martin-Roberts-Stirling set 1 (MRS 1)[14][15]. As discussed earlier, the uncertainty in $\alpha_S(Q^2)$ also contributes to the uncertainty of the total cross section.

These theoretical uncertainties don not affect the shape of the differential cross section $d\sigma/dx_F$ as much as the total cross section. To illustrate this, I show the theoretical calculation of $d\sigma/dx_F$ as given in figure 1.5 in based on the lowest order (α_S^2) processes by Ellis and Quigg[8]. Figure ?? demonstrates that a decrease in the charm quark mass m_c from 1.8 to 1.2 GeV can result in a factor of 10 increase in the magnitude of $d\sigma/d\hat{x}_F$ but little change in its $\hat{x}_F$ distribution shape.

Despite these uncertainties, the energy dependence of the predicted charm total cross section is consistent with the measurements as shown in figure 1.4[16].

The total cross section σ is only one aspect of charm production. The differential cross section with respect to x_F can reveal important physics as well. Equation 1.1 only gives the $\hat{x}_F$ dependence of the charm quark and not charmed hadrons. The produced charm quark can loose (gain) energy when interacting with the partons from the target (beam) as it fragments into a final state hadron. As a result, $d\sigma/dx_F$ can show a beam flavor dependence as well as an atomic number dependence. Also, $x_F > \hat{x}_F$ is possible.

The charm quark can combine with a sea quark or a valence quark from the two incident hadrons to form a final state hadron. We can compare the fragmentation process in hadroproduction and that in e^+e^- collisions. If we assume that the fragmentation processes are the same, we can use the fragmentation functions extracted from e^+e^- experiments[17] to derive the predicted $d\sigma/dx_F$ from equation 1.1. Then we can compare this modified prediction with our measured $d\sigma/dx_F$ distribution. The comparison is discussed in Chapter 6.

When the final state charmed hadron contains a valence quark of the incident beam hadron, this is called the leading particle effect. There has been evidence of this effect [18][19]. In this thesis, this effect is studied by comparing $d\sigma/dx_F$ of D^+ mesons and $d\sigma/dx_F$ of D^- mesons in π^--nucleon collisions, because the D^- mesons can contain the valence quarks (d quark) of beam π^- mesons whereas the D^+ mesons cannot. The detailed comparison is discussed in Chapter 6.

From the experimental point of view, the advantage of studying the differential cross section $d\sigma/dx_F$ is that it does not depend on the absolute detection efficiencies of the spectrometer, the absolute trigger efficiencies, and the reconstruction efficiencies. Furthermore, it does not depend on the beam flux, or nucleon densities in the target. Hence, the results can be free of the systematic effects due to the corrections to those quantities. The disadvantage of studying $d\sigma/dx_F$ compared to the total cross section is that theoretical prediction depends on the fragmentation processes. It is generally difficult to quantitatively understand fragmentation processes because the interactions are at low energies. To compare with the theory, we have to use a delta function to approximate the fragmentation function or use the fragmentation functions extracted from experiments.

Chapter 2

Spectrometer

In this chapter, I describe the E769 apparatus at the Tagged Photon Lab (TPL). Figure 2.1 shows the spectrometer in a three dimensional view. The location and geometry of each detector are shown in figure 2.2. The TPL spectrometer was used for Fermilab experiment E516 which was designed to study photoproduction of charm using a recoil electron trigger. Later on, experiment E691 used it to study charm properties and production mechanism in photon-nucleon collisions. It is a large forward acceptance spectrometer with silicon microstrip detectors (SMD)[20] for vertex detection, drift chambers for downstream tracking, two magnets for track momentum measurements, two Čerenkov detectors[21] for particle identification, and electromagnetic and hadronic calorimeters[22][23] to provide the transverse energy (E_T) trigger and particle energy measurements. The description of the TPL spectrometer can be found in the theses from E516[24] and E691[25][26][27].

The major change from E691 to E769 was the switching from a photon beam to a hadron beam. Accordingly, we added a beam tracking system to the spectrometer. The beam tracking system consisted of eight proportional wire chambers (PWC's) and two 25 μm pitched SMD planes. Other improvements included the addition of two downstream 25 μm SMD planes to enhance vertex detection. Also, we added two downstream y view PWC planes near the drift chambers (D1). The PWC planes can directly measure the tracks' y coordinates which the drift chamber system lacked. Furthermore, we developed a data acquisition system which was capable of taking 1.4

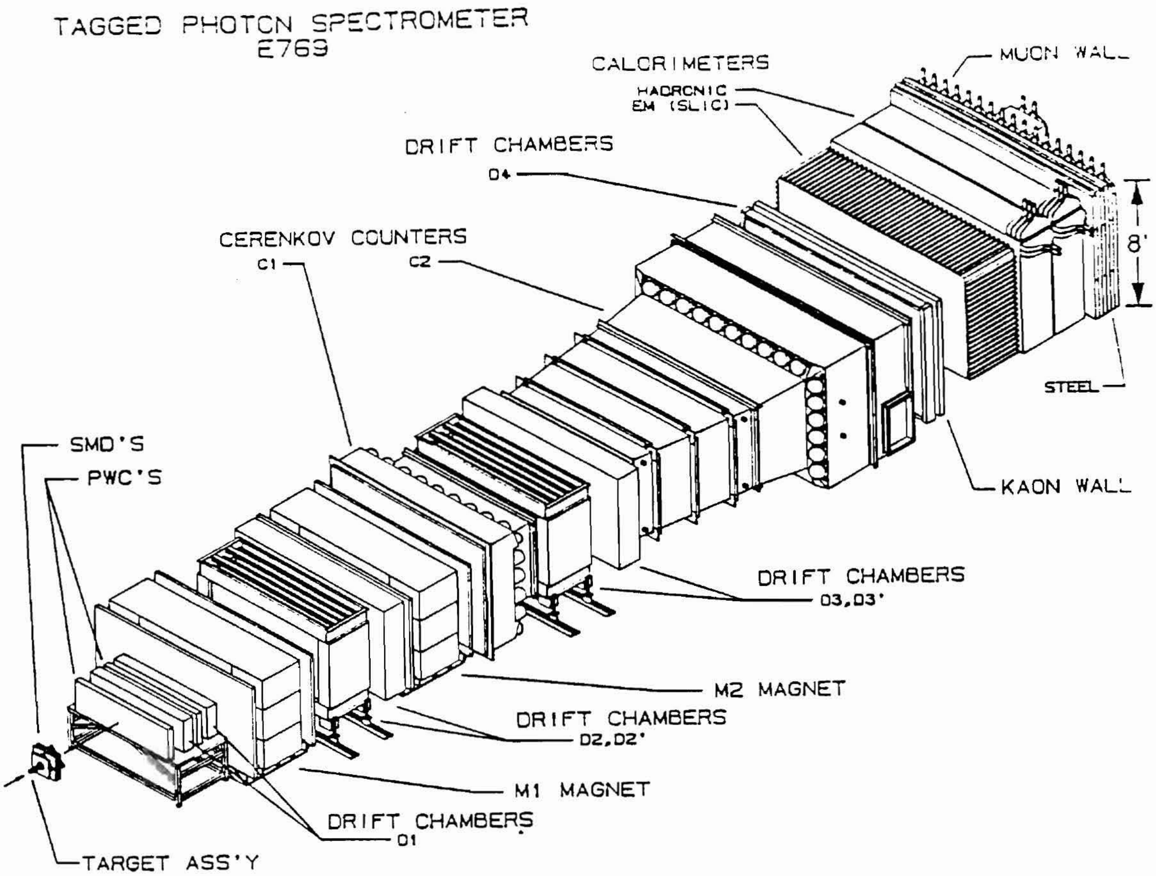

Figure 2.1: A three dimensional view of the spectrometer[21].

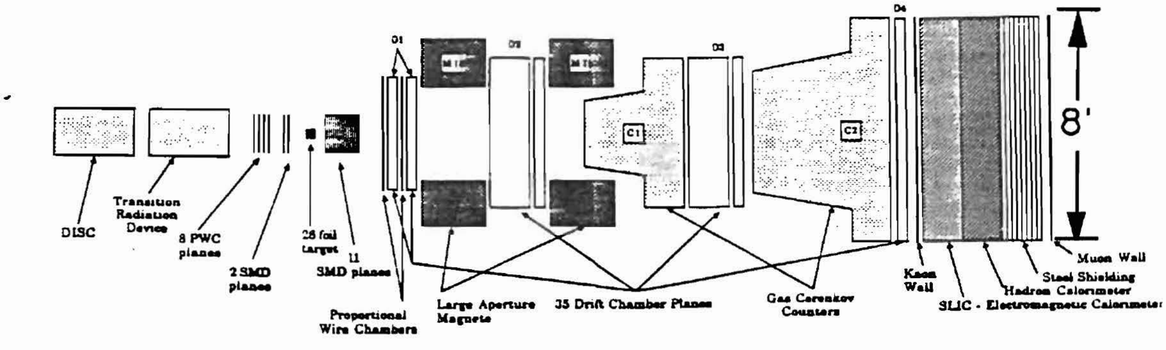

Figure 2.2: The cross section of the spectrometer[28].

MB/sec. The rate was 4 times higher than that in E691.

The coordinate system of TPL is defined with the convention that the z axis is along the beam direction, the y axis is pointing vertically upwards and the x axis is pointing horizontally towards the west.

2.1 Beam

To study the beam flavor dependence of charm hadroproduction, we used a beam consisting of three particle types: charged pions, kaons and protons. The primary source of the beam was the 800 GeV protons which were extracted from Fermilab's Tevatron and were split to 3 beamlines: Meson, Neutrino and Proton. The proton beam line was further divided into three beam lines: PWEST, PCENTER and PEAST. Finally, as shown in figure 2.3, the proton beam in PEAST was directed onto a 30 cm beryllium target where secondary particles including pions, kaons and protons were created. From the secondary hadrons, a 250 GeV charged hadron beam for E769 was selected by tuning the magnetic field of the selecting dipole. In figure 2.3, prisms, concave and convex lenses represent magnetic dipoles, focusing quadrupoles and defocusing quadrupoles respectively. The polarity of the dipole determines the charge of the beam (whether it is a positive or negative beam). We took half of our data with a negative beam and half with a positive beam. PEAST received about 20% of the total extracted 10^{13} protons per spill where a spill lasts 22 seconds and occurs every minute.

The 250 GeV charged hadron beam was then transported into the experimental area of E769. Beam particles were tagged with a Differential Isochronous Self-collimating Čerenkov (DISC) counter and a Transition Radiation Detector (TRD)[29], [30]. After that, the beam was steered onto the target as shown in figure 2.3.

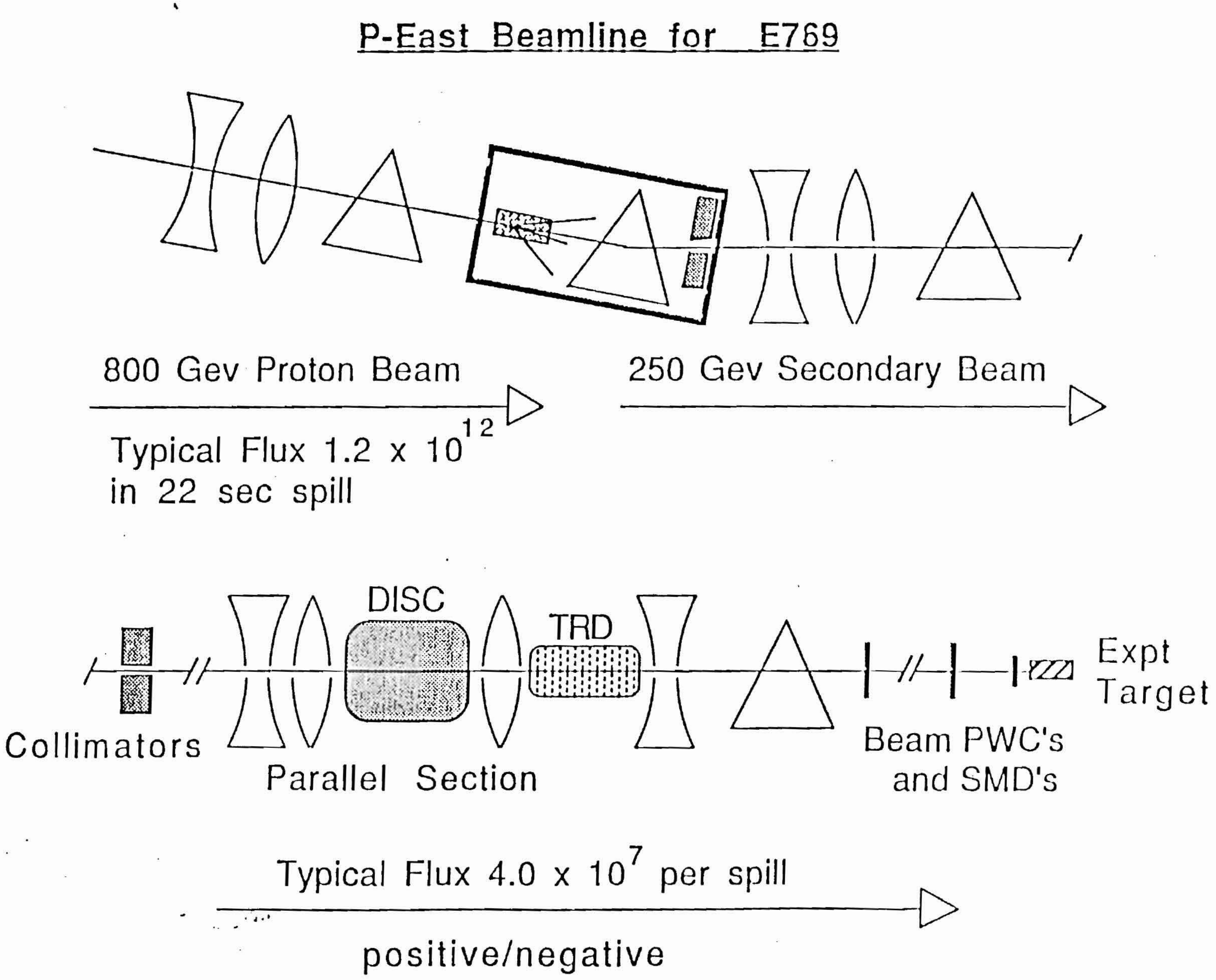

Figure 2.3: The beam for E769.

2.2 Tagging System

2.2.1 DISC

The DISC[28] was used to tag beam particles based on their different Čerenkov angles due to their slightly different speeds. Its principle of operation can be found in the literature[31][32]. It was designed and built at CERN. It had a cylindrical shape. It was 5 meters long and 0.5 meter in diameter. As shown in figure 2.5, it was made of a chamber filled with helium at 8.3 atmospheres (135 psi) as the medium for Čerenkov radiation. A mirror located at the end of the chamber was designed to reflect the Čerenkov photons backwards through the slits on a diaphragm. The mirror had a hole in the middle to allow the beam particles pass through. The diaphragm was located at the focal point of the mirror, so the Čerenkov light from a beam particle type was imaged to form a ring on the diaphragm. The slits only let the light ring with a radius 10.75 cm go through as shown in figure 2.5. The photons were detected by eight phototubes which were behind the slits and arranged symmetrically around the beam axis.

A charged particle emits Čerenkov radiation with an angle θ_c satisfying $cos\theta_c = 1/n\beta$ when it travels in a medium with a speed greater than the phase speed of light. The greater the speed, the larger the Čerenkov angle θ_c. The three beam particles pions, kaons and protons (antiprotons for the negative beam) had different speeds or βs, because they had the same momentum but different masses. Thus, their Čerenkov radiation produced three rings on the diaphragm with the pion ring being the largest and the proton ring the smallest. The radii of the rings could be varied by changing the helium pressure in the chamber because the pressure changes the index of refraction n, hence, Čerenkov angles. As a result, the DISC could be set to tag a particular beam particle type by selecting a pressure so only its Čerenkov radiation could pass the slits and fire the phototubes. Because the beam has a finite angular spread, a beam particle to be tagged may not fire all of the phototubes. The particle was considered 'tagged' by the DISC if more than four phototubes were fired simultaneously.

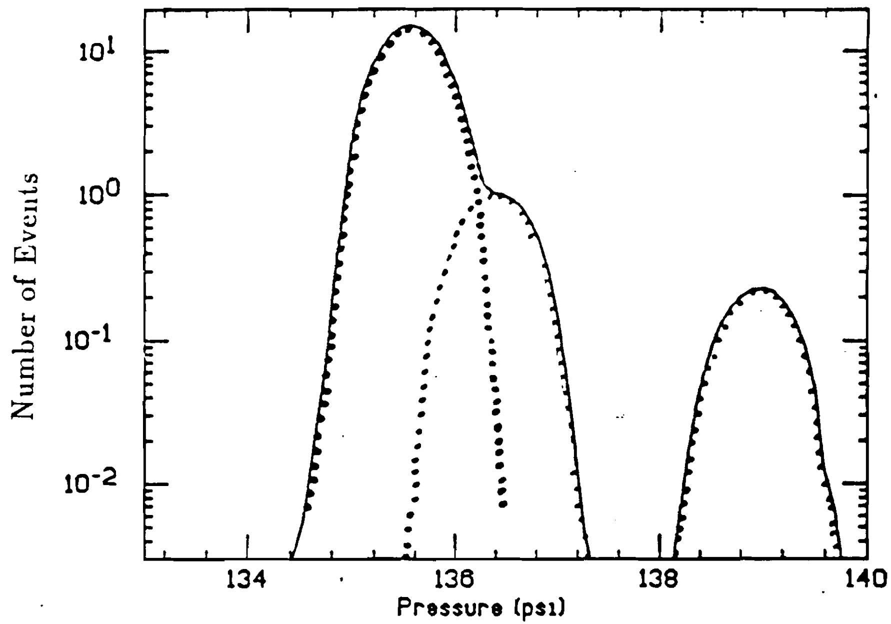

Figure 2.4: The pressure curve for the negative beam. The three peaks (from left to right) are due to beam particles π^-, K^- and $\bar{p}$ respectively. The area of each peak shows the relative concentration of each particle type.

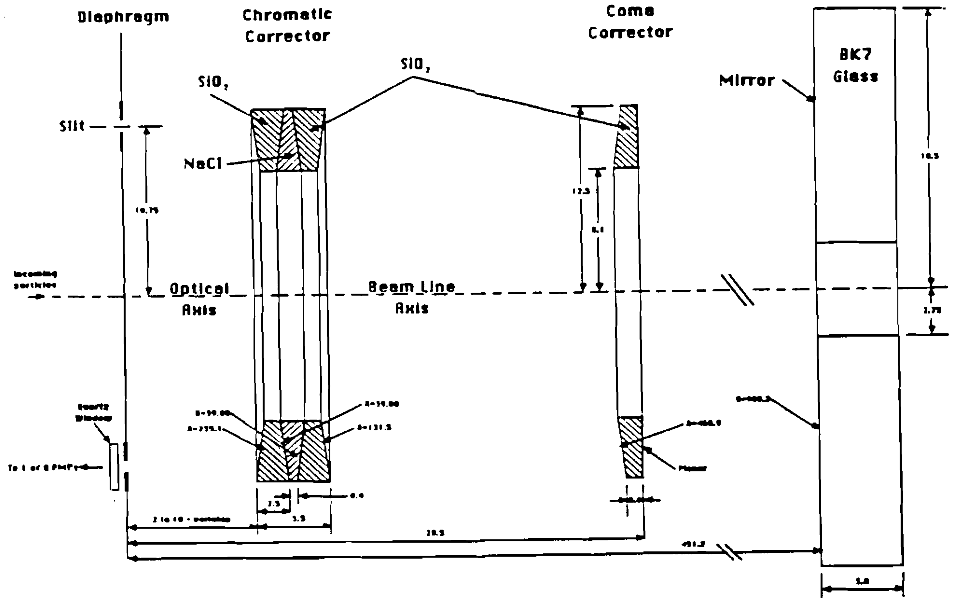

Figure 2.5: The Schematic of the DISC[28].

Figure 2.4 shows the relative concentration of negative pions and kaons, and antiprotons (predominantly π^-s) in the beam. The curve was obtained by varying the helium pressure in the chamber and so was called the pressure curve. The kaons only made up about 6% of the beam in both the negative and positive beams, so the pressure was set at the kaon peak in the DISC throughout most of the runs to enrich the kaon induced triggers. When the DISC was set on kaons, we took every kaon physics trigger and a fraction of the non-kaon triggers which were selected using prescalers. A prescaler selects every n^{th} trigger, where the prescaling factor n is adjustable.

Because of the overlap of the pion and kaon peaks as shown in the pressure curve, the pressure was chosen slightly above the kaon pressure peak keeping the pion contamination below 5%, while maintaining a kaon tagging efficiency of 40%.

2.2.2 Transition Radiation Detector

The TRD[29][30], located following the DISC, was used to separate protons from pions for the positive beam when the DISC was set on kaons. The TRD information was not used in the analysis of the negative beam data. However, for the completeness of the spectrometer, I still include a description of the TRD.

Figure 2.6 depicts one of the 24 modules of the TRD with the orientation such that the incident hadron beam entered from the left side of the figure. The radiator of the module was built by stacking 200 12.7 μm thick polypropylene foils alternatively with 180 μm nylon nets to maintain gaps between the foils. The gaps were constantly flushed with helium. Two 64 wire PWC planes with 1 mm wire spacing were placed following each radiator stack to detect the transition radiation gamma rays. The combined photon capture efficiency of the two PWC planes was about 85%.

In each plane, we connected the 64 wires in groups of four and input them to amplifiers/discriminators. Then, they were input to LeCroy 4564 modules, 16 input OR gates, to make a single output which is the plane hit. The resulting plane hit signals were readout by CAMAC[1] latch module LeCroy 4448 modules as one of the raw data types.

---

[1] CAMAC stands for Computer Aided Measurement And Control.

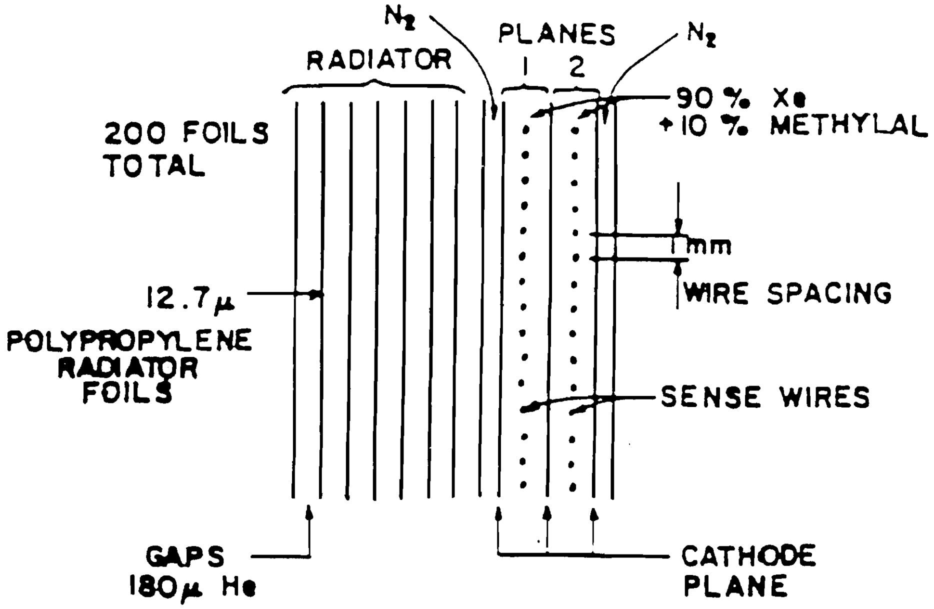

Figure 2.6: Schematic of one of the 24 radiator-chamber modules of the TRD[29].

Because the number of transition radiation photons is a monotonically increasing function of γ ($=1/\sqrt{1-\beta^2}$), pions radiate more photons than kaons and protons since pions have lower mass, and hence higher γ. Thus, on average, pions fired more TRD planes than kaons and protons. We demanded more than eight TRD plane hits to distinguish π^+s from protons. Figure 2.7 shows the beam identification power of using both the DISC and TRD.

We also used the TRD to estimate the contaminations by protons of kaon tagged triggers from the DISC.

2.3 Beam Tracking System

The beam tracking system was located between the transition radiation detector and the target. It consisted of two identical PWC stations and one SMD station. Each PWC station contained four planes in x, y, x' and w views respectively. The x' plane was displaced one half of a wire spacing from the x view plane to increase resolution. The w view plane axis was tilted -60^o from the x plane axis. Each plane had 64 wires with a wire spacing of 1 mm. The SMD station had two 25 μm planes (AX

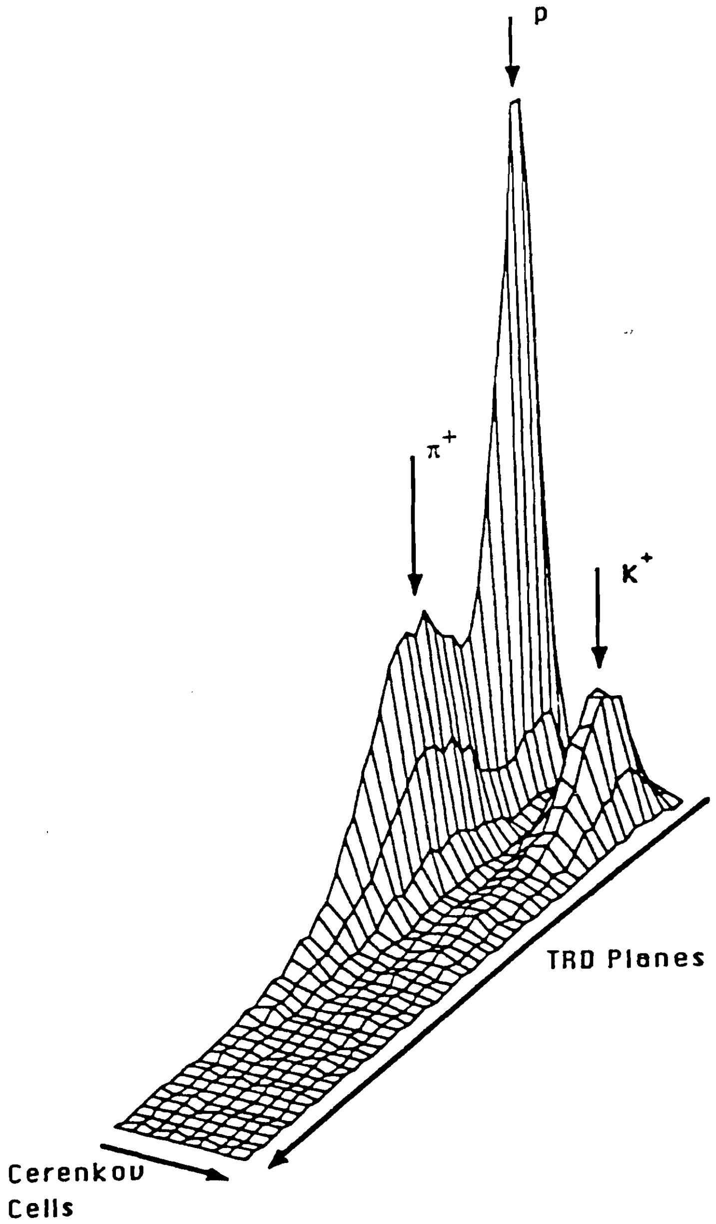

Figure 2.7: Distribution of events from a typical E769 positive beam data tape plotted along two axes, one of which is the number of TRD planes that fired and the other of which is the number of DISC photomultiplier tubes that fired[29].

and AY) in the x and y views respectively. Because the two SMD planes were about 7 cm upstream of the first foil of the target, the beam track positions at AX and AY could be used to identify the production (primary) vertices.

The PWC planes were read out by Nanometric Amplifier/discriminator and LeCroy model 2731A CAMAC modules. The PWC's were filled with a gas mixture of 17% CO_2, .3% Freon and the balance Argon.

The structure and readout system of the SMD planes AX and AY are given in section 2.5.

2.4 Target

In order to study the atomic number dependence of charm production, we chose a target made of four materials: Be, Al, Cu and W. They have an atomic number span from 4 to 74.

To associate charm primary vertices with a particular material, the target materials were split into 26 thin foils evenly placed along the z axis. The thicknesses were 250 μm for Be, Al and Cu and 100 μm for W. The gap between two adjacent foils was 1.36 mm. The layout of the target foils is shown in figure 2.9, a plot of the distributions of the reconstructed primary vertices along the z axis, using events which have interactions in the target. Note that we can clearly associate a primary vertex with a foil. The peak at z = -0.5 was due to the interaction counter which is described in chapter 3. The W foils were placed upstream of the other foils so that the tracks produced in the other foils are not multiple-scattered by W.

The amount of target material was chosen to give 2% of an interaction length based on the conflicting requirements of high rates and small multiple scattering.

The target foils were stacked in a plexi-glass box whose dimensions are shown in figure 2.8. The holes along the z axis were designed to allow the beam pass through. The gaps between the foils were accurately maintained by spacers. The spacers were 1.36 mm thick paper washers. Table 2.1 summarizes the properties of the target.

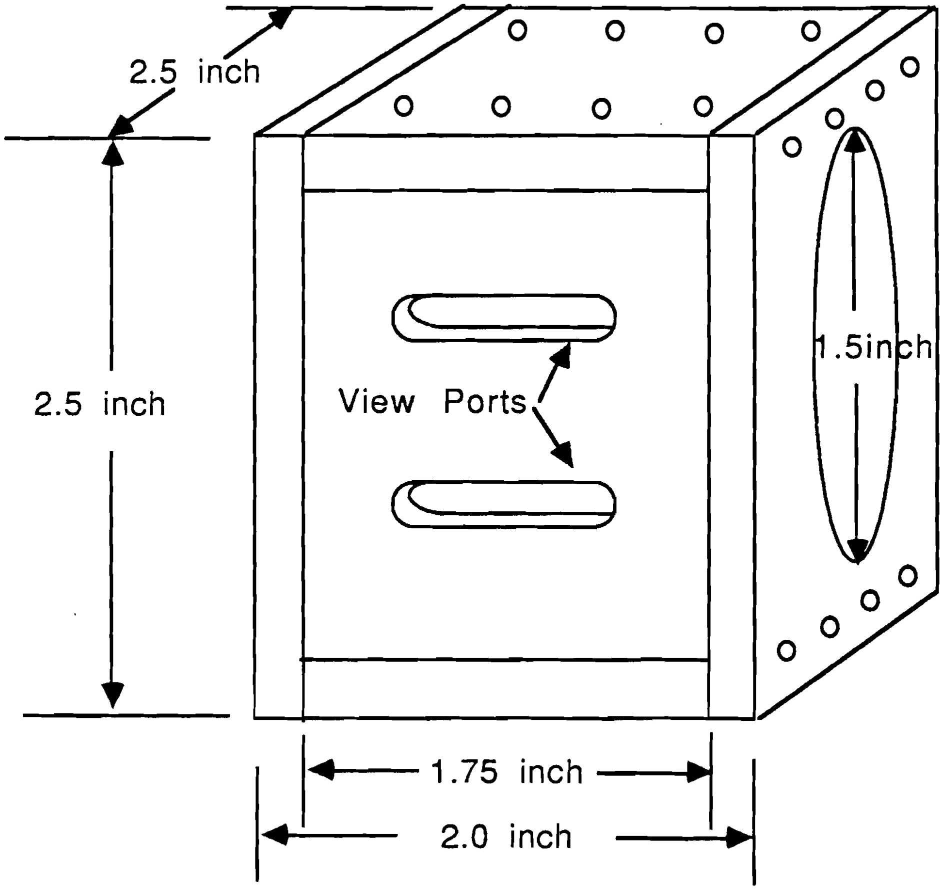

Figure 2.8: The Target Box.

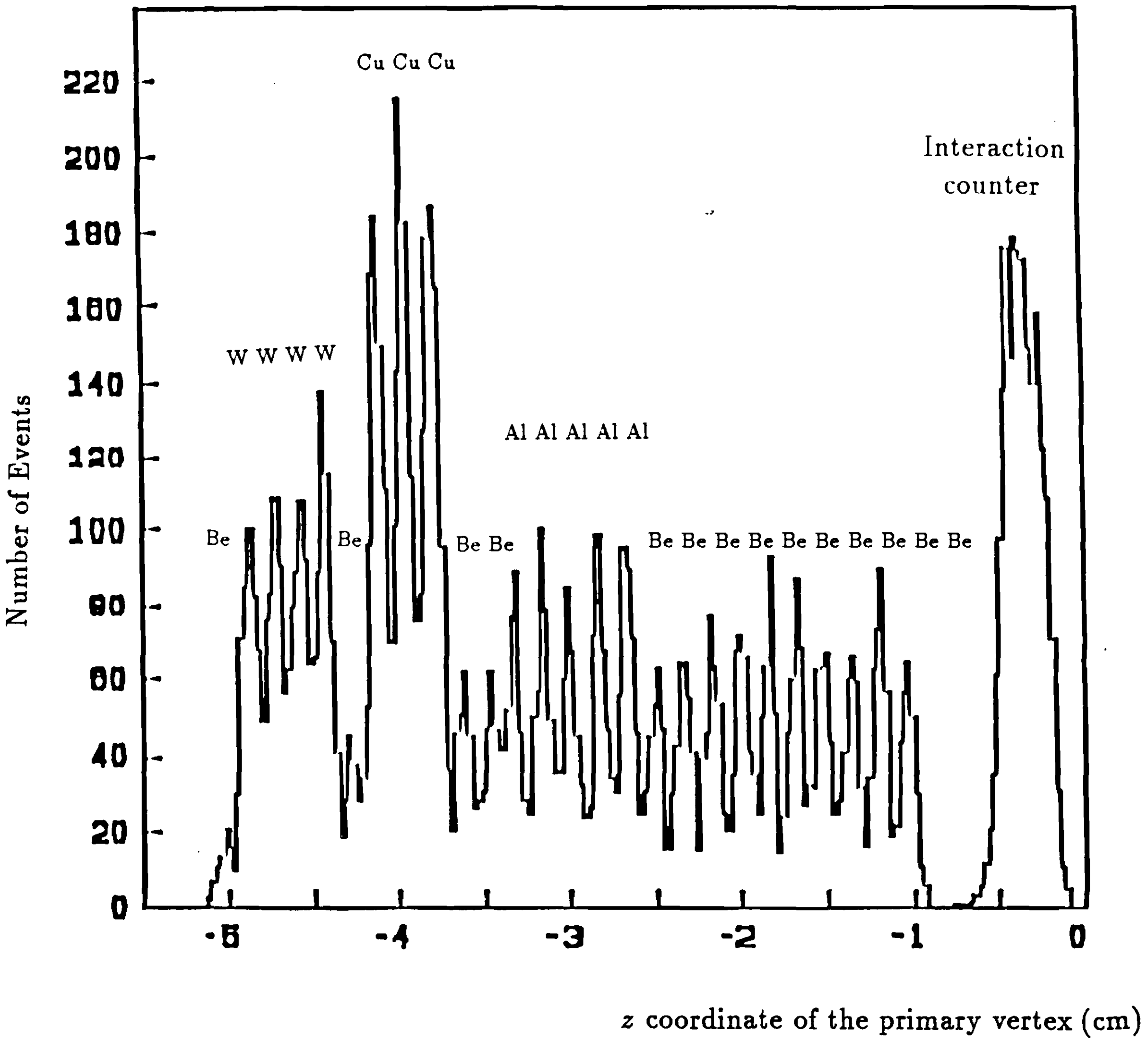

Figure 2.9: The distribution of the primary vertices along the beam axis. The distribution shows the target foil layout.

Material	Atomic Number	No. of foils	thickness/foil (μm)	λ_I (%)
Be	4	14	250.0	0.87
Al	13	5	250.0	0.32
Cu	29	3	250.0	0.50
W	74	4	100.0	0.43
Total	-	26	-	2.12

Table 2.1: Target Material Information for E769.

2.5 SMD System

In an experiment, the key to observing charm is to separate the production vertices from the charm decay vertices. The lifetime for $D^{\pm}$ is 1.07 picoseconds, other charmed particles have lifetimes of fractions of a picosecond. When they are produced relativistically, they typically travel a distance $\Delta Z = \gamma c\tau$ before they decay. As shown in figure 2.10, if the angle between two decay tracks is θ and the transverse spatial resolution of a vertex detector is σ, the charm vertex position resolution along the beam axis (z axis) will be $\sigma_{zs} = \sigma/sin\theta \simeq \sigma\gamma$. The effective separation SDZ of the charm decay vertex from the production vertex is defined as the distance of the charm particle traveled divided by the error on the distance. More explicitly, $SDZ = \Delta Z/\sqrt{\sigma_{zs}^2 + \sigma_{zp}^2}$ where σ_{zp} is the vertex position resolution of the production vertex along z axis. Because the production vertex had many more tracks than the charm decay vertex, σ_{zp} is small compared to σ_{zs}. Therefore, $SDZ \simeq \Delta Z/\sigma_{zs} = c\tau/\sigma$. The effective separation SDZ has to be significantly greater than 1 because the fractional cross section for charm is less than 10^{-3}. The quantity SDZ is independent of the beam energy. This means that an increase of beam energy does not enhance the vertex detection of the short lived particles. Typically, $SDZ \simeq 150(\mu m)/\sigma$ for charmed particles since $\tau \simeq 0.5$ picosecond. This requires the transverse position resolution σ of a vertex detector be much smaller than 150 μm. In addition, because charm events are rare in hadroproduction, the vertex detectors have to be triggerable and be able to take high rate. The SMD satisfies all these requirements: the E769 SMD planes had expected resolutions of 7 μm for 25 μm pitched planes and 15 μm for 50

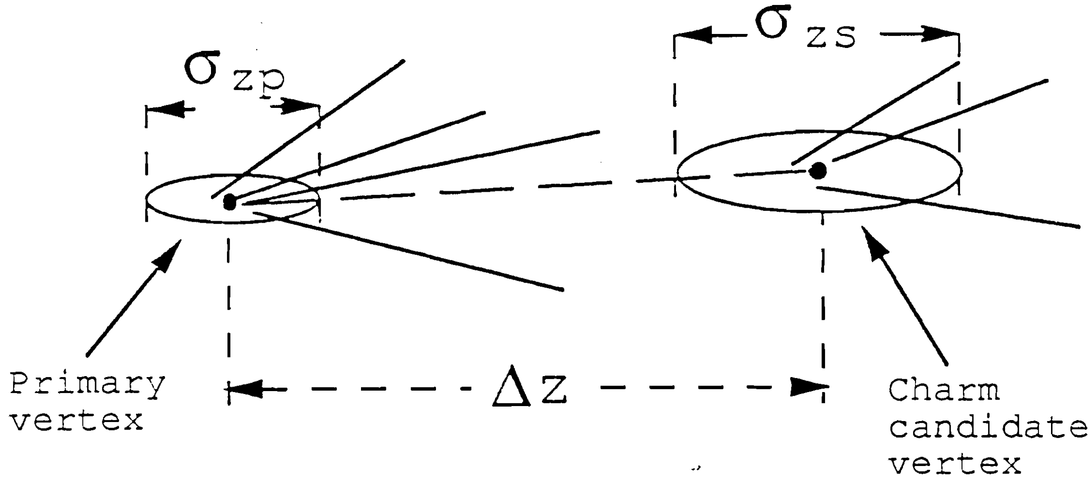

$$\underline{SDZ} = \frac{\Delta z}{\sqrt{\sigma_{zp}^2 + \sigma_{zs}^2}}$$

Figure 2.10: The definition of the quantity *SDZ*.

μm pitched planes. They enabled us to topologically separate charm decay vertices from primary vertices.

Figure 2.11 shows the layout of the 13 SMD planes. There are three views: x, y and v. The axes of the v view planes were tilted at 20.5° with respect to the x axis. In a position detector system, it is necessary to have v view planes in addition to the x and y view planes because they help to eliminate random combinations of the x measurements and the y measurements. The planes were grouped into five stations. The two planes described in section 2.3 in station A were located upstream of the target to measure the transverse beam track position (x,y) which can be used to identify primary vertices. The other planes were placed downstream of the target to measure the primary and charm decay vertices. The spacing between the SMD planes and the target was based on the conflicting requirements of long tracking lever arm and good angular acceptance. The distance of furthest plane from the last target foil was about 25 cm. The entire SMD system had an angular acceptance of about 100 milliradians. Four planes AX, AY, BX and BY, in stations A and B, had 386 strips with 25 μm pitch in the central region and 152 strips with 50 μm pitch on each side of the outer region. The other nine planes were contained in stations 1, 2

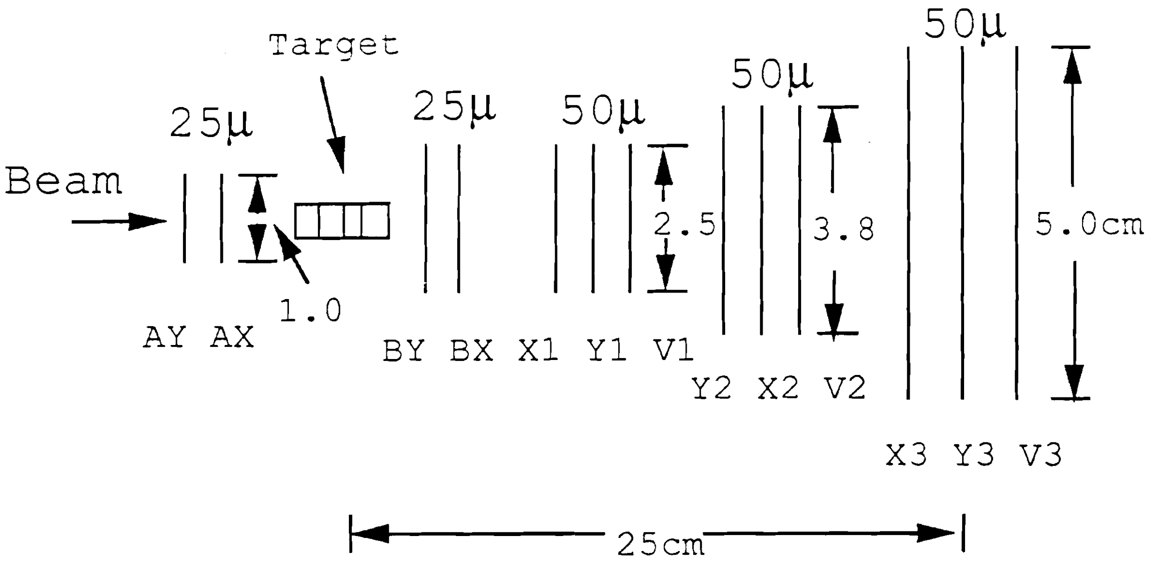

Figure 2.11: The SMD system.

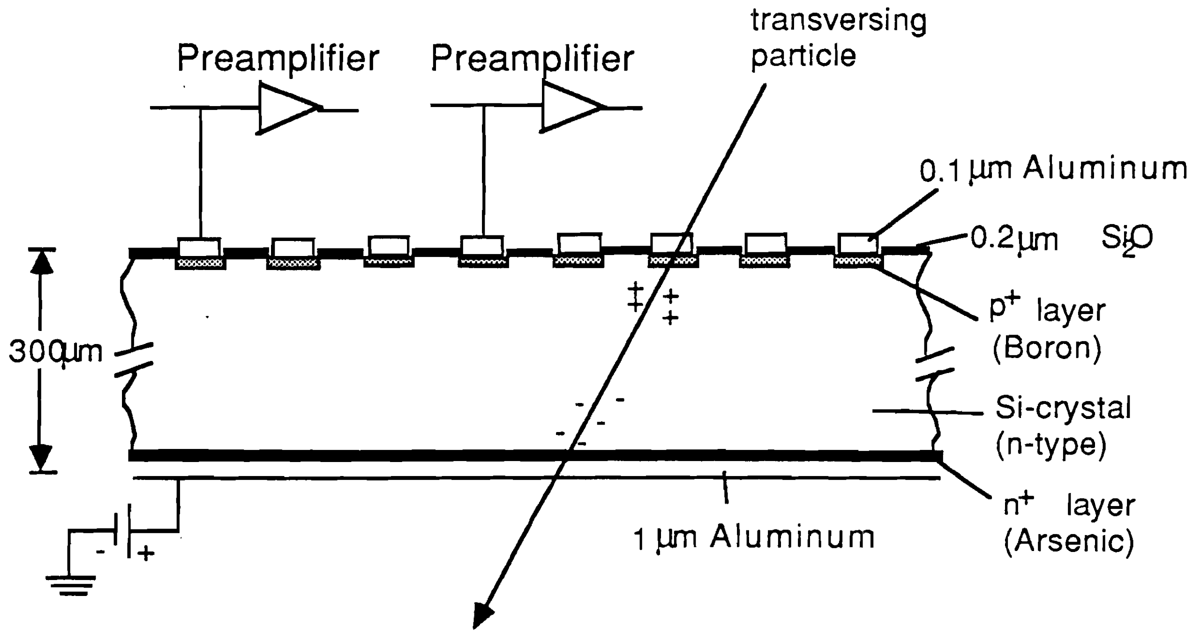

Figure 2.12: The SMD plane structure.

and 3 as shown in figure 2.11. They were originally used for experiment E691, so I call them the E691 planes. They had a pitch of 50 μm. We instrumented the 25 μm strips in the central regions of the beam planes AX and AY; while we instrumented both 25 and 50 μm pitched strips of BX and BY. The number of strips instrumented in each station progressively increases in the downstream direction as summarized in Table 2.2.

Stations	Active Area (mm^2)	Instrumented Strips	
		25 μm	50 μm
A	10 × 10	2 × 386	
B	16 × 16	2 × 386	2 × 304
1	26 × 26		3 × 512
2	50 × 50		3 × 768
3	50 × 50		3 × 1000

Table 2.2: SMD Characteristics.

The cross section of an SMD plane is sketched in figure 2.12. A silicon plane is fabricated on a 300 μm thick n-type silicon wafer. The p-type strips with a spacing of 25 or 50 μm were formed by implanting boron atoms on the upper surface of the wafer. Aluminum is deposited on top of the p-type strips to allow charge collection. The aluminum strips were connected to a printed circuit fan-out board using a ultrasonic bonding technique. This bonding technique can only be applied for the strip spacing greater than 100 μm. For the E691 planes with a 50 μm pitch, even and odd numbered strips had to be fanned-out on opposite sides of the detectors as sketched in figure 2.15. For the 25 μm planes, the aluminum strips were first fanned-out to reach a pitch of 50 μm on silicon wafers; then, the bonds were made for even numbered strips on one side and odd numbered strips on the other to fan-out printed circuit boards.

The bottom face of the silicon wafer is doped with a uniform n-type layer of arsenic over which aluminum is deposited so the bias voltage can be applied. Each strip is a p-i-n junction diode where i denotes the intrinsic material. When the silicon plane is in operation, a reverse bias voltage is applied to the p-i-n junctions to fully deplete the wafer to eliminate free charge carriers (electrons and holes). Thus, the only free electrons and holes are those created by the charged tracks passing through the wafer.

A minimum ionizing particle creates 24,000 electron-hole pairs on average as it passes through a 300 μm thick silicon wafer. For the E691 planes, the signal so created was first amplified by 4 channel Laben (model MSD2) hybrid preamplifiers to 1 mv. Then it was transmitted by 9 conductor aluminum shielded cables to a discriminator card (also called the readout card). The cables had alternating signal and ground wires to reduce crosstalk. As shown in figure 2.13, the discriminator card was an 8 channel Nanosystem S710/810 MWPC type which contains a dual differential comparator, an adjustable monostable multivibrator (also called a one-shot), and a shift register. The basic design of the card was modified at the front end to include a transistor to invert and amplify the input, and a potentiometer to adjust the discriminator threshold. The added components are shown on the left side of the dashed line in figure 2.13.

For the newly acquired 25 μm planes, the readout system had the same architecture but the preamplifiers and the readout cards had different designs. The preamplifiers were 4 channel MSP1 types manufactured by Laben. The preamplifier outputs were differential. This means that the each signal has two outputs with the same magnitude but opposite polarity. The advantage was that the signal could be extracted by taking the difference of the two outputs and at the same time the noise could be canceled. The signals were then transmitted by 10 conductor pair twisted cables to the readout cards. As shown in figure 2.14, again, the front end of an 8 channel Nanosystem S710/810 MWPC discriminator card was modified to include a dual input comparator and a potentiometer for each channel as shown on the left side of the dashed line in figure 2.14. The input comparator was used to extract signals from the differential inputs. The potentiometer was for adjusting the discriminator threshold.

To ensure a homogeneous response of the readout system to the detector signals, the gain of each preamp channel was individually selected to be within 5% of the standard. Also, the discriminator thresholds on the MWPC readout cards were adjusted, using the added potentiometers, to correspond to 40% (0.4 mv of the preamp output) of the average charge created by a minimum ionizing particle. This threshold

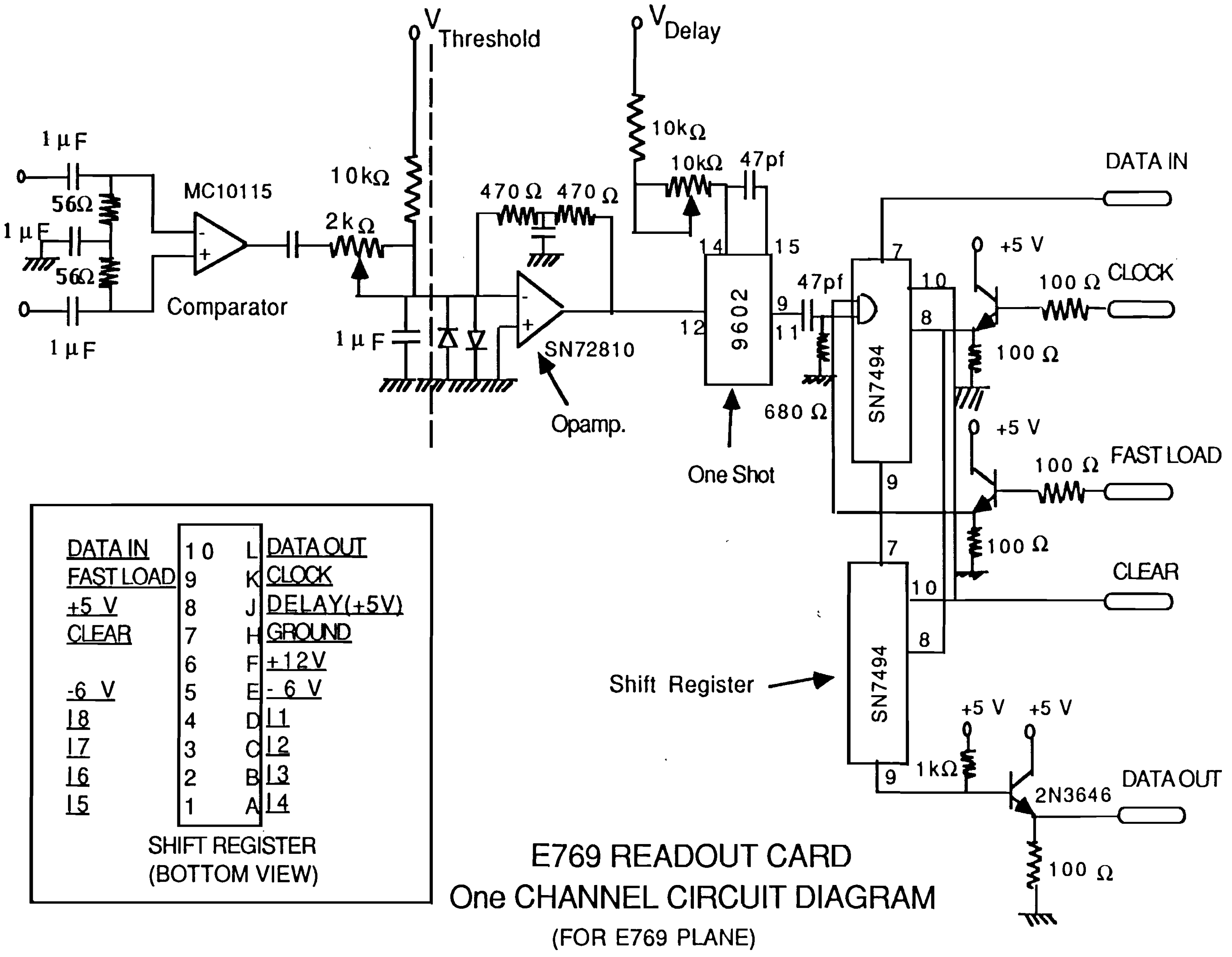

Figure 2.14: The sketch of the components of a single channel from the readout cards for the 25 μm SMD planes

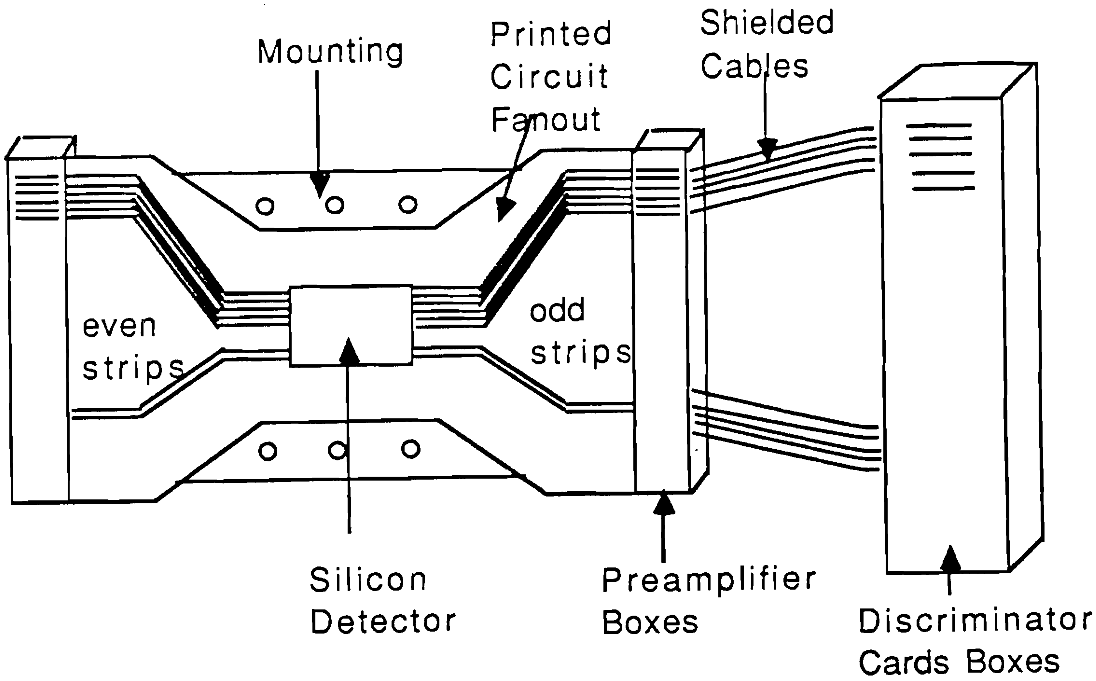

Figure 2.15: A small microstrip silicon plane, printed circuit fan-out and the sketch of the readout system.

resulted in high detection efficiency and low noise rate.

Because the even and odd numbered strips of an SMD plane were read out on opposite sides of the SMD as sketched in figure 2.15. The readout electronics were accordingly split into east and west halves to avoid unnecessary congestion. For the E691 planes, 10 shielded aluminum boxes were placed on the each side (east and west) of the detector to house the the readout cards as illustrated in figure 2.16 (A) and (B). Besides the readout cards, each box also contained a coupler card on the top of the readout card stack. The coupler card generated four fiducial bits with one bit on and three bits off all the time. The shift-registers of the readout cards and coupler cards in several boxes were connected serially to form a readout chain. The readout chain contained not only the hit bits but also the fiducial bits. The fiducial bits were used to to check the integrity of the readout chain. The readout chain was fed to a Nanoscanner Camac Module (WCS-300). As the figure 2.16 depicts, scanners 1 through 6 were used to read out the strips of the E691 planes. For instance, scanner 4 read out two boxes on the east side. They contained two groups of even and odd strips of X1, and two groups of odd strips of Y1. Scanners 7 and 8, not shown in the figure, were assigned to read out the planes in stations A and B respectively.

The X1, Y1 and V1 planes in the station 1 were manufactured by Enertec (France), a division of Schlumberger. The other planes were built by Micron Semiconductor (Britain). The Enertec detectors were fully depleted at a bias of 90 Volts. The Micron detectors required 70 Volts. The Enertec detector strips were fanned out to preamps via printed circuit kapton sheets, while the Micron wafers were mounted on copper plated G-10 fan-out board with a small strip of kapton at the edge for flexibility.

The silicon detectors and fan-outs were mounted inside rf boxes which are light and gas tight. This is necessary because light can induce electron-hole pairs resulting in an increase of leakage current. In addition, the boxes were constantly flushed with dry nitrogen to prevent vapor from being absorbed by the silicon wafers.

The maintenance and the performance of the SMD system is discussed in the next chapter.

2.6 Magnets

Figure 2.2 shows the locations of the two magnets M1 and M2. They were used to measure the track momenta. The magnetic fields were parallel to the y axis, so the bend was only in the x direction. As a result, the positive (negative) particles would be bent east (west). A charged particle with momentum p in a magnetic field is deflected by an angle:

$$\theta \simeq \frac{\int B \cdot dl}{3.33p} , \tag{2.1}$$

with B in Tesla, p in GeV/c and l in meters.

The detailed properties of the magnets are given in table 2.3. The magnet currents were 2500 and 1800 amperes for M1 and M2 respectively. The field maps at these currents were made using a Fermilab Ziptrack which consisted of three perpendicular coils which could move throughout the magnetic volumes. Several million field points were recorded and fitted to a sum of orthogonal polynomials consistent with Maxwell's equations[24]. This measurement was made in the earlier experiment E516.

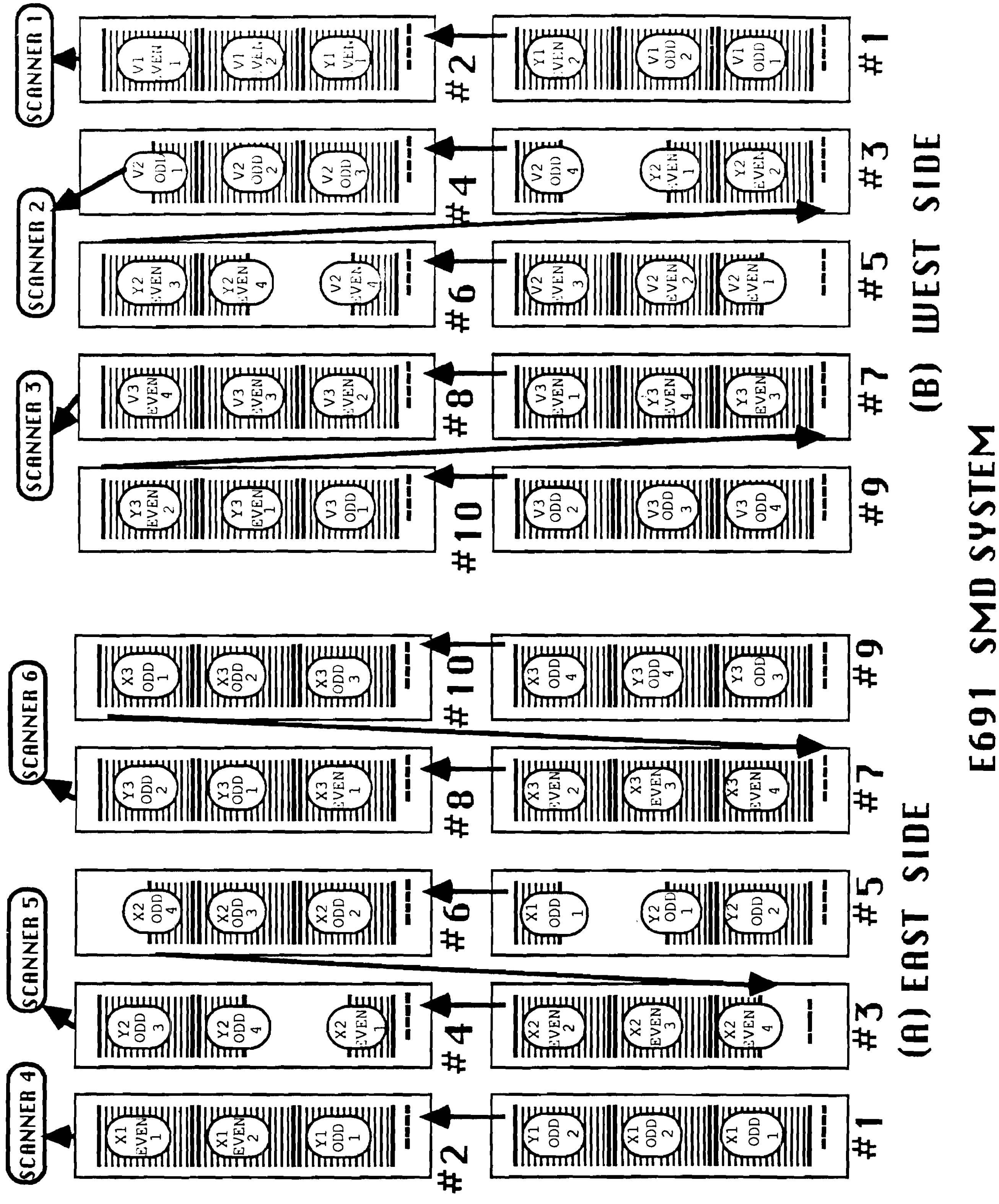

Figure 2.16: The SMD readout card boxes.

Magnet	M1	M2
Entrance Aperture (cm^2)	154 × 73	154 × 69
Exit Aperture (cm^2)	183 × 91	183 × 86
Length (cm)	165	208
E769 Current (Amp)	2500	1800
$\int B_y(0,0,z)dz$ (T-m)	-0.71	-1.07
p_T kick (GeV/c)	0.21	0.32

Table 2.3: Magnet Characteristics.

2.7 Drift Chambers

There were 35 drift chamber planes in the spectrometer to provide the downstream tracking. The tracks' trajectories were used for measuring their momenta, for identifying their particle types by the Čerenkov counters and for associating their showers in the calorimeters.

The drift chambers were grouped into four stations (D1, D2, D3 and D4). Their locations are shown in figure 2.2. The D1 planes were behind the SMD system to measure the track entrance angles to the first magnet M1. After the SMD planes were added in E691, they were also used to support the tracks which did not have enough hits in the SMD planes. The D2 planes were used to measure the track exit angles from M1 and entrance angles to the magnet M2. The D3 planes were used to measure the track exit angles from M2. Therefore, D1, D2 and D3 planes are important for track momentum measurement. The D4 planes, close to the calorimeters, were important for associating drift chamber tracks with showers in the calorimeters.

Each station was further divided into assemblies. The assemblies in D1 contained u, v, x and x' planes. The x' planes are identical to x planes but were offset by half a cell size to improve resolution. The u and v view axes were tilted $\pm 20.5^o$ from the x axis. The assemblies in the other stations consisted of sets of planes in x, u and v views. We call a combination of the measurements in an assembly (x,u,v) a triplet. A triplet was used to determine the x, y and z coordinates of a point on a charged particle trajectory. Table 2.4 shows the properties of the drift chamber system.

Stations	D1	D2	D3	D4
Dimensions ($x \times y$) (cm)	160 × 120	230× 200	330 × 200	550 × 300
Cell Size (x) (cm)	0.446	0.953	1.588	3.18
Cell Size (u/v) (cm)	0.476	0.892	1.487	2.97
Z position (cm)	154-195	382-501	928-1048	1738-1749
No. of Assemblies	2	4	4	1
view	$x\ x'\ u\ v$	$x\ u\ v$	$x\ u\ v$	$x\ u\ v$
No. of Planes	8	12	12	3
Resolution (mm)	0.35	0.3	0.3	0.8

Table 2.4: Drift Chamber Characteristics.

A drift chamber station was made of a stack of alternating sense planes and cathode planes. The sense planes consist of alternating sense and field wires transverse to the beam. The cathode planes and field wires were held typically at -2.1 kv and -1.6 kv respectively, so that the ionized electrons were forced to drift toward the sense wires which were held ground potential. We operated the drift chambers in the 'plateau region' of the gas, so the drift velocity v_d was nearly constant. The v_d was obtained by fitting muon tracks produced in the upstream beam dump. From the drift time Δt, the distance d from the particle's hit position to the sense wire can be defined by the relation: $d = v_d \Delta t$.

Each wire was read out by a Nanomaker N-277C amplifier discriminator card which also produced a start pulse for a TDC. The common stop signal for the TDCs came from the interaction counter. Therefore, the TDC counts were larger for small Δt than for large Δt.

The drift chamber gas consisted of equal parts of argon and ethane with a 1.5% admixture of alcohol. The alcohol prevents sparks and thus protects the wires.

2.8 Downstream PWC Planes

As shown in figure 2.2, the two identical downstream planes were interspersed with two D1 stations. They were both in y view which the drift chamber system lacked.

Each plane had 288 wires with 2 mm wire spacing.

The gas mixture and readout system for the two planes were the same as the upstream PWC planes which has been described in section 2.3.

2.9 Čerenkov Counters

The locations of the two Čerenkov counters (C1 and C2) are shown in figure 2.2. They were used primarily to identify kaons and protons from copiously produced pions in hadronic interactions based on their momentum thresholds and amount of radiation. The identification of kaons and protons is important because they are the daughter particles of many important charm decays such as $D^+ \rightarrow K^-\pi^+\pi^+$, $D^0 \rightarrow K^-\pi^+$, $D^0 \rightarrow K^-\pi^-\pi^+\pi^+$, $D_s^+ \rightarrow K^-K^+\pi^+$, $\Lambda_c^+ \rightarrow pK^-\pi^+$.

When the speed of a charged particle exceeds the phase speed ($v_{th} = c/n$) of light in a medium (when $\beta > 1/n$), it emits Čerenkov radiation with an angle θ_c satisfying $cos\theta_c = 1/n\beta$. Therefore, using the relation $v_{th} = c/n$, the threshold momentum is,

$$p_{th} = \gamma_{th} m v_{th} = \frac{mc}{\sqrt{n^2 - 1}} \tag{2.2}$$

where m is the mass of the particle and $\gamma_{th} = 1/\sqrt{1 - v_{th}^2/c^2}$. The number of photons N emitted per unit wavelength (λ) and unit distance l is

$$\frac{d^2N}{d\lambda dl} = \frac{2\pi\alpha}{\lambda^2} sin^2\theta_c \tag{2.3}$$

where α is the fine structure constant.

Because the bulk of the tracks have momentum between 5 and 40 GeV, the index of refraction n in C1 and C2 was chosen to optimize the proton/kaon/pion identification in this momentum range. The upstream counter C1 was filled with N_2 gas and the downstream counter C2 with a He(80%)/N_2(20%) mixture. They were both operated at atmospheric pressure. The lighter helium gas in C2 gives a lower index of refraction n, thus a smaller θ_c and a higher p_{th}. However, because the Čerenkov radiation is proportional to $sin^2\theta_c$, C2 was made twice as long as C1 in order to allow enough photons to be produced and detected. Table 2.5 shows the properties of C1 and C2.

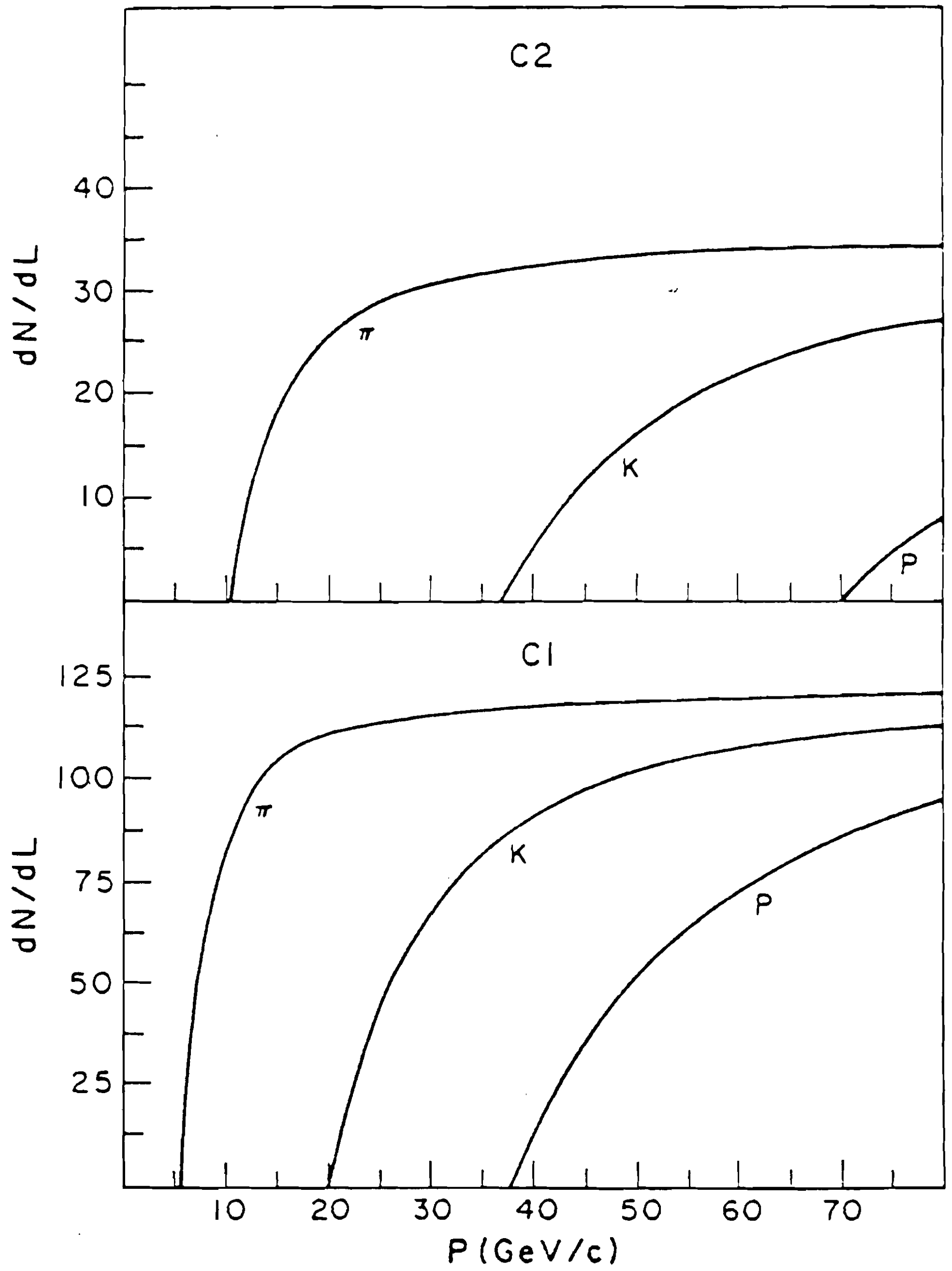

Figure 2.17: Čerenkov light intensities versus momentum[21].

Counter	C1	C2
Length (m)	3.7	6.6
No. of Mirrors	28	32
Gas	N_2	80% He + 20% N_2
Index of Refraction (n)	1.000309	1.0000901
π threshold (GeV)	5.8	10.5
K threshold (GeV)	20.0	37.0
p threshold (GeV)	37.7	69.8

Table 2.5: Čerenkov Detector Characteristics.

Figure 2.17 shows the theoretical number of Čerenkov photons emitted in C1 and C2 as a function of momentum for proton/kaon/pion. The intersect at the abscissa of these curves gives p_{th} for each particle. Notice that p_{th} is proportional to the particle mass.

Because the track multiplicity was similar to that in E516, we still used the same Čerenkov counters. The segmentation of the mirrors was a compromise between minimization of the cases where two or more particles in one event strike the same mirror and the full containment of the radiation by a single particle with a single mirror (and therefore a single phototube). The maximum Čerenkov ring radius [2] is 8.4 cm (8.7 cm) for C1 (C2). This led to the segmentation shown in figure 2.18 for C1 (C2) with the smallest mirror size $15 \times 25cm^2(15 \times 50cm^2)$. With this segmentation, the chance of radiation from two or more tracks falling on one mirror in C1 or C2 was less than 10% in E516[21].

Low mass nylon strings held the mirrors stable so that light collection efficiencies were not degraded during the run. Čerenkov light was imaged by a mirror to the face of an RCA 8854 photo-multiplier-tube located at the focal point of the mirror. A Winston cone (with parabola shape) was attached to the front of the phototube to accept photons with angle of incidence up to 20 degrees maximizing the number of Čerenkov photons hitting the phototube, while cutting out background light.

The first counter C1 was partially set inside M2 because of the limited available

---

[2] $r = L * tan\theta_c$, where L is the length of the Čerenkov counter and $\beta = 1$ is assumed.

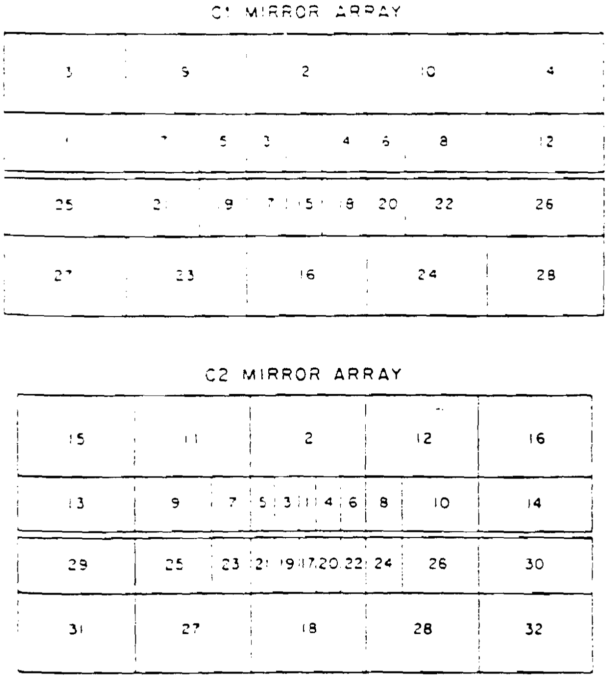

Figure 2.18: Mirror segmentation in C1 and C2[21].

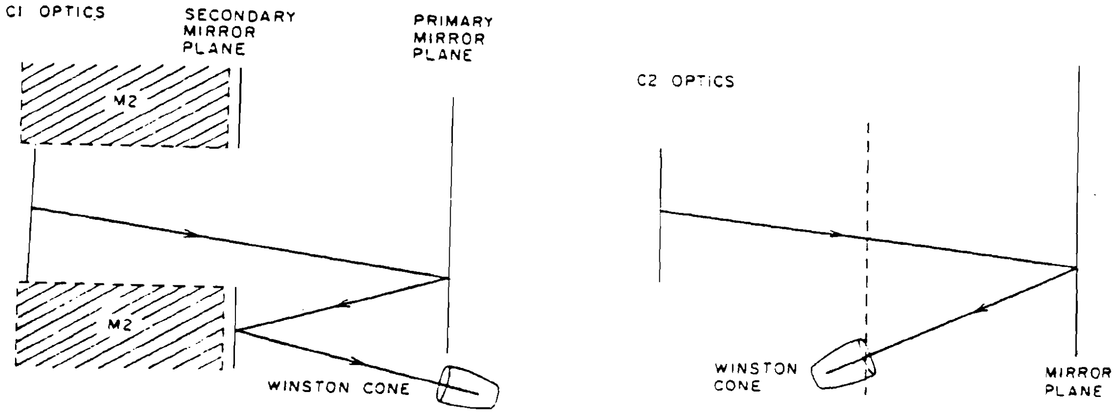

Figure 2.19: Light paths in C1 and C2[21].

space. A two bounce geometry (as shown in figure 2.19) for a C1 photon was required so that the phototubes could be placed as far away from the magnetic field as possible. This is because the magnetic field can degrade the performance of the phototubes by deflecting cascading photoelectrons through the dynodes. There was still residual magnetic field of up to 2 gauss which could reach phototubes after penetrating through the shielding pipes, so the problem had to be solved using fields generated by current carrying wires around the iron shielding pipes to cancel the residual field.

The phototubes were monitored during the run, using heavily attenuated laser light. The Čerenkov counters were calibrated using well separated high momentum tracks to obtain the pedestals and gains of phototubes.

2.10 Calorimeters

The transverse energy trigger of E769 was provided by the electromagnetic calorimeter SLIC (segmented liquid ionization counter) and hadronic calorimeter (called hadrometer). Photon and electron showers were measured by the SLIC. Neutral and charged hadron showers were measured by both the SLIC and hadrometer.

When a high energy electron enters a dense material it radiates high energy photons through Bremsstrahlung. The radiated photons interact with the heavy nuclei to produce electron and positron pairs. The electron and positron pairs in turn radiate photons and the photons produce more electron and positron pairs and so on until the the radiated photon energy falls below 1 Mev, the threshold energy for pair production. Then the shower stops. The photon showers are formed in the same way.

A hadronic shower is of a different character. When a high energy hadron enters a medium, it interacts with the nucleus to produce secondary hadrons. The secondary hadrons can produce next generation hadrons and so on. The charged secondary hadrons deposit their energy through ionization. The shower can be detected by collecting the ionization light. Because interaction lengths are typically longer than radiation lengths, the shower is more spread out compared to those of the electrons and photons. For instance, the hadronic showers usually extended from the SLIC to the hadrometer. On the other hand, the electron or photon showers were nearly

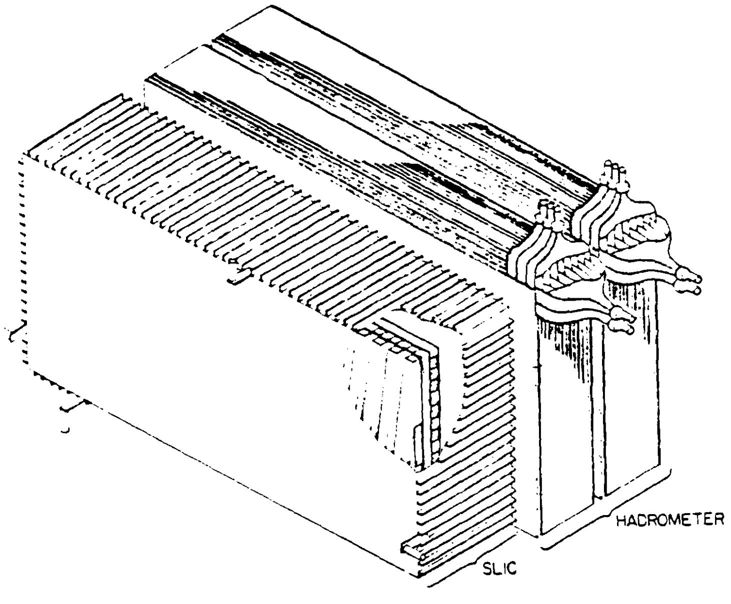

Figure 2.20: The SLIC and the hadrometer[22].

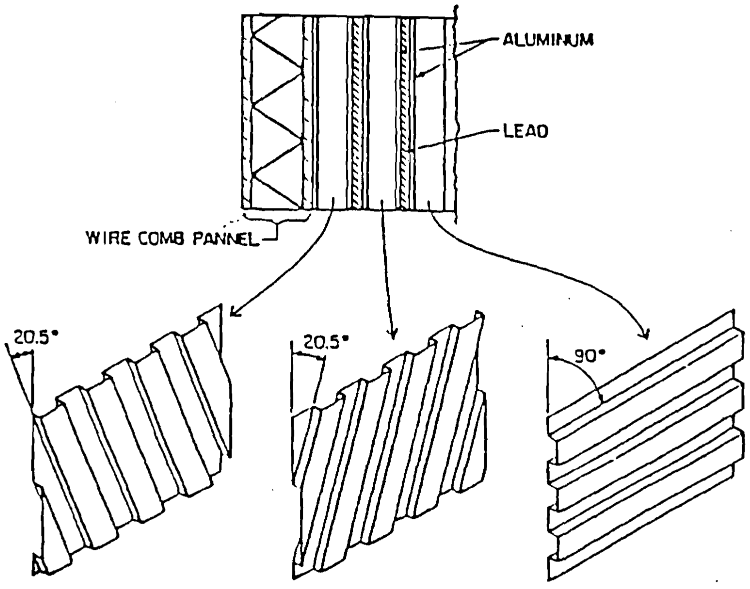

Figure 2.21: SLIC interior and the corrugated panels[22].

contained in the SLIC.

The SLIC had 60 layers, each composed of a sheet of 0.63 cm thick lead and a thin corrugated aluminum sheet filled with scintillating liquid as shown in figure 2.20. The lead was used as a radiator. The corrugation has a square wave shape with a half width of 3.17 cm which defines the width of the scintillator strips. The u, v and y view channels can be seen in figure 2.21. The aluminum corrugated sheets were coated with teflon film to provide total internal reflection when the angle of incidence was greater than 20^o. This occurs because the teflon film has a lower index of refraction than the scintillator liquid. The light emitted in the scintillator layers was guided through the corrugated channels and collected by wavelength-shifter bars glued on the edge of the SLIC. The wavelength-shifter bars converted ultraviolet into visible light to which the phototube is more sensitive. The wavelength-shifter bars summed light from all 20 layers in depth in a given view and transported the sum to phototubes. In the outer region of the SLIC, the light from two waveshifter bars were added and fed to one phototube; in the center region, one phototube read out one waveshifter bar to keep good spatial resolution. The y view counters were split into east and west halves of 58 strips each and they were read out from the side. The 109 u and 109 v view counters were read out at the top and bottom respectively.

The hadrometer had two identical upstream and downstream modules as shown in figure 2.20. Each module had 18 layers of 2.5 cm thick steel plate as the interacting material. Orthogonal strips of x and y counters were placed in alternate gaps in the 18 layers of steel. The steel and scintillator material together comprised 3 absorption lengths in each module. Each view was divided into 14.5 cm wide strips. The individual strips from 9 layers were integrated in the beam direction and read out by a 5 inch EMI 9791 KB phototube. The 33 x view strips were read out on the top, while the 38 y view strips were split into east and west halves, as in the SLIC, and were read out on the east and west sides of the modules.

The anode signals of the phototubes were digitized by the LRS 2280 ADC's. The phototube gains of the SLIC and hadrometer were calculated using high energy muons which were copiously produced at the upstream beam dump. A typical ADC gain was about 20 counts/GeV.

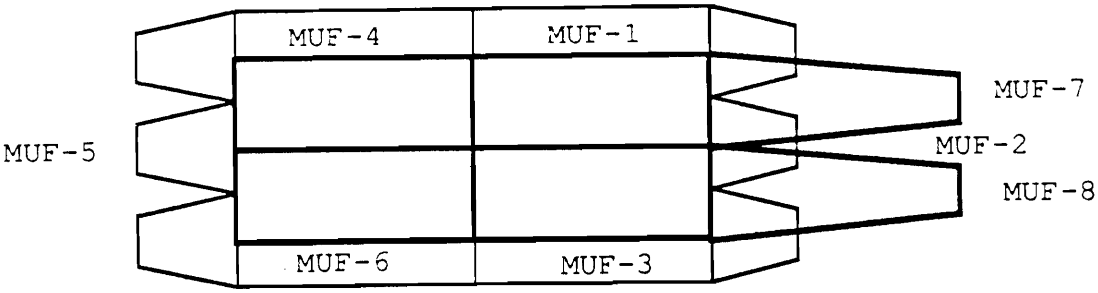

Figure 2.22: The Front Muon Wall[25].

2.11 Muon Walls

Two large plastic scintillator walls were used to detect muons. The Front Muon Wall, located at the beam entrance to the spectrometer, consisted of 8 plastic scintillation counters with lucite light guides. They were all 1.5 feet wide; 6 of them were 4 feet long and 2 of them were 8 feet long as shown in figure 2.22. The Back Muon Wall was made of 1.25 or 2 foot wide slabs of scintillators as shown in figure 2.23. Five inch EMI 9791KB phototubes were glued onto the lucite light guides. The signals from both walls were discriminated and latched. A four foot thick iron wall separated the Back Muon Wall from the hadrometer to stop the remaining hadrons which escaped the hadrometer.

The two muon walls were used mainly for triggering on muons. They were used in coincidence to select the calibration muons produced upstream of the spectrometer for the drift chambers, the SLIC and the hadrometer. They were also used in anti-coincidence to reduce the background rates in the J/Ψ dimuon trigger.

TDCs were installed on the Back Muon Wall to record the times it took for the signals to travel from the hit positions to the phototubes, so the y-coordinates of the muon hits could be measured.

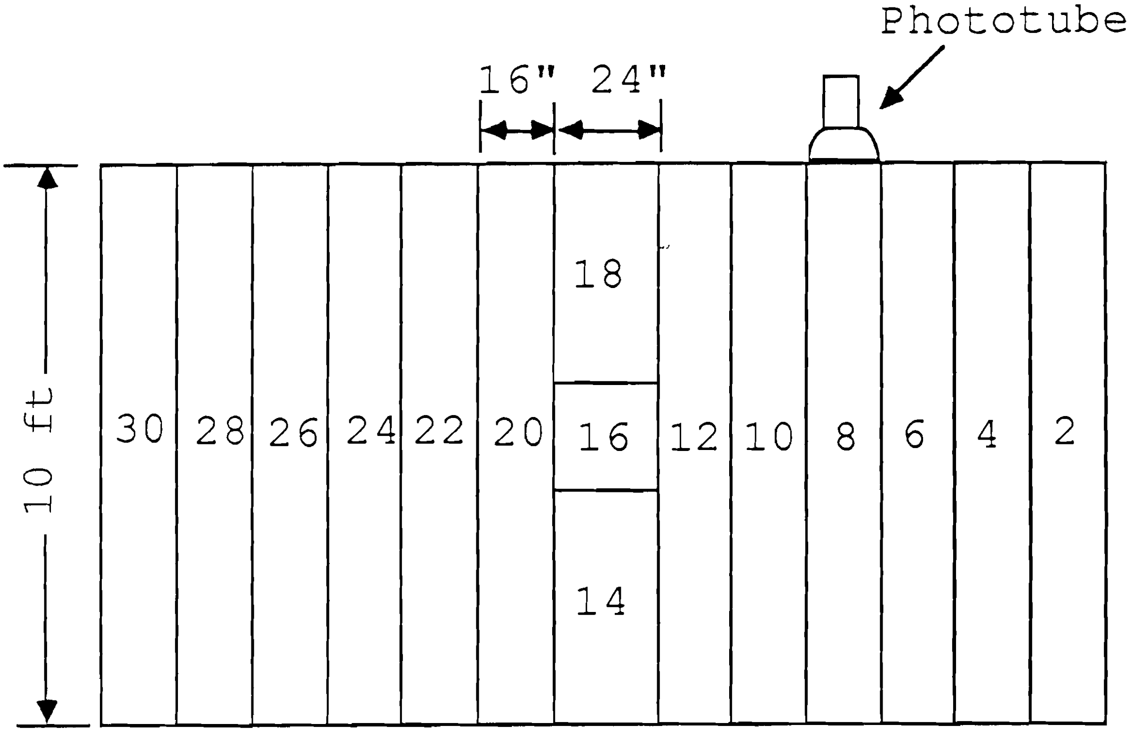

Figure 2.23: The Back Muon Wall[25].

Chapter 3

Data Collection

To do an experiment, we not only need a spectrometer, a beam to induce interactions, but also efficient triggers to select interesting (charm enriched) events and a data aquisition system to collect them.

3.1 Triggers

About 5% of our total data was taken with the interaction trigger. As shown in figure 3.1, three scintillation counters: the beam spot paddle, the beam halo paddle and the interaction paddle were involved in making this trigger. These paddles were made of plastic scintillators. Their dimensions were shown in figure 3.2. The interaction paddle had a comparable material as the Cu foils in terms of interaction length. As a result, about 20% of the charm was produced in the interaction counter. The discriminators for the beam spot and beam halo counters were set to allow a single minimum ionization particle to pass the discriminator level. The threshold of the interaction counter pulse was set at 5 minimum ionizing particles. It turned out that the interaction counter was only 50% efficient for hadronic inelastic interactions and nearly 100% efficient for charm. This is because the charm events have higher track multiplicities on average than the non-charm ones. The anti-coincidence of the beam spot and the beam halo counters selected only the beam particles (called "GOOD BEAM") which went through the circular hole on the halo paddle. The interaction

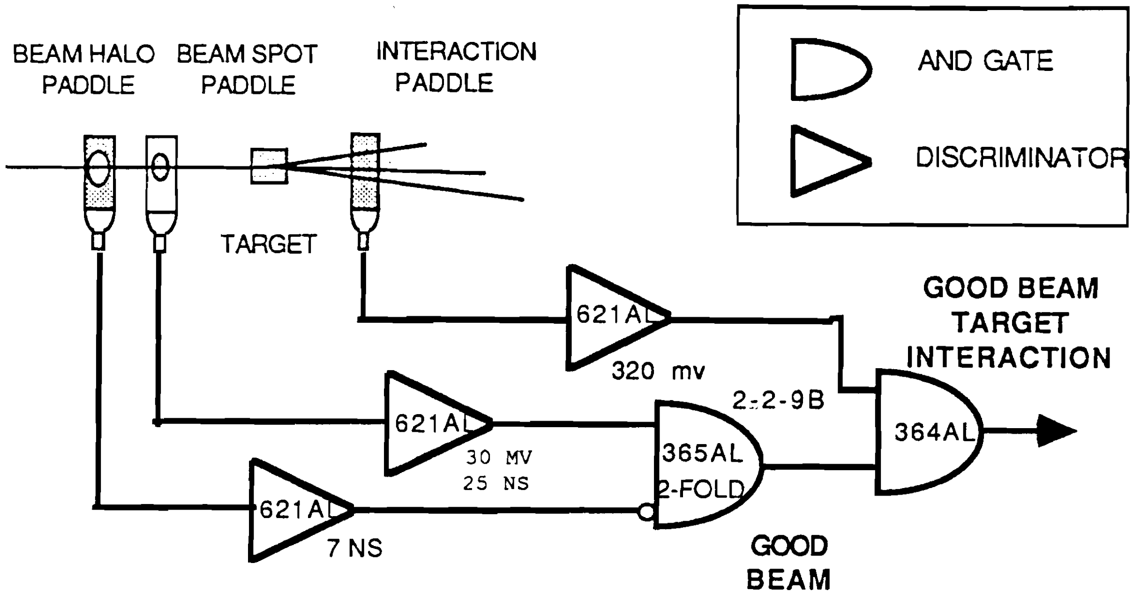

Figure 3.1: The interaction trigger diagram.

trigger (called "GOOD BEAM TARGET INTERACTION") was the coincidence of "GOOD BEAM" with the interaction counter.

Most of the data (90%) was taken with a large transverse energy trigger (E_T) set at 5.5 GeV. The motivation of having an E_T trigger was as follows. It has been observed that the mean transverse momentum of a particle produced in inelastic hadronic interactions is on the order of its mass. Because the charm hadrons are much heavier than the hadrons which are made of only the light quarks, such as up, down and strange quarks, a requirement of large E_T enriches the data sample with charm.

The E_T trigger was implemented by summing over the energy deposits in the SLIC and hadrometer counters with the weights chosen to be proportional to their distances to the center. The weights for the eight central counters of the two hadrometer modules were assigned to be zero. The dynodes of physically adjacent channels in each calorimeter view were summed in units of 8 and fanned into LRS 628 weighted fan-in/fan-outs as shown in figure 3.3.

The purpose of the E_T trigger was to yield a factor of three rejection over the interaction triggers. The E_T trigger was measured to be 78±8% efficient for charm

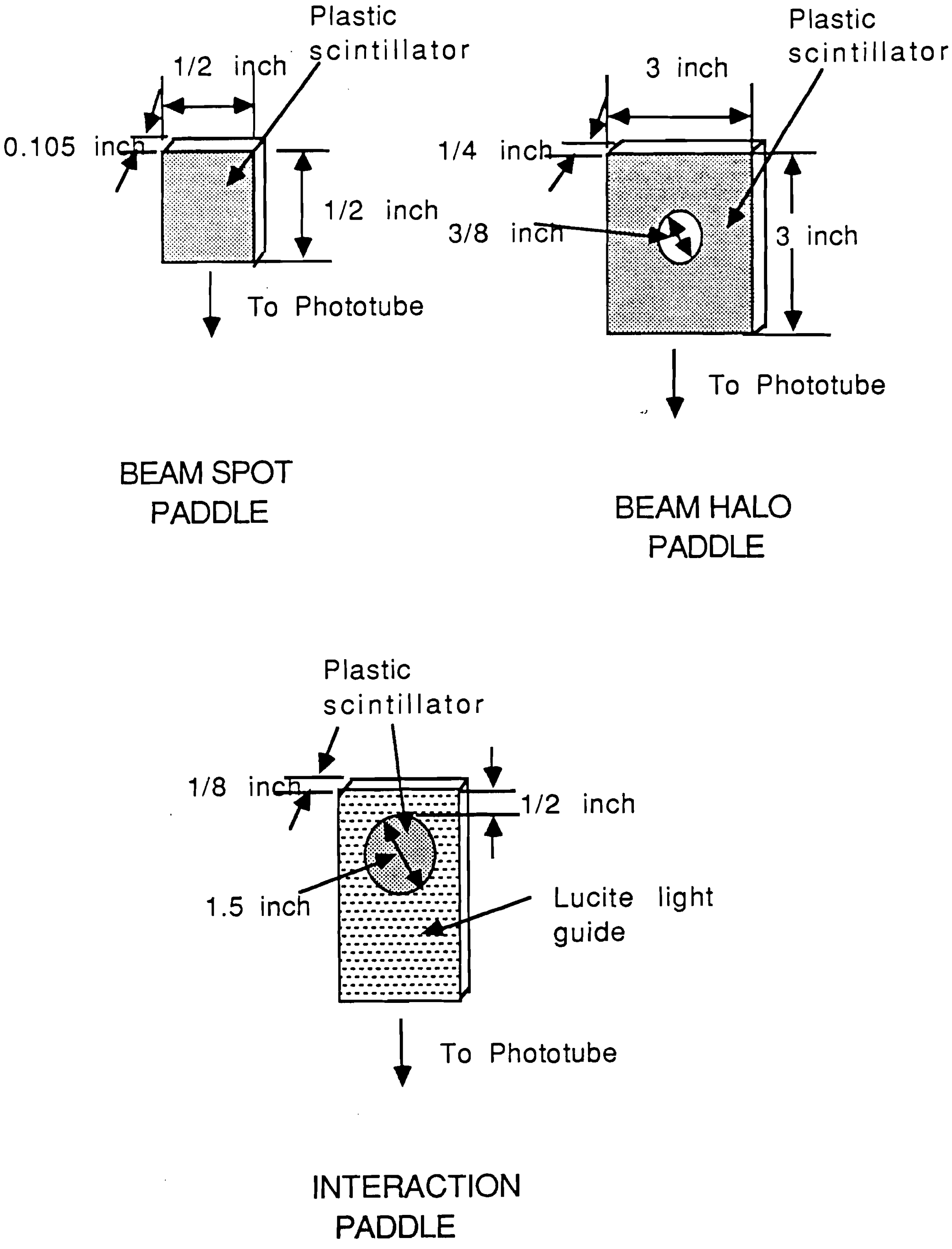

Figure 3.2: The beam spot, halo and interaction paddles.

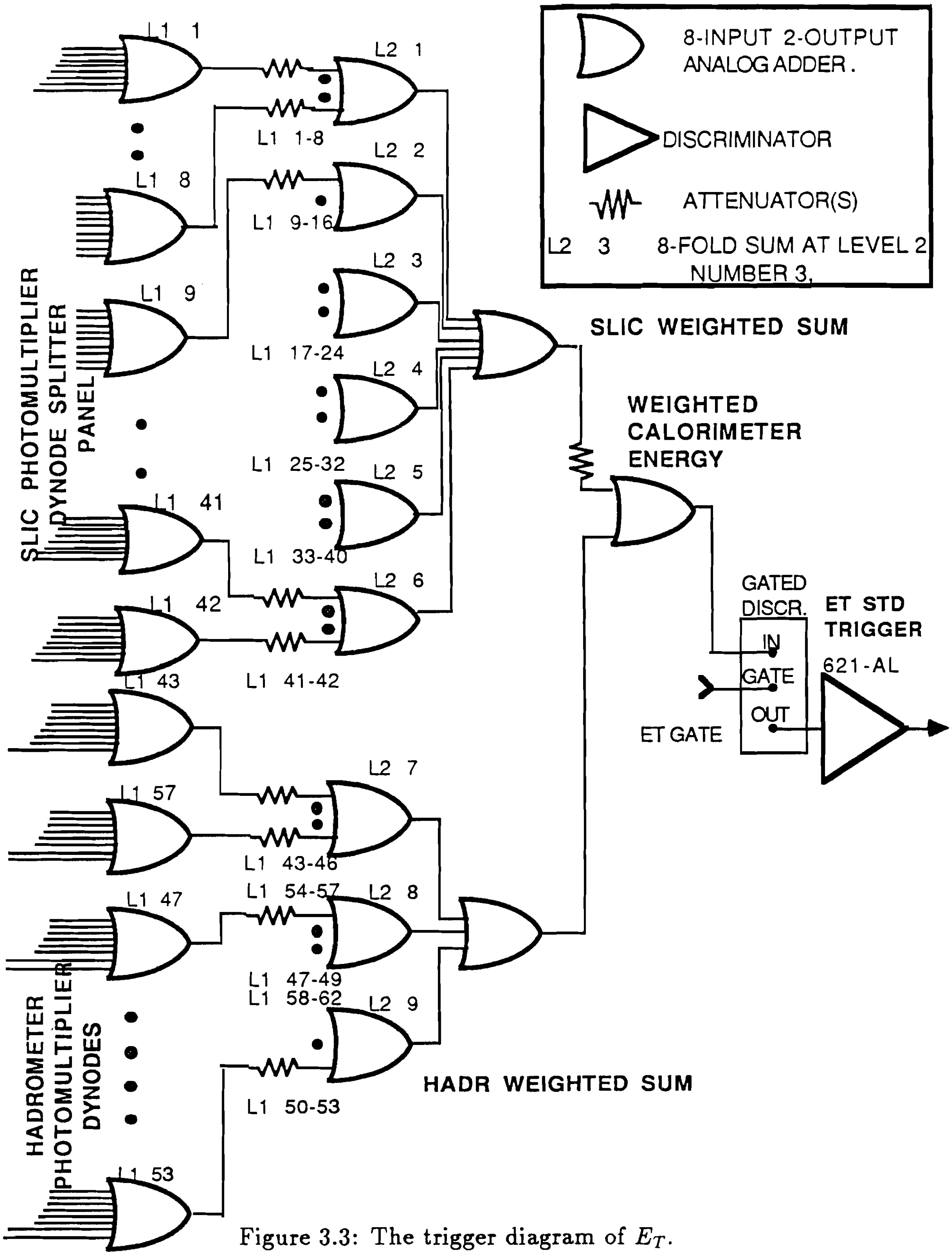

Figure 3.3: The trigger diagram of E_T.

($D^{\pm}$ and $D^0/\bar{D}^0$). This is discussed in Chapter 6. Also, it allowed good acceptance over a large range of x_F.

We also took 10 calibration triggers for each spill. The calibration events contained informations such as the pedestals of the phototubes.

3.2 Data Aquisition System

The data aquisition[28][34] system collected the digitized data of events from CAMAC modules and merged them onto tapes.

Figure 3.4 depicts the salient components of the data acquisition system. The data from the detectors were first digitized by the CAMAC modules and were read out by the Smart Crate Controller (SCC) modules. The SCC modules were built at Fermilab based on Motorola 68000 chips. Each SCC sent its data to a dedicated VME[1] Readout Buffer. An Rbuf allows events to pour in at one end while being read out at the other. Hence, all crates were read out at the same time. Two of the 16 ACP (Fermilab Advanced Computer Project) processors were assigned to read seven Rbufs. The other 14 ACP modules were used to weed out corrupted events, to format the accepted events and to place them in output buffers. The events from the output buffers were either written to tape or sent to an online event pool for monitoring. An ACP processor is a VME module with a 17 MHz Motorolla 68020, a 68881 coprocessor, and 2.0 MB (Mega Byte) on board memory. These Motorolla processors have a .7 MIPS (Million Instructions Per Second) computing power. About 1.4 Mb of the memory was used as input buffer, giving a total buffering capacity of 22.4 MB for the 16 ACP modules. At a full rate of 1.4 MB/sec, the data acquisition system took about 30 MB of data during the 22 second spill. However, we could only write 10 MB to tape during the spill, so the other 20 MB had to be stored in the input buffer, and were dumped to tape between spills.

The highest level of control resided in the TPL VAX11/780. It ran the System Controller program which served as the operator interface to the VME data acquisition system. All commands such as "start" and "stop" were issued through the

---

[1] VME stands for Versa Module Europe.

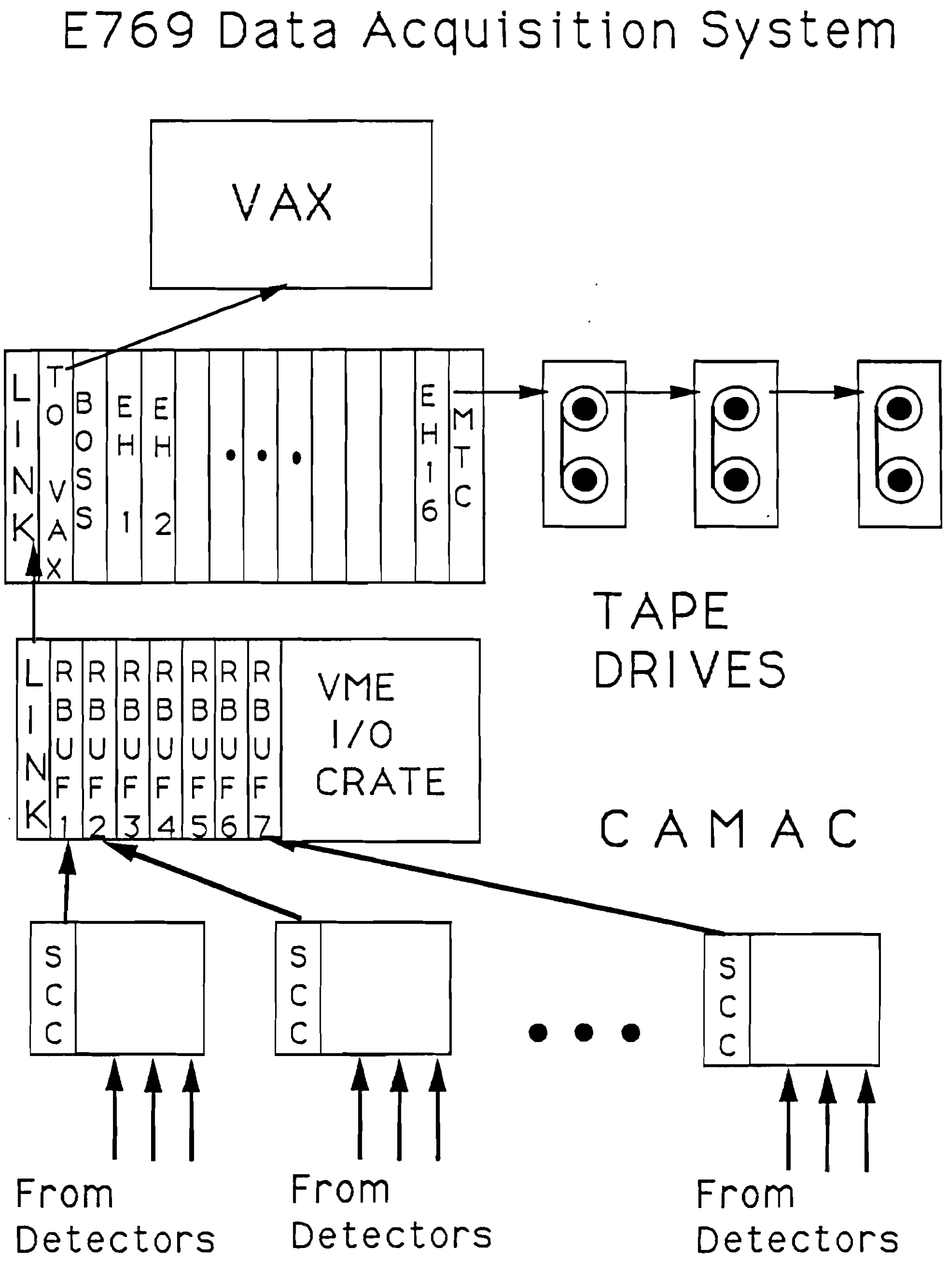

Figure 3.4: E769 data acquisition system[34].

VAX.

The parallel processing of data in each of the CAMAC crates made our data aquisition system 4 times faster than the E691 system which read out the crates serially. In addition, exploiting the time between spills for dumping out events stored during the spill to tape made it possible to take 12,000 9-track tapes during the nine month running period. As mentioned earlier, the data acquisition system was able to take 1.4 MB/sec or 400 events/sec since a typical E769 event has 1800 16-bit words, which meant a 9-track tape was filled every 5 minutes.

3.3 Monitoring of the Apparatus

We took data from the beginning of June 1987 until the end of the fixed target run in early February 1988. We collected 400 million triggers (mostly E_T) on more than 12,000 9-track tapes.

Besides changing tapes, the physicists on shift also had to do a check list which included checking the gas pressures and voltages for the detectors such as the DISC, TRD, SMD's, PWC's, Čerenkov counters, calorimeters and drift chambers. A check-tape job (a computer program) was also required to be run every shift on a newly filled tape to plot the hit distributions for the tracking detectors, and the phototube pulse height distributions for the Čerenkov counters and calorimeters. If any of these distributions deviated from its nominal one, the experts were called in to investigate the problem.

There were many online monitoring programs called DAPs (Detached Analysis Process) for various detectors, each could be run on line using events coming from the event pool to monitor an individual detector.

There was also an alarm program which printed out messages on a dedicated monitor if the critical voltages or gas pressures walked away from their nominal values.

3.4 Maintaining the SMD System

As discussed in the previous chapter, the SMD's are a complicated system which consisted of nearly 9,000 strips, 2,300 preamplifier cards, 1,200 readout cards and eight CAMAC Nanoscanners.

The performance of the preamplifier and readout cards depended on the reliability of the power supplies. The voltages of these power supplies located in the experimental hall were checked periodically. Furthermore, an alarm module automatically rang a bell in the control room if the voltages departed from their nominal values by more than 0.2 Volts for most of the power supplies. The voltages, which the threshold and delay of the SMD readout cards depend on, were held within 50 mv from their nominal values.

In the beginning of the run, the SMD planes and their preamplifiers, and the readout cards for the E691 planes were overheated due to poor ventilation. The temperature increase resulted in higher leakage currents in the detectors, higher noise and failure rate of the readout cards. To solve the problem, a ventilation system consisting of 10 pipes was installed as shown in figure 3.5. Each pipe had slit cut into its sides which allowed air to be blown over the readout cards for the E691 planes due to fans installed at both ends of the pipe. Also, an air conditioner blew cold air into the SMD area.

The leakage currents of the silicon detectors were measured every week. Typical currents were about 2 na per strip for the Enertec detectors and 20 na per strip for the Micron detectors. The strips which caused high leakage currents in some planes were disconnected before the run.

The noise rates of the SMD planes were constantly monitored by taking triggers when the beam was off. Most channels had noise rates (defined as the number of noise hits per trigger) lower than 0.3%. The channels with noise rate higher than 1% were tracked down and their corresponding readout card were taken out and checked. A noisy channel often could be fixed by resetting the threshold or replacing the whole readout card. The efficiencies of the SMD planes were monitored online by making hit profile plots from the data in the event pool. A channel which consistently showed

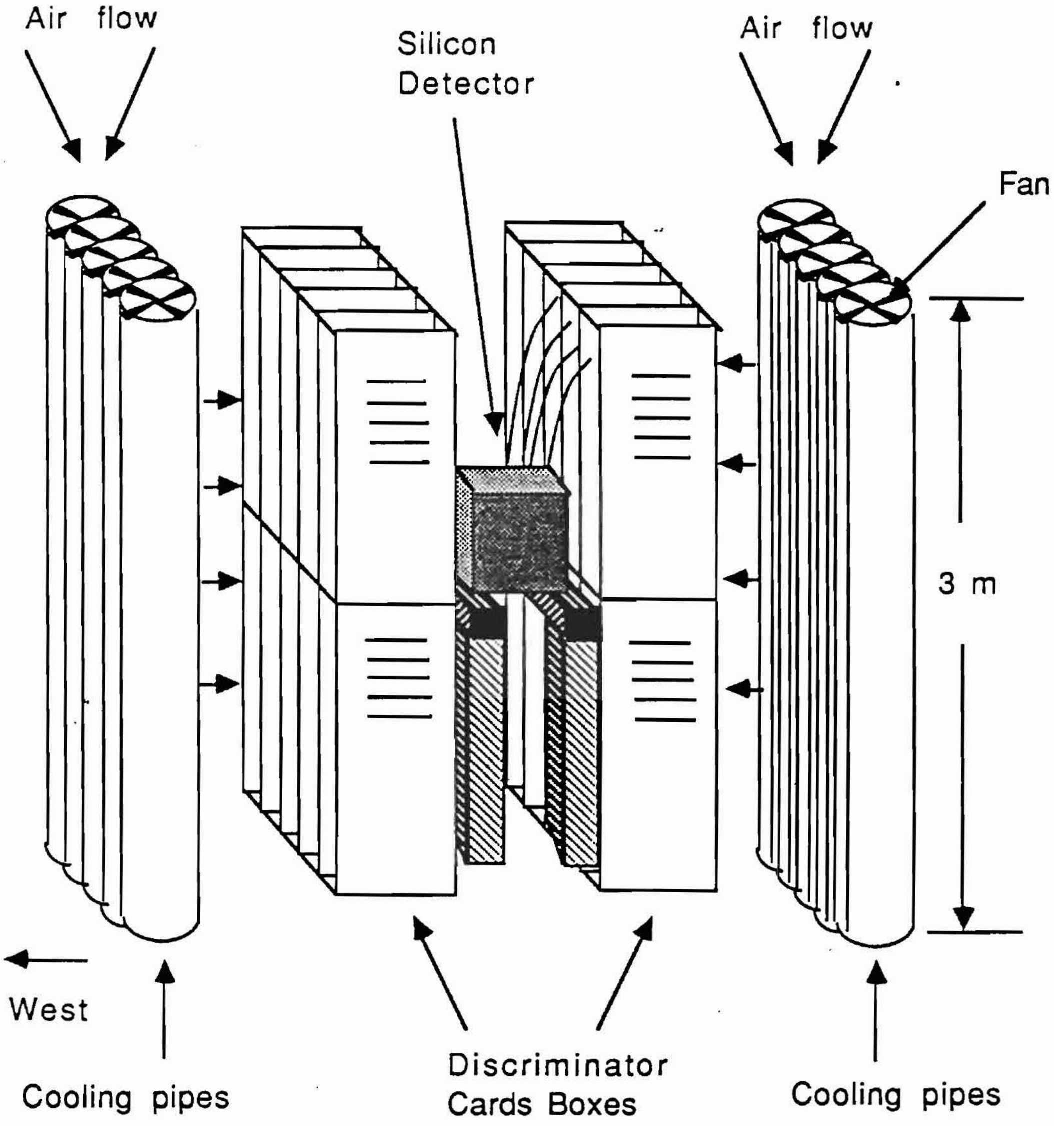

Figure 3.5: The ventilation system for the E691 SMD readout cards.

lower numbers of hits than the neighboring channels was tracked down and fixed the same way as a noisy channel. Some of the bad (noisy or inefficient) channels were caused by preamplifier failures. About a dozen bad channels in nine E691 planes and another dozen in the two downstream 25 μm pitched planes were due to bad preamplifiers. To replace a preamplifier card for a E691 plane, it was necessary to move the target and interaction scintillation counter out of the way to open the light tight SMD fixture. This procedure was too time consuming to attempt during the run. However, the preamplifier boxes for the beam planes AX and AY were easier to access, so replacements were made two times during the run. Over all, the SMD system performed very well. The noisy and inefficient channels were only about 3% of the total.

As shown in figure 3.6, a special apparatus was set up to test and set the threshold of the readout cards. The major components of the test setup were the pulse generator, a test fixture containing the 2 four channel preamplifiers, a register box and DC low voltage power supplies. We used a 10 KHz square wave with a peak-to-peak amplitude 0.85 Volts (0.43 Volts for E769 SMD readout cards). The pulses were attenuated by a factor of 1000 before they reached the preamplifier to simulate the real signal. The register box was used to generate the digital patterns necessary to operate the readout cards and in addition, counting the number of pulses which passed through the discriminator card.

The same test setup was also used to repair the readout cards. Figure 2.13 and Figure 2.14 show the circuit diagrams of one channel from the SMD readout cards for the E691 planes and 25 μm planes respectively. As discussed in the last chapter, the components on the left side of the dashed line were modifications to convert the circuit originally used for reading out MWPCs (Multi-Wire Proportional Chamber). As shown in Figure 2.13, a single transistor circuit was used to receive signals sent via transmission line from a preamplifier. The potentiometer was used to set the threshold. The opamp (operational amplifier) further amplified the signal. After that, the signal was delayed for 750 ns by a monostable multivibrator. The delay allowed the trigger decision to be made. Then, the delayed signal set a latch in the shift register to be read out by a CAMAC Nanoscanner. As discussed in section 2.5,

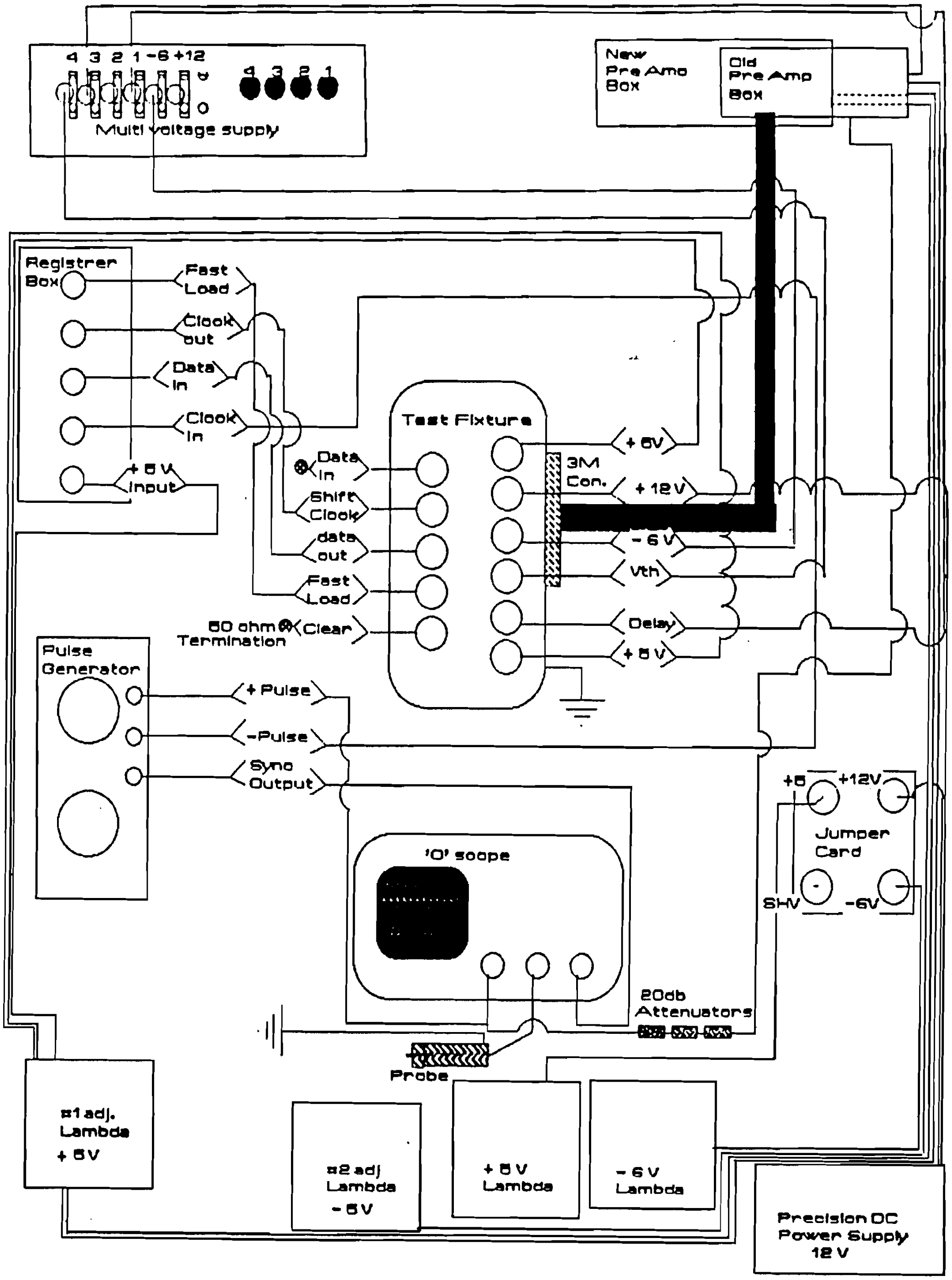

Figure 3.6: The test setup for the SMD readout cards.

the front end of a readout card channel for a 25 μm plane used a comparator instead of a transistor to extract a differential signal from a preamp. This was the only difference between the two types of cards. The failed components were found by tracing the test signal through the circuit. The most common failure was the breakdown of the diodes before the differential comparator.

I found that the noise levels were reduced by a factor of 2-10 by adding a 20 pf capacitor in parallel with the two diodes at the input of the differential comparator to bypass the high frequency noise to ground.

3.5 Efficiencies of the SMD Planes

The efficiencies of the SMD planes are the necessary ingredients for monte carlo simulation of the spectrometer. Therefore, it is important to determine them in order to get physics results. In this section, we present the efficiencies of the SMD system at different times during the run. The efficiencies of the 25 μm planes and the E691 planes were determined separately using different methods.

3.5.1 The Efficiencies of the E691 SMD's

The PASS1 data [2] (the transverse energy triggered events) tapes were used to determine the efficiencies for the E691 SMD planes. To measure the efficiency of an E691 SMD plane, say X1, we first selected good quality tracks based on the criteria summarized in table 3.1. The tracks were required to have hits in all other 8 E691 SMD planes according to the hit array[3], momentum above 10 GeV, track angle between 2 and 100 milliradians, and χ^2/DOF below 5 where DOF is number of degrees of freedom for the track. We then calculated the frequency that the plane X1 had hits according to the hit array corresponding to those tracks. Hence, the efficiency of X1 was number of 9 hit tracks (X1 had hits) divided by the sum of 9 hit tracks and 8 hit

---

[2] PASS1 data were intermediate output of the reconstruction. They contained the reconstructed track and momentum information, and the raw data types.

[3] The hit array indexed by the track number and plane number gave the hit number on a SMD plane for a given track.

tracks (X1 did not have hits).

The number of SMD hits	> 8 (out of 9)
Momentum (GeV)	> 3
Angle (radian)	> 0.002 and < 0.10
χ^2	< 5

Table 3.1: The cuts on tracks for the E691 SMD planes.

3.5.2 The Efficiencies of the 25 μm SMD's

For the 25 μm SMD planes, we had to use a different method because the hit array did not contain tracking information for the 25 μm SMD planes. This was because the PASS1 tapes were reconstructed using the E691 style code. As I discussed in the last chapter, E691 did not have these 25 μm planes.

We used the raw beam track tapes to determine the efficiencies of the 25 μm planes. The advantage of using the beam tracks was that there was only one 250 GeV beam track going through the SMD planes in each event. There was little ambiguity about the reconstructed tracks. Furthermore the multiple scattering for the beam track was much smaller than the tracks in data events. In order to evaluate the efficiency of a 25 μm SMD plane, say AX, we first reconstructed 3 hit tracks using three E691 SMD planes for x and y views, secondly combined the two tracks to calculate the intersection with each plane in the v view and thirdly searched for a hit in the window of ± 2 strips from each intersection. When the supporting hit was found in each of the v view planes, a 9 hit track was obtained. Then, we only selected 9 hit tracks with χ^2 less than 5 and extrapolated them to AX. We calculated the intersections with AX, namely, their predicted positions on AX, and looked for hits in the windows of $\pm$ 5 strips around the intersections. We obtained the frequencies for getting no hit (n_0), a single hit (n_1) and two hits (n_2) out of the total number of extrapolated tracks (n_t) in the windows. The reason one could get more than one hit in a window was due to noise. The reason we chose to reconstruct tracks using only

E691 SMD planes was because the E691 SMD planes generally were more efficient and less noisy.

Assuming the efficiency of a 25 μm SMD plane is ϵ, the probability for getting a noise hit is η. The probabilities for getting no hit p_0, one hit p_1 and two hits p_2 can be expressed in terms of ϵ and η. They are:

$$p_0 = (1-\epsilon)(1-\eta) = n_0/n_t$$

$$p_1 = (1-\epsilon)\eta + (1-\eta)\epsilon = n_1/n_t$$

$$p_2 = (1-\epsilon)\eta^2 + \eta\epsilon = n_2/n_t$$

To solve for ϵ and η, only two equations were needed. The equations for p_0 and p_1 are used to get the simplest equation:

$$\epsilon_1^2 - (p_1 + 2p_0)\epsilon_1 + p_0 = 0$$

where,

$$\eta = 1 - p_0/\epsilon_1$$

$$\epsilon = 1 - \epsilon_1$$

3.5.3 Results

Table 3.2 shows the efficiencies of the E691 SMD planes obtained from three tapes taken far apart in time. There were some variations from different tapes for the efficiency of a plane. The variations were small (within 3%) except for Y3. The last column in table 3.2 gives the efficiencies and their standard deviations averaged over those tapes. The only plane which had an efficiency below 90.0% was Y3.

Table 3.3 shows the efficiencies of the 25 μm SMD planes evaluated from three beam track tapes taken in a period in which most of the E769 data were accumulated. The efficiencies had fluctuations about 10%. The last column shows the efficiencies and their standard deviations averaged over these tapes.

The average efficiencies were 93% for the E691 planes and 73% for the 25μm pitched planes. The lower efficiency for the 25μm pitched planes was because the

Tape number	RI2310	RI5301	RI7303	Average
X1	0.928 ± 0.006	0.937 ± 0.011	0.936 ± 0.006	0.934 ± 0.005
X2	0.945 ± 0.005	0.934 ± 0.012	0.930 ± 0.006	0.936 ± 0.007
X3	0.883 ± 0.007	0.930 ± 0.011	0.904 ± 0.006	0.906 ± 0.019
Y1	0.934 ± 0.006	0.939 ± 0.012	0.950 ± 0.005	0.941 ± 0.007
Y2	0.961 ± 0.005	0.954 ± 0.010	0.960 ± 0.005	0.958 ± 0.004
Y3	0.816 ± 0.008	0.885 ± 0.015	0.857 ± 0.008	0.853 ± 0.029
V1	0.934 ± 0.006	0.936 ± 0.012	0.957 ± 0.005	0.942 ± 0.011
V2	0.960 ± 0.004	0.961 ± 0.009	0.961 ± 0.005	0.961 ± 0.003
V3	0.951 ± 0.005	0.939 ± 0.011	0.939 ± 0.006	0.943 ± 0.006

Table 3.2: The efficiencies of the E691 SMD planes.

Tape number	QA183	QA218	QA231	Average
AX	0.820 ± 0.022	0.727 ± 0.023	0.739 ± 0.026	0.762 ± 0.044
AY	0.732 ± 0.026	0.654 ± 0.025	0.788 ± 0.023	0.725 ± 0.057
BX	0.832 ± 0.021	0.671 ± 0.025	0.721 ± 0.027	0.741 ± 0.069
BY	0.674 ± 0.029	0.791 ± 0.020	0.657 ± 0.029	0.707 ± 0.061

Table 3.3: The efficiencies of the $25\mu m$ SMD planes.

gains of their preamplifiers were purposely lowered to reduce the noise level. This was necessary because the noise rates on the 25 μm planes were too high under normal operating conditions due to improper shielding.

3.6 Resolutions of the SMD Planes

For a position detector with wire spacing or pitch p, the theoretical standard deviation (resolution) of the measured position of a particle trajectory on the detection plane from its true position is $p/\sqrt{12}$. However, in reality, the resolution of a detector is always worse than the theoretical expectation due to noise, small errors in the alignment constants, multiple scattering and so on. It is important to understand the real resolutions of the detectors for doing monte carlo simulations and future detector developments. In the following, we present the resolution measurements of seven SMD planes and the comparison to the theoretical values.

A PASS1 beam track tape PQ0032 was used for the resolution study. The algorithm we used to determine the resolution is similar to the method we used to find efficiencies of the 25 μm SMD planes. To measure the resolution of an SMD plane, say X1, we first reconstructed tracks using other SMD planes except X1. We required the tracks satisfy the cuts on number of hits, χ^2/DOF and momentum as given in table 3.1. Then, we extrapolated the reconstructed tracks to X1 to obtain the intersections with X1. We calculated the difference of every measured hit position on X1 with the intersections and plotted its distribution. This distribution should peak at zero for the hits which correspond to the tracks, while it should be flat for other hits. This plot is called the residual plot for X1. The width (σ) of the peak is due to the contribution from the resolution of the measured coordinates (σ_m) and the resolution of the predicted coordinates (σ_p) with the following relation : $\sigma = \sqrt{\sigma_p^2 + \sigma_m^2}$. Our goal was to calculate σ_m from the this expression. The width of the peak σ was measured by applying a maximum-likelihood fit of a gaussian peak sitting on a linear background to the residual plot. As an example of this fit, we show the residual plots for BX and X1 planes with the fits in Figure 3.7. The predicted error σ_p could be calculated from the error matrix of the track parameters, but it depends on the σ_m's of other SMD planes. As a result, we had to compute σ_m through many iterations. For the first iteration, we used the theoretical expectation ($50/\sqrt{12} = 14.4$ microns) as the starting value σ_{m1} (1 denotes the first iteration) for the resolutions of the plane other than the one we want to compute. Then, we computed σ_p and solved σ_m for this plane. We repeated this procedure for other planes. Then, we obtained a set of σ_m's. We calculated the average $\overline{\sigma_m}$. For the second iteration, we assigned the starting value σ_{m2} with (σ_{m1} + $\overline{\sigma_m}$)/2 and repeated the same procedure. This process went on until the results converged. Then, within errors the solved σ_m's were equal to the values we put in.

Table 3.4 shows the measured σ's, σ_p's and calculated σ_m's for seven planes in x and v views. The final values for the resolution σ_m's are about 17 microns for the 50 μm planes. They are about 2.6 microns greater than the theoretical expectation

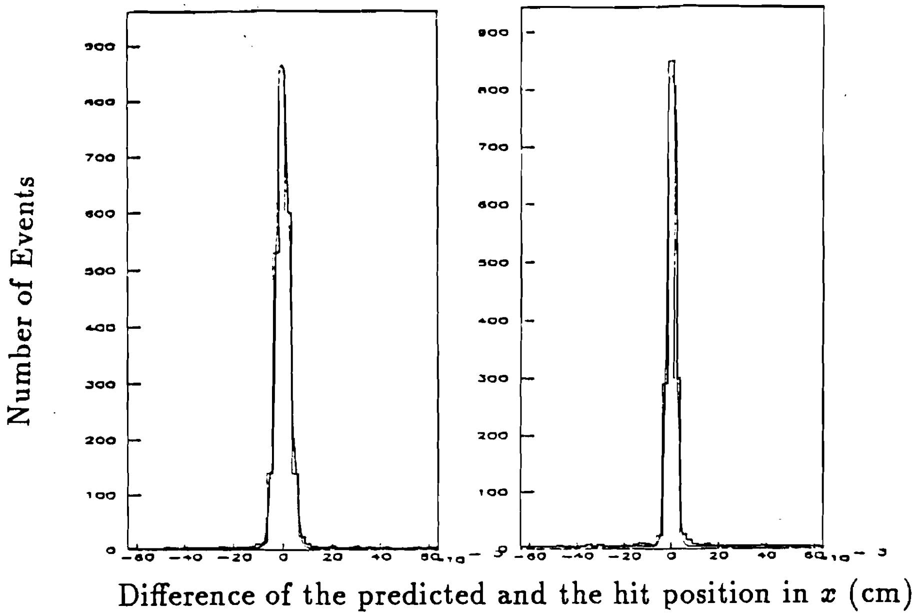

BX X1

Figure 3.7: The residual plots for BX and X1 with bin size of 25 μm. The units are in centimeters. The smooth curves are the results of the maximum likelihood fit using a function which is the sum of a gaussian and a linear function.

(14.4 microns). The measured σ_m for the 25 μm plane BX is 7.5 microns which is close to the theoretical expectation of 7.2 microns.

Plane	σ (μm)	σ_p (μm)	σ_m (μm)
BX	16.2 ± 0.4	14.3	7.5 ± 0.4
X1	25.3 ± 0.4	19.9	15.7 ± 0.7
X2	18.7 ± 0.4	8.4	16.7 ± 0.4
X3	22.5 ± 0.4	12.9	18.4 ± 0.5
V1	20.0 ± 0.4	10.9	16.5 ± 0.5
V2	19.8 ± 0.4	7.9	18.2 ± 0.4
V3	24.8 ± 0.5	17.5	17.6 ± 0.7

Table 3.4: The resolutions of the SMD planes.

Chapter 4

Data Reconstruction

In order to obtain physics results from data, the raw digital information recorded from the spectrometer must be converted to the physical properties of the produced particles such as energy momentum four-vectors, trajectory parameters and particle types. The conversion is called the data reconstruction.

We used the SMD planes, the downstream PWC planes and the drift chambers to measure the trajectories of the charged particles in the spectrometer. The momentum of a charged particle was calculated from its bend angles in M1 and M2. The direction of the bends revealed the charge of the particle. Given the particle's momentum, we obtained the particle type information from the responses of the Čerenkov counters. The topology of an event was established by the vertex reconstruction of the particle tracks in the SMD region. From the reconstructed electromagnetic and hadronic showers in the SLIC and hadrometer, we identified electrons, photons, muons and hadrons, and determined their energies.

We modified the E691 reconstruction code to include the added detectors, namely, the upstream and downstream SMD and PWC planes, the DISC and TRD.

We calculated the gains of the phototubes (the conversion factor from ADC counts to energy) from the muon calibration runs, before any reconstruction began. As mentioned in the Chapter 3, there were 10 calibration events taken per spill. The calibration events contained the pedestal information of the phototubes. The reconstruction program began by searching for at least 10 and up to 20 calibration events in a tape to calculate the average pedestal for each phototube. It also ran 1000 events to find the hot channels in the SMD planes and to determine the pion and proton peaks in the TRD plane count distribution. The tape was rewound and the real reconstruction began. The reconstruction program had PASS1, PASS2 and DST programs as in E691, but it also had an additional beam identification program. The PASS1 program performed the track reconstruction in three regions of the spectrometer (2 magnets naturally divided the spectrometer into 3 regions). The PASS2 program did the vertexing, calorimetry reconstruction and the particle identification. The raw data types were retained in the PASS1 output for PASS2. They were also retained in PASS2 output for caution. The DST (Data Summary Tape) program dropped out the raw data types, extracted the reconstructed information from PASS1 and PASS2, and repacked them into a compressed DST data format. The beam identification program assigned a beam particle with a probability of being a particular beam type ($\pi/K/p$) based on the DISC and TRD. Table 4.1 shows the size of the data at each stage of the reconstruction in unit of 9-track tapes.

Raw	PASS1	PASS2	DST
1	2	4	1/2

Table 4.1: Relative size of the data at different stages of the reconstruction.

4.1 Computing Demands

On average, it took 0.7, 0.4 and 0.03 seconds per event on the AMDAHL at Fermilab to run the PASS1, PASS2 and DST programs respectively. Because the AMDAHL only has 30 MIPS (Million Instructions Per Second) of computing power, it would require 12.3 years to fully reconstruct our total 400 million events from raw to DST format. Other Fermilab main frame computers such as the FNAL VAX cluster with 5.5 MIPS and the CYBER with 17 MIPS clearly could not meet our computing demands. The microprocessor farm, ACP (Advanced Computer Project) system which has 400 nodes with 0.7 MIPS on each, could satisfy our needs. Unfortunately, we could only use 130 nodes on average, because the system was shared with other experiments at Fermilab. Had we done the data reconstruction only on the ACP nodes available to us, it would have taken us almost four years. Obviously, this was not acceptable.

Fortunately, the 4D/240S computer manufactured by Silicon Graphics was available at the time. A 4D/240S is based on the UNIX operating system using MIPS 25 MHz R3000 chips. It has four processors with 16 MIPS of computing power on each. It also uses the 8 mm 1.2 GB (Giga-Byte) exabyte cassettes instead of the much larger 120 MB 9-track tapes.

We persuaded Fermilab to buy four 4D/240S computers. Using these and our share of the ACP system, we finished our data reconstruction in a year.

4.2 PASS1

PASS1 had two major programs: S1234 and SESTR. S1234 reconstructed tracks originating from the target while SESTR was responsible for searching for tracks originating downstream of the SMD planes such as the tracks from the decay of $K_s^0 \to \pi^+\pi^-$ and $\Lambda^0 \to p\pi^-$.

We started the track finding from the E691 planes[1] by first looking for 3 hit tracks in each of the three views x, y and v. With a set of three hit tracks in two views, we searched for matching three hit tracks in the third view. Thus, we found the 9 hit SMD tracks. We used hits on D1 and the downstream PWC planes to help the views with less than 3 SMD hits. Thus, we also picked up the tracks with less than 9 SMD hits. The minimum requirements to start a track were that there were more than 6 hits in the SMD planes and there was at least one hit in each view. After an initial track was found, it was extrapolated into the two downstream 25 μm SMD planes (BX and BY). The corresponding hits were found within the appropriate windows around the predicted locations on these planes.

---

[1] The reason that the two downstream 25 μm SMD planes were not included in the initial track finding was because of their lower efficiencies and higher noise rates than the the E691 planes.

We fit the track to a straight line using all the SMD hits by minimizing χ^2 expressed as:

$$\chi^2 = \sum_{i=1}^{n} \frac{(p_i^p - p_i^m)^2}{\sigma_i^2} \tag{4.1}$$

where p_i^p is the predicted position of the fitted track at the i^{th} plane and p_i^m is the position of the found hit. The number n (=11) is the total number of SMD planes. The hits in the PWC and D1 planes were only used for pattern recognition and not in the fit. This was because the PWC and D1 planes had much poorer spatial resolutions (about 300 μm versus 15 μm) than the SMD planes. In addition, the typical transverse position errors the D1 and PWC planes due to multiple scattering in the SMD system were about 300 μm. Thus, including the PWC and D1 planes would not significantly improve the track fit. p_i^p can be expressed as:

$$\begin{aligned} p_i^p &= p_{0i} + x_i^p cos\phi_i + y_i^p sin\phi_i \\ &= p_{0i} + (m_x z_{pi} + b_x) cos\phi_i + (m_y z_{pi} + b_y) sin\phi_i \end{aligned} \tag{4.2}$$

where p_{0i} is the offset; z_{pi} is the z coordinate of the i^{th} plane; ϕ_i is the angle between the x axis and the coordinate axis of the i^{th} plane. For instance, ϕ_i equals $0^o, 90^o, 20.5^o$ for the x, y and v views respectively. We call p_{0i}, z_{pi} and ϕ_i the alignment constants for the i^{th} plane. I will discuss their computation in section 4.5. The parameters m_x (m_y) and b_x (b_y) are the slope and the intercept in x view (y view). They were calculated by solving equations of $\frac{\partial\chi^2}{\partial\alpha_k} = 0$ where k = 1, 4 and α_k is the k^{th} track parameter.

After the tracks were reconstructed in the SMD region, S1234 extrapolated them through both magnets into D3 in the y-z plane. We picked D3 instead of D4 because D3 had 12 planes while D4 only had 3. S1234 then matched the y coordinates of the XUV triplets from D1 to D4 along the extrapolated trajectory. The y coordinates were consistent with the straight line extrapolation because the magnetic fields didn't bend particles in the y direction. The x components of the matched triplets specified the horizontal bends by the magnets. Using a single-bend-point approximation for both magnets, the initial trajectories of the particles were established throughout the spectrometer.

S1234 then performed a more sophisticated fit of track parameters and momentum for each track candidate using the matched triplets in the drift chambers and the SMD track information, and taking the field maps of the two magnets into account. This is not a trivial problem because the track parameters are momentum dependent. The χ^2 in this case still had the same form as expression 4.1, except that p_i^p has an additional momentum dependent term QMD5/Qp_x, where Q is the charge of the particle and p_x is the x component of the particle momentum. The coefficient QMD5 was calculated using the initial track parameters, the track bends across the magnetic fields and the full field maps of the magnets. Then we determined determine the track parameters and track momenta by minimizing the χ^2. Finally, S1234 called a routine to eliminate tracks with too few hits in the SMD system or with large χ^2 from the track fitting, and those tracks that shared too many hits with other tracks.

The SESTR routine was called at this stage to search for the tracks originating downstream of the SMD system.

4.3 PASS2

4.3.1 SLIC and Hadrometer Reconstruction

Using measured pedestals from the calibration events and gains obtained during the calibration runs, the counter outputs were first converted into physical energies. The shower reconstruction program had two major parts. The first part found the energy groupings, called sectors, in the calorimeters. The second part generated a list of candidate particles with energy depositions which matched the sector energies.

The reconstruction program first found regions of contiguous energy depositions, i.e. the sectors (with energy e_i), in the calorimeters. The coordinates of each sector were determined from counters in xuv views. This position was then adjusted according to the known shower shapes. A stepwise regression fit[33] was used to merge the insignificant sectors into more significant ones. The transverse energy distribution of each sector was fit to a known electromagnetic shower shape plus a broader version of this shape used to approximate a hadronic shower. From this fit, we determined the nature of the sector energy deposition (whether it is electromagnetic shower or hadronic shower) and the energy deposition error (σ_i).

The least-squares formalism was used to find the best set of candidate particles. The energy (ϵ_j) deposited in the calorimeters by candidate particle j was determined by minimizing the χ^2 defined as:

$$\chi^2 = \sum_{i=1}^{n_s} \frac{(e_i - \sum_{j=1}^{n_p} \alpha_{ij}\epsilon_j)^2}{\sigma_i^2} \tag{4.3}$$

where n_s is the number of sectors, n_p is the number of particle candidates. The factor α_{ij} accounted for the fact that each sector could be due to showers of more than one particle. It was calculated based on the positions of the candidate sector and candidate particle. The calculation also included the physical and optical leakage between the right and left y view SLIC counters.

Because the SLIC has 20 radiation lengths, all of the electron and photon showers were nearly contained in the SLIC. On the other hand, the SLIC only has about 1.5 absorption lengths, so the hadronic showers tended to extend from the SLIC to the hadrometer. The electron and photon showers differ from the showers of charged and neutral hadrons by their narrow width and short longitudinal length. The showers due to the charged particles could be distinguished from the neutral ones because the charged particle showers could be associated with drift chamber tracks. Therefore, we could identify the showers due to electrons, photons, charged and neutral hadrons. Because a π^0 almost always decays to two photons, they were reconstructed by combining the two identified photons.

Muons with energies greater than 5 GeV penetrated through the calorimeter and were detected by the Back Muon Wall. Because they were close to minimum ionizing, they did not create either electromagnetic or hadronic showers as other particles did.

The identification of charged hadrons (π, K, p) were left for the Čerenkov reconstruction.

4.3.2 Čerenkov Reconstruction

The Čerenkov particle identification program calculated the probability of a charged particle of being an electron, muon, pion, kaon and proton. The calculation was based on the light observed in the phototubes with the particle's momentum and track information.

The program first converted the measured radiation in each phototube to the number of measured photoelectrons. Then, the program extrapolated a reconstructed track through both Čerenkov counters. If the particle was above threshold, it predicted the number of photoelectrons expected from this track of a given mass in each mirror. The radiation for this mass hypothesis could spread over more than one mirror. The total number of the predicted photoelectrons of the corresponding phototubes were added to be μ. The total number of the measured photoelectrons were N. The likelihood of the particle's having this mass is given by a compound Poisson probability distribution function:

$$P(N,\mu,b) = \frac{\mu^N}{N!}(1+b\mu)^{-N-1/b}\prod_{m=1}^{N-1}(1+mb) \tag{4.4}$$

where the parameter b expresses the deviation of this distribution from a pure Poisson distribution. It was taken as a constant throughout the run. Its determination was discussed in the NIM article[21].

The overall probability $CPRB_{i,j}$ that a given mass hypothesis i and track j are given as:

$$CPRB_{i,j} = P(N_{C1,j},\mu_{C1,j},b) \times P(N_{C2,j},\mu_{C2,j},b) \times A_i \tag{4.5}$$

where N and μ denote the measured and predicted number of photoelectrons from track j. The subscripts $C1$ and $C2$ represent the first and second Čerenkov counters. The *apriori* likelihood A_i represents the fraction that electrons, muons, pions, kaons, and protons are produced in our collisions. The normalization condition was then applied so that:

$$\sum_{i=1}^{5} CPRB_{i,j} = 1 \tag{4.6}$$

When the particle j was below the threshold for a mass hypothesis m_i, the expected number of photoelectrons μ_i was zero. If the measured number of photoelectrons was not zero, $CPRB_{i,j} = 0.0$ according to equation 4.4. The mass hypothesis m_i was eliminated. The relative probabilities for other mass hypotheses would be increased. If there was no observed photoelectrons, $CPRB_{i,j}$ was assigned to be equal

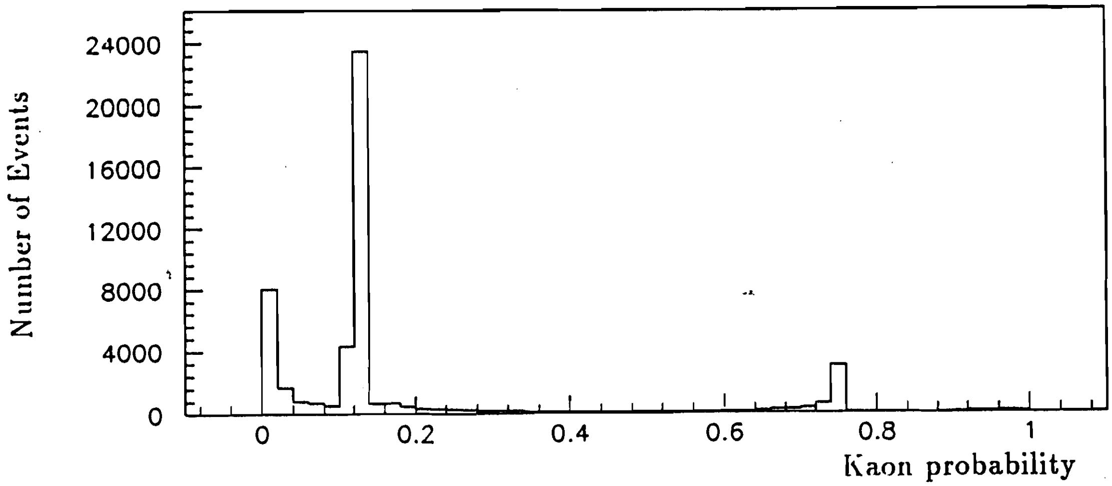

Figure 4.1: The kaon Čerenkov probability distribution.

to its *apriori* probability A_i because there was no Čerenkov information. When the particle's momentum were so high that it is above the thresholds of all the mass hypotheses, there would be no difference in the predicted numbers of photoelectrons for different mass hypotheses. Therefore, there was no Čerenkov identification either. The Čerenkov particle identification works best between the threshold momentum ranges, between 6 and 40 GeV for π/K separation for instance.

If the mirrors in question were shared by two tracks, $CPRB_{i,j}$ was assigned to the *apriori* A_i. When this happens, it means there is no Čerenkov identification. Figure 4.1 shows the $CPRB$ for kaons. There is an *apriori* peak at 0.12. For a positively identified kaon, its $CPRB$ should be greater than its *apriori*.

The calibration of the Čerenkov detectors was described in the NIM article[21].

The electron and muon identification by the calorimeters and muon wall were also used to eliminate certain mass hypotheses.

4.3.3 Vertex Reconstruction

The purpose of the vertex reconstruction was to obtain all vertices in an event. These vertices were the candidates for the primary vertex. It allowed track sharing. The

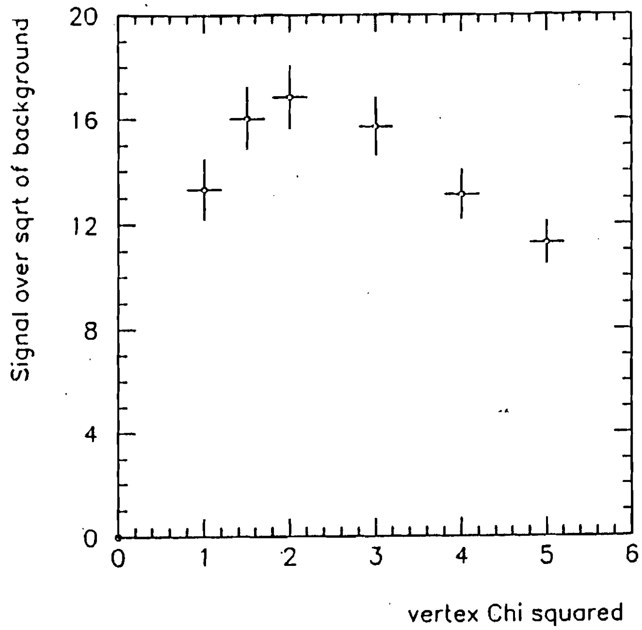

Figure 4.2: Signal over square root of background versus vertex χ^2/DOF cut.

general method was to find a two track vertex with χ^2 per degree of freedom (DOF) smaller than 2.0. The vertex reconstruction began by refitting tracks using the SMD hits only. It started with a two track vertex. Tracks were added to this vertex as long as $\chi^2/DOF < 2.0$. The χ^2 for a vertex was defined as the sum of the χ^2 (see equation 4.1) of each track with the constraint that all the tracks were forced to go through the vertex point. Thus, each track only had two parameters to vary. The number of degrees of freedom (DOF) equals to the number of hits subtracted by the number of constraints, i.e., the number of parameters used in the fit. There were three coordinates of the vertex and 2 track parameters for each track. Hence,

$$DOF = \sum_i^N n_i - (3 + 2N) \tag{4.7}$$

where N is the number of tracks in the vertex fit, n_i is the number of hits for the i^{th} track. The idea of the vertex fit was to find a vertex which minimizes χ^2/DOF.

It was tricky to pick the cut value for χ^2/DOF. If the cut value was chosen too small, the primary vertices might get lost. If the cut value was chosen too large, the charm tracks might get included in the primary vertices. This would result in the loss of charm. As an example, consider a vertex with three tracks. $DOF = 15$ for a typical

SMD track with 8 hits (out of 11 SMD planes). According to the χ^2 distribution for DOF=15 (from the particle data book), $\chi^2/DOF < 1.5$ guarantees with the confidence level of 93% that this vertex is good. For $DOF > 15$, the confidence level is higher than 93%. The value 1.5 is the minimum. However, we could not determine exactly where the optimal cut should be using the χ^2 distribution. We studied the signal significance of $D^\pm$ from the decay $D^\pm \to K^\mp \pi^\pm \pi^\pm$ as a function of the χ^2/DOF cut. The significance is defined as the ratio of the signal to the square root of background ($S/\sqrt{B}$). The signal S was obtained from the Monte Carlo and the background B from the data. The cut value 2.0 was chosen because it optimized the significance as shown in figure 4.2.

4.4 The DST Production on the AMDAHL

Historically, PASS1 and PASS2 were made to work before a working version of the DST program was available. By the time the DST program was working, we had created about 5000 PASS2 9-track tapes from the ACP system. To convert these PASS2 tapes to the DST tapes, the 30 MIPS AMDAHL equipped with 18 tape drives was the logical candidate to use because the DST program required little computation but many tape mounts.

According to table 4.1, one output DST tape was required for every 8 PASS2 input tapes. We acquired 10 maxidisks with 200 MB memory on each to store the DST job outputs which were later merged to the DST tapes. To ensure the smooth running of the DST production, a dedicated batch job queue was set up with the help of the Fermilab computing department. Because of the large number of tapes and job submissions involved, the book keeping became time consuming. We needed a part-time assistance, so we hired twin sisters Miss Bing and Yan Yang who were undergraduate students at Yale to handle this task.

4.5 SMD Alignment

4.5.1 Introduction

The alignment of the spectrometer, especially the SMD system, was very important because the accuracy of the reconstruction relied on it. In this section, I describe the alignment algorithm developed by Dr. Paul Karchin (see section 4.5.2) for finding the alignment constants for the SMD planes. In section 4.5.3, I discuss the conversion of the alignment constants defined in the local SMD coordinate system to the global alignment constants in the E769 standard coordinate system based on the drift chamber planes. There were 2 upstream and 11 downstream planes in the SMD system as discussed in chapter 2. The alignment constants of upstream and downstream planes were determined, using the same algorithm, separately for reasons discussed in the following section. The upstream SMD planes were moved twice for repair and once for the installation of the W target during the run which naturally divided the run into four periods for the SMD alignment.

4.5.2 Algorithm

Based on the SMD system, we define a local coordinate system with the z axis along the beam direction and through the center of each SMD plane, the y axis pointing up vertically and the x axis pointing west. Consider an x view SMD plane perpendicular to the z axis as a rigid body. To completely describe this plane, we need three position parameters (p_0, y_p, z_p) and three orientation parameters (ϕ_x, ϕ_y, ϕ_z) (the rotation angles around the three axes). These six parameters are the alignment constants for this plane. We need to determine those relevant to the coordinate (x) which this plane measures. Therefore, we can ignore the plane's y coordinate y_p because it doesn't affect the x coordinate. We can also ignore two rotation angles ϕ_x and ϕ_y because the changes around their nominal values only result in second order corrections to the x coordinate. We only need to determine the three alignment constants: the offset p_0, the location z_p and the orientation angle ϕ_z (or simply called ϕ) for this plane. Since an SMD plane only measures one view, the same argument holds for every SMD plane. Therefore, there are 3 × 13 alignment constants for the SMD system.

We cannot determine the absolute location, absolute distance scale and absolute angle of the SMD system using the track information alone. For the x view, we obtained the z_p locations of the x view planes X1 and X3 from the mechanical drawings. This is necessary because one z_p defines the absolute location and the other defines the absolute distance scale. The offsets of X1 and X3 planes were assigned with zeros. For the y view, the z_p locations and the offsets of the Y1 and Y3 planes were obtained the same way. We do not have to fix any alignment constants for the v view planes, because v view coordinates can be computed from x and y coordinates. The ϕ angles of the X1 and Y1 planes were set to zero which sets the reference for the ϕ angles of the other planes. Thus, we fixed 10 alignment constants out of 39 for the 13 SMD plane system.

We used the least-squares formalism to find the alignment constants which minimize the χ^2. Similar to equation 4.1, we define the χ^2 as:

$$\chi^2 = \sum_l \sum_{i=1}^{n} \frac{(p_i^p - p_i^m)^2}{\sigma_i^2} \tag{4.8}$$

where p_i^p is the predicted position from fitted track parameters at the i^{th} plane and p_i^m is the measured position. The total number of the SMD planes is n. The track index l is omitted from the variable p_i^p and p_i^m. Summing over many tracks increases the statistical significance. p_i^p is defined in equation 4.2.

The χ^2 is a function of the alignment constants (β's) because of p_i^p. We could find the alignment constants by solving the following equations:

$$\frac{\partial \chi^2}{\partial \beta_k'} = \sum_l \sum_{i=1}^{n} \frac{2(p_i^p - p_i^m)}{\sigma_i^2} \frac{\partial p_i^p}{\partial \beta_k'} = 0 \tag{4.9}$$

where $k = 1, 3n$ [2] and the β_k' is the k^{th} alignment constant.

However, it is hard to solve these equations for the β', because the χ^2 is not a linear function of β'. The key to simplifying this problem is to linearize the χ^2's dependence on β'. We write each alignment constant β' as the sum of the nominal

---

[2] The total number of alignment constants is $3n$, where n is the total number of SMD planes (each plane has three alignment constants).

value β and its deviation $\delta\beta$. Because $\delta\beta$ is small, p_i^p can be expressed in the following formula to the first order in $\delta\beta$:

$$p_i^p = p_{i0}^p + \sum_{j=1}^{3n} F_{ij}\delta\beta_j \tag{4.10}$$

where p_{i0}^p is the predicted position evaluated at $\beta\prime = \beta$ according to equation 4.2 on the i^{th} plane, and

$$F_{ij} = \frac{\partial p_i^p}{\partial \beta_j\prime} = \frac{\partial p_i^p}{\partial \delta\beta_j} \tag{4.11}$$

Now, p_i^p is a linear function of the new variable $\delta\beta_j$ where $j = 1, 3n$. The problem of finding $\beta_j\prime$ has been converted into finding $\delta\beta_j$.

In calculating F_{ij}, it is important to remember that the track parameters m_x (m_y) and b_x (b_y) depend on $\delta\beta_j$. In our computer program, F_{ij} was calculated numerically. For a small variation $\delta\beta_j$, each track was refitted and a new set of the track parameters were obtained. Equation 4.10 and 4.11 were used to calculate the new p_i^p and F_{ij}.

The equation 4.9 after inserting expression 4.10 for p_i^p becomes :

$$\begin{aligned} \frac{\partial\chi^2}{\partial\beta_k\prime} &= \sum_l \sum_{i=1}^{n} \frac{2(p_i^p - p_i^m)}{\sigma_i^2}\frac{\partial p_i^p}{\partial\delta\beta_k} \\ &= \sum_l \sum_{i=1}^{n} \frac{2}{\sigma_i^2}(p_{i0}^p + \sum_{j=1}^{3n} F_{ij}\delta\beta_j - p_i^m)F_{ik} \\ &= 0. \end{aligned} \tag{4.12}$$

Equation 4.12 leads to :

$$\sum_l \sum_{i,j}^{n,3n} \frac{F_{ij}F_{ik}\delta\beta_j}{\sigma_i^2} = \sum_l \sum_{i=1}^{n} \frac{(p_i^m - p_{0i}^p)F_{ik}}{\sigma_i^2} \tag{4.13}$$

It can be written as:

$$\sum_{j=1}^{3n} A_{kj}\delta\beta_j = B_k \tag{4.14}$$

where

$$A_{kj} = \sum_l \sum_{i=1}^{n} \frac{F_{ij}F_{ik}}{\sigma_i^2}$$

$$B_k = \sum_l \sum_{i=1}^{n} \frac{(p_i^m - p_{0i}^p)F_{ik}}{\sigma_i^2}$$

and $k = 1,\ 3n$.

Finally, we have obtained a matrix equation $A\delta\beta = B$. This equation was solved using the matrix inversion method: $\delta\beta = A^{-1}B$. The new alignment constants were $\beta_{j'} = \beta_j + \delta\beta_j$ ($j = 1, 3n$). For those fixed parameters, $\delta\beta_j$'s were set to zero.

In the actual implementation of the general algorithm described above, the alignment constants for the downstream and upstream SMD planes were determined separately. For the downstream alignment, we used the tracks from the E_T trigger events. We only used 11 ($n = 11$) downstream planes for the alignment, while ignoring two upstream SMD planes. No downstream planes were moved during the run, so one set of alignment constants for the downstream planes can be used for the whole run.

For the upstream alignment, we used the beam tracks to find the offsets and ϕ angles, while keeping the downstream SMD planes fixed. Because the beam tracks experienced little multiple scattering for their high momenta and they cover a circular area with diameter of about one centimeter, they gave a good determination of the offsets and the ϕ angles. However, we could not use the beam tracks to determine the z_p locations very precisely because their angles were too small (about 1 milliradian). Fortunately, some of our data events had interactions upstream of the beam planes, so we obtained the z_p locations from the upstream interaction tracks. We required at least 3 hits in both AX and AY planes to select the upstream interaction events.

In order to reduce false tracks in the alignment, we imposed cuts on the number of hits and the angle of the tracks. The cuts are shown in table 4.2 for the tracks used for the downstream alignment. In order to determine the z_p locations precisely, we used a minimum angle cut of 10 milliradians. The maximum angle cut was to ensure the tracks were within the geometric acceptance of the SMD planes. As for the beam tracks, we applied a maximum track angle cut at 2 milliradians to eliminate false and non-beam tracks. The cuts are shown in table 4.3. The cuts for the upstream interaction tracks are similar to those for the tracks used in the downstream alignment.

The alignment program was made of a track reconstruction routine and an alignment routine. The track reconstruction routine reconstructed tracks from 9 E691

SMD planes, extrapolated them into the 25 μm pitch planes. We searched for the hits in these planes inside a window of ± 200 μm from an extrapolated track, and then refit the track. The χ^2 is defined as the sum of the χ^2 of every track used. The alignment routine minimized the χ^2 by varying the alignment constants as described earlier in this section. The program gave a suggested correction and its error for each alignment constant. After a few iterations, the suggested corrections were within their errors. Then, the alignment constants were well determined.

Variables	Cuts
The number of hits	> 9 (out of 11)
Angle	> 0.01, < 0.10 radians
χ^2	< 5.0

Table 4.2: The cuts on tracks for the downstream SMD alignment

Variables	Cuts
The number of hits	> 9 (out of 13)
Angle	< 0.002 radians
χ^2	< 5.0

Table 4.3: The cuts on beam tracks for the upstream SMD alignment

Variables	Cuts
The number of hits	> 9 (out of 13)
Angle	> 0.01, < 0.10 radians
The number of hits in AX and AY	> 3
χ^2	< 5.0

Table 4.4: The cuts on upstream interaction tracks for the SMD alignment

4.5.3 The Relative Alignment Between the SMD system and the Drift Chambers

After the alignment constants were found in the local SMD system, they had to be converted into global alignment constants in the standard E769 coordinate system which was based on the drift chamber planes. To make the conversion, the relative alignment constants between the SMD and the drift chambers had to be determined. Both SMD and drift chamber systems were assumed to be two rigid bodies, so their relation could be defined by three position parameters (δX, δY, δZ) and three orientation parameters (δM_x, δM_y, $\delta\Phi$). The relation was expressed in terms of the above relative alignment constants:

$$\begin{aligned} \Phi_i &= \phi_i + \delta\Phi \\ Z_{pi} &= z_{pi} + \delta Z \\ P_{0i} &= p_{0i} + \cos\phi_i(\delta X + Z_{pi} * \delta M_x) \\ &+ \sin\phi_i(\delta Y + Z_{pi} * \delta M_y) \end{aligned} \tag{4.15}$$

where ϕ_i, z_{pi}, p_{0i} are the local alignment constants and Φ_i, Z_{pi}, P_{0i} are the global alignment constants. The relative alignment constants were determined using the same method of minimizing χ^2 to match tracks found in the SMD planes and those in the drift chambers.

4.5.4 Results and Discussion

As a check on the alignment constants, we made residual plots of the offset, ϕ and z_p for every SMD plane. The basic principle was to use the parameters of reconstructed tracks and two alignment constants to check the third one because they are related according to equation 4.2.

It was straightforward to make a residual plot for the offset. According to equation 4.2:

$$p_i^p = p_{0i} + x_i^p cos\phi_i + y_i^p sin\phi_i$$

$$= p_{0i} + (m_x z_{pi} + b_x)cos\phi_i + (m_y z_{pi} + b_y)sin\phi_i,$$

we calculated the predicted position p_i^p of a track with the i^{th} plane; we computed the difference δ_p of every measured hit position p_i^m on this plane with p_i^p. Then, we plotted the distribution of δ_p for many tracks. This plot is the residual plot for the offset. The quantity δ_p should be distributed around zero for the hits which correspond to the tracks, while δ_p form a smooth distribution for other hits. If the offset were off, the distribution would not peak at zero. This residual plot provided a very powerful check. This is important because there is always a danger of finding a local minimum of χ^2 using an analytical method.

It was a bit tricky to make the equivalent residual plot for the z_p location and ϕ angle. We first converted the above equation to:

$$z_{pi} = \frac{p_i^p - p_{0i} - b_x cos\phi_i - b_y sin\phi_i}{m_x cos\phi_i + m_y sin\phi_i}. \tag{4.16}$$

Then, we computed the quantity z_{mi} by replacing p_i^p with p_i^m in the above equation. More explicitly,

$$z_{mi} = \frac{p_i^m - p_{0i} - b_x cos\phi_i - b_y sin\phi_i}{m_x cos\phi_i + m_y sin\phi_i}. \tag{4.17}$$

where p_i^m is the hit position on the i^{th} plane. Again, we calculated and plotted the difference δ_z of z_{mi} and z_{pi}. Similarly, δ_z should be distributed around zero for the hits associated with the tracks. To make the residual plot for the ϕ angle, we need to solve ϕ_i from equation 4.2. Unfortunately, it is not a linear equation for ϕ_i. To make it linear, we first expressed ϕ_i as the sum of the nominal value ϕ_{i0} and its deviation $\delta\phi_i$. We then expanded $cos\phi_i$ and $sin\phi_i$ at ϕ_{i0} in terms of $\delta\phi_i$. We only kept the first order terms in $\delta\phi_i$. Thus, we obtained $\delta\phi_i$:

$$\delta\phi_i = \frac{p_i^p - p_{0i} - (m_y z_{pi} + b_y)sin\phi_{0i} - (m_x z_{pi} + b_x)cos\phi_{0i}}{(m_y z_{pi} + b_y)cos\phi_{0i} - (m_x z_{pi} + b_x)sin\phi_{0i}}. \tag{4.18}$$

We obtained the quantity $\delta\phi_{mi}$ from the above equation by replacing p_i^p with the hit position p_i^m. We then made a plot of $\delta\phi_{mi}$. This residual plot should have a peak at zero.

As an example, we show the three residual plots for AX in figure 4.3. They all have peaks at zero.

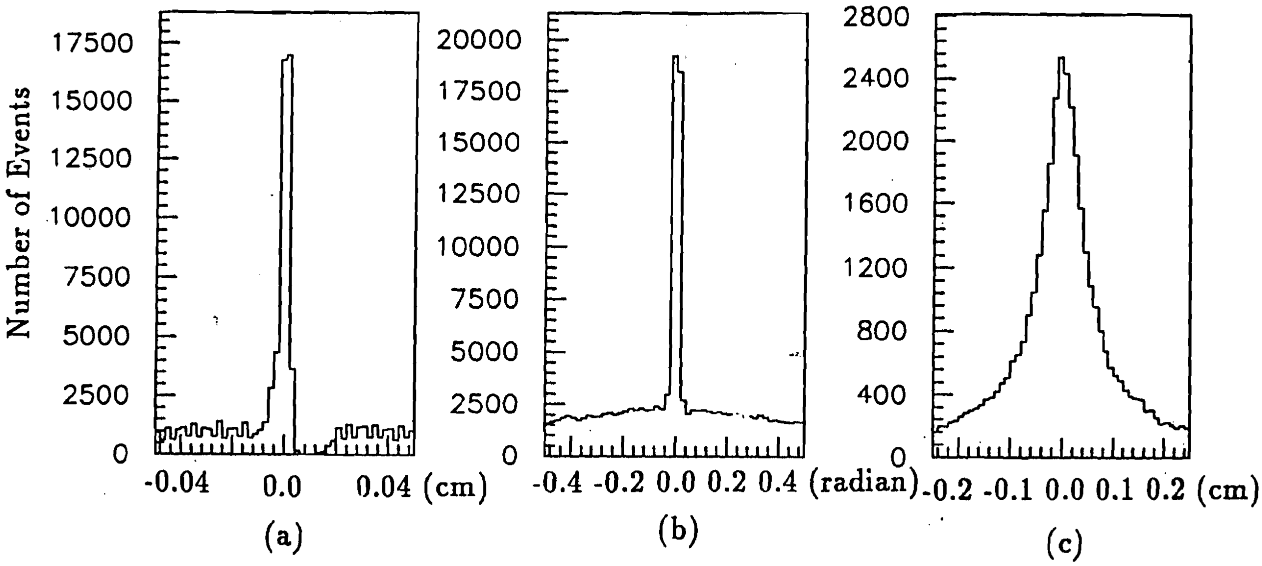

Figure 4.3: The residual plot of offset(a), ϕ(b) and $z_p(c)$ for AX

More than 1000 beam tracks and 10,000 upstream interaction tracks were used in finding the alignment constants for the beam planes. Over 20,000 tracks were used for the downstream alignment. We checked the consistency of the alignment constants by comparing the alignment constants as they were obtained from several different tapes within the same period. The variations were typically 2 μm for the offsets, 1 milliradian for the ϕ angles, 100 μm for the z_p locations of the downstream planes and 1 mm for the z_p locations of the upstream planes. The errors of the track trajectories due to these variations were much less than the errors due to the resolution of the SMD planes.

Chapter 5

Analysis

5.1 Introduction

In this chapter, I describe the algorithms and selection criteria (cuts) used to extract the $D^{\pm} \rightarrow K^{\mp}\pi^{\pm}\pi^{\pm}$ signal.

We used an effective mass method to observe charm. We first selected one K^{-} candidate and two π^{+} candidates from the reconstructed tracks to form a $D^{+} \rightarrow K^{-}\pi^{+}\pi^{+}$ candidate vertex. Then, we calculated the center of mass energy (also called the effective mass) of the three tracks. If these tracks are indeed the decay products of D^{+}, their effective mass should equal the mass of D^{+}, which is a constant. Therefore, there should be a peak at the D^{+} mass in the effective mass distribution. In order to avoid missing the real charm candidate, all possible combinations have to be considered. The combinations, which do not correspond to D^{+} decay products, form a smooth distribution.

In hadronic interactions, the charmed particles are rare and there are many final-state particles, so a large number of combinations have to be considered. In order to see the mass peak, we have to apply many cuts at different stages.

5.2 Algorithm and Selection Criteria

The first step of the analysis was to reduce the data in the DST format to a manageable quantity using two stripping programs: a "pair-strip" program, and a substripping program for $D^{\pm} \rightarrow K^{\mp}\pi^{\pm}\pi^{\pm}$. The strategy here is to get a large reduction factor using a few simple and efficient cuts, so the cuts applied were considered "loose" and not optimal. These two stripping programs gave a collective rejection factor of 300 over the DST output, so the final data sample could be stored on just a few exabyte cassette tapes. Then, we ran the analysis program on these tapes to extract the final $D^{\pm}$ signal. In each program, the cuts applied were progressively more stringent and closer to the optimal.

5.2.1 Pair Strip and Substripping Programs

Because one of the important signatures of charm is the separation of its decay vertex from the primary vertex in an event, we devised an algorithm to find a separated downstream pair vertex as a charm candidate vertex. This algorithm was implemented in the so called pair strip program. The program first picked the vertex with most tracks as the primary vertex in an event. Then, it formed a downstream candidate vertex out of any possible combination of two tracks which passed through the first magnet. The secondary vertex was demanded to satisfy the following requirements: (1) its $\chi^2/DOF < 5$ and (2) its location error σ_z (in z coordinate) < 1.8 mm. It was also required to be well separated from the primary vertex by having $SDZ > 6.0$, where SDZ, as defined in figure 2.10, was discussed in section 2.5. This cut was the most important of all because it signifies the separation of the charm vertex from the primary. Thus, most of the background was rejected by this cut.

In order to ensure that the two tracks in the secondary vertex were not from the primary vertex, both of them were required to be closer to their own vertex than to the primary vertex. To implement this cut, for the track i (i=1,2) from the secondary vertex, we computed the ratio of its distance (d_s^i) to the secondary vertex and that (d_p^i) to the primary. As illustrated in figure 5.2, the quantity RAT, called the ratio

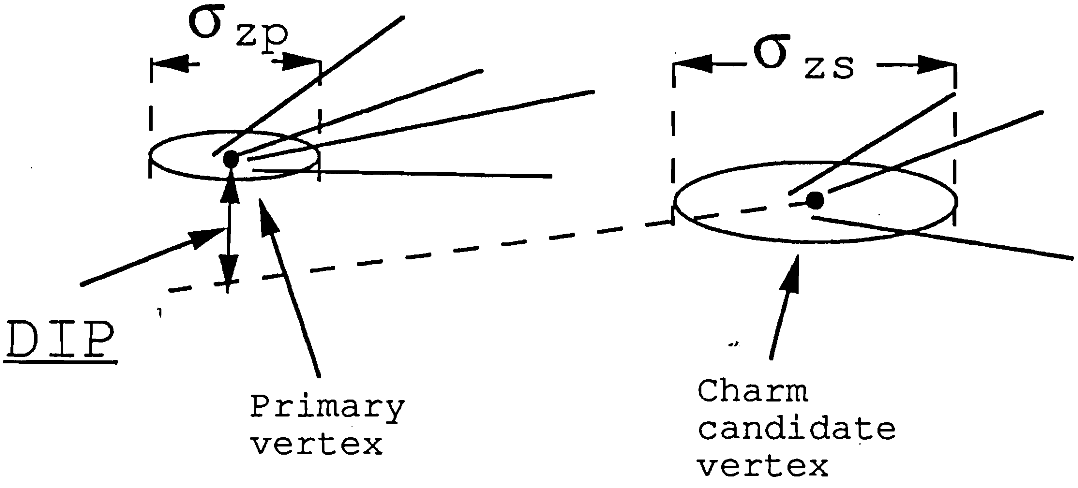

Figure 5.1: The definition of *DIP* cut.

cut, was defined as the product of the ratios from these two tracks. More explicitly,

$$RAT = \prod_{i}^{2} \frac{d_s^i}{d_p^i} \tag{5.1}$$

$$= \frac{d_s^1}{d_p^1} \times \frac{d_s^2}{d_p^2} \tag{5.2}$$

The ratio cut $RAT < 0.06$ was required. This means that each of the two tracks has to be on average four times closer to the secondary vertex than to the primary vertex.

One source of background is the secondary interactions which were induced by the primary tracks. The average transverse momentum for these secondary interaction tracks is about 0.3 GeV which is much smaller than that (1 Gev) of the charm particles. We computed the magnitude sum ($PT2DK$) of the the transverse momenta of the two tracks from downstream vertex relative to their direction of flight. We required $PT2DK$ be greater than 0.1 GeV. The first column of table 5.1 summarizes the cuts described above.

Because the pair strip program searched for any downstream pair vertex which passes several simple cuts described above, it was efficient for many decay modes such as $D^{\pm} \rightarrow K^{\mp}\pi^{\pm}\pi^{\pm}$, $D^0 \rightarrow K^{\mp}\pi^{\pm}$, $D^{\pm} \rightarrow K^{\mp}\pi^{\mp}\pi^{\pm}\pi^{\pm}$. Also, it gave a rejection factor of 14 over the DST tapes.

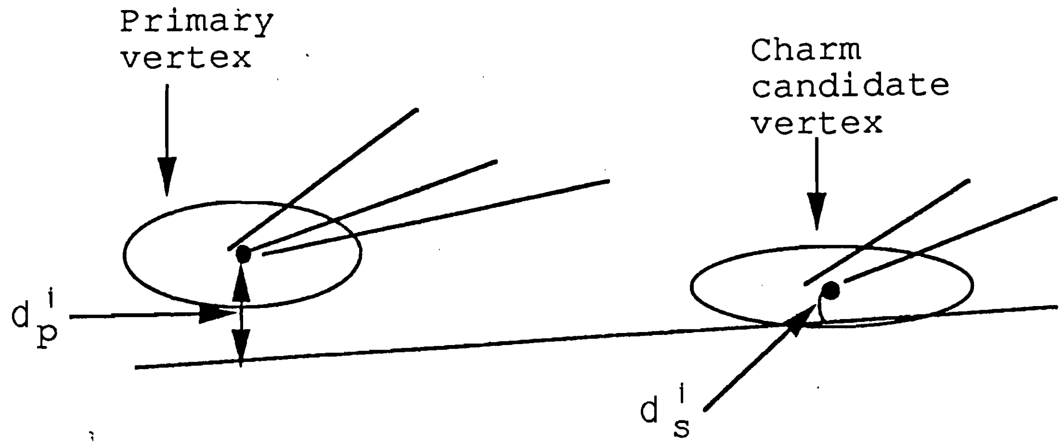

$$\underline{RAT} = \prod_{i=1}^{3} \frac{d_s^i}{d_p^i}, \quad \underline{RATIOD} = \mathrm{MIN}_{i=1}^{3} \frac{d_p^i}{d_s^i}$$

Figure 5.2: The definition of ratio cuts *RAT* and *RATIOD*.

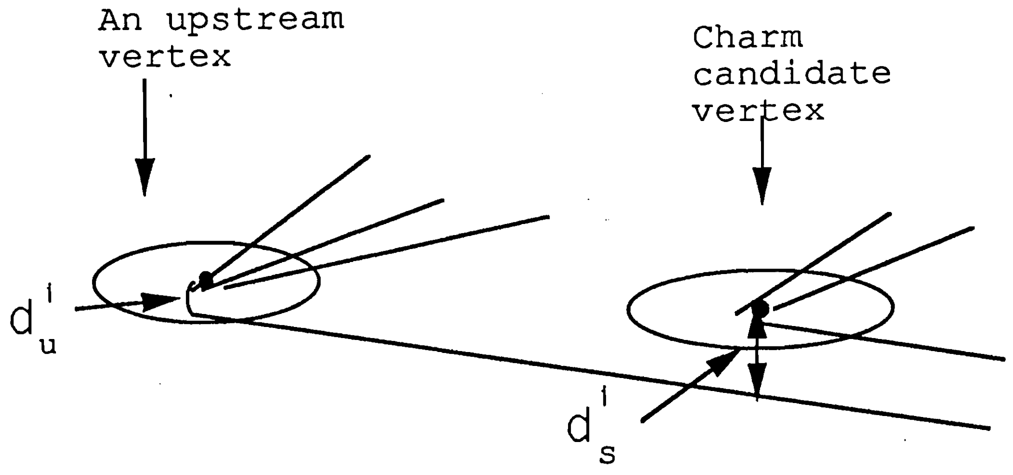

$$\underline{RATIOP} = \mathrm{MIN}_{i} \frac{d_s^i}{d_u^i}$$

Figure 5.3: The definition of *RATIOP*.

The substripping program for $D^{\pm} \rightarrow K^{\mp}\pi^{\pm}\pi^{\pm}$ applied more stringent cuts described above. It also used several additional cuts described below. It first formed a $K^-\pi^+\pi^+$ (also the charge conjugate state) candidate vertex from any possible three track combinations with their effective mass (EM) between 1.75 and 2.0 GeV. Then, it refit the vertices in the vertex list after removing these three tracks. Since the D^+ came from the primary vertex, the 3-vector momentum sum of the three tracks should point back to the primary vertex. We used this as the criterion to select the primary vertex from a list vertex candidates in an event. We computed the the impact parameter DIP [1] of the D^+ candidate relative to each upstream vertex. The vertex which gave the smallest DIP was chosen to be the primary vertex. The DIP cut is illustrated in figure 5.1. The $DIP < 200\ \mu m$ was applied in the program to reject the D^+ candidates which did not point back well to the primary. This is a loose cut, because the strategy here is to get a good rejection but not the optimization.

To reduce the contamination of the three prong charm candidates by 4 or more prong vertices, an isolation cut was introduced. To implement the cut, we considered each track in an event except the three candidate tracks and we calculated the ratio of the distance d_s of this track to the D^+ candidate vertex to the distance d_u to its own vertex. The isolation cut $RATIOP$, as illustrated in figure 5.3, was defined as the minimum of the ratios. It was required to be greater than 1.

Another source of contamination of the D^+ candidates was by the 2 prong vertices. Another type of ratio cut $RATIOD$ was introduced to reduce this background. The definition of $RATIOD$ is shown in figure 5.2. It was defined as the minimum of the ratios (d_p^i/d_s^i) for these three tracks. More explicitly,

$$RATIOD = min_{i=1,3}(\frac{d_p^i}{d_s^i}) \tag{5.3}$$

The cut $RATIOD > 1.0$ was imposed.

A minimal Čerenkov probability of 0.02 was required for the kaon candidate. This Čerenkov cut is discussed in detail in the next section. The analysis cuts applied in the substripping program are summarized in the second column of table 5.1.

---

[1] DIP is the symbol for the Impact Parameter

CUTS	PAIR STRIP	$D^{\pm}$ SUBSTRIP	ANALYSIS
SDZ	> 6.0	> 6.5	> 12.0
σ_z(secondary) (cm)	< 0.18	< 0.18	< 0.18
χ^2 (secondary)	< 5.0	< 5.0	< 5.0
RAT	< 0.06	< 0.06	< 0.06
$PT2DK$ (GeV)	> 0.1	> 0.1	> 1.0
EM (GeV)	-	> 1.75 and < 2.0	> 1.75 and < 2.0
$KPROB$ (for $p_K < 40.0 GeV$)	-	> 0.02	> 0.13
$KPROB$ (for $p_K > 40.0 GeV$)	-	> 0.02	> 0.10
DIP (cm)	-	< 0.02	< 0.01
χ^2 (primary)	-	< 5.0	< 5.0
$RATIOD$	-	> 1.0	> 3.0
$RATIOP$	-	> 1.0	> 1.0
DISC tag	-	-	non-kaons

Table 5.1: The cuts for pair strip, $D^{\pm}$ substrip and final analysis

5.2.2 Final Analysis Criteria.

For the final analysis, we selected the cuts to optimize the signal significance, i.e., to maximize $S_{MC}/\sqrt{S_{data} + B_{data}}$ where S_{MC} is the signal obtained from the Monte Carlo and $S_{data} + B_{data}$ is the sum of the signal and background from the data. The reason of using the Monte Carlo for the signal was because we could get high statistics. Thus, we do not tune on fluctuations.

As an example of this procedure, the $RATIOD$ cut was further extended and optimized at 3 as shown in figure 5.4, a plot of the quantity $S/\sqrt{S+B}$ as a function of $RATIOD$ cut. When we varied the cut $RATIOD$ to make this study, other cuts had been applied at their optimal values. For instance, SDZ had been cut at 12. Therefore, most of the background had been rejected by the SDZ cut. That is why $RATIOD$ only gives an additional 20% increase in $S/\sqrt{S+B}$. Similarly, we selected other cuts which are summarized in table 5.1.

Unfortunately, we could not apply the procedure directly for the kaon Čerenkov probability cut, because we measured an up to 15% discrepancy in kaon identification efficiencies at some momentum ranges between the Monte Carlo and the data. I

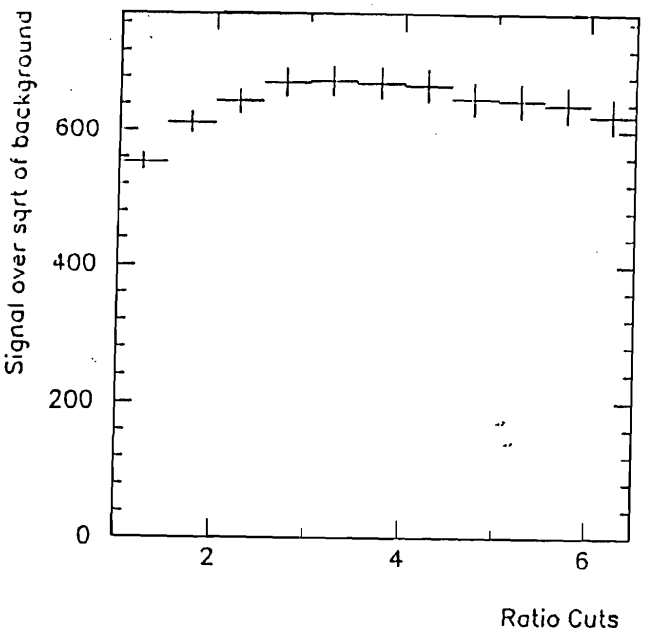

Figure 5.4: The significance of the signal as a function of *RATIOD* cut.

discuss this effect on the acceptance in section 6.5. Therefore, we had to choose this cut which maximizes $S_{data}/\sqrt{S_{data}+B_{data}}$ only based on data. As it was discussed in section 4.3.2, the π/K separation based Čerenkov counters works best for particle momentum between 6 and 40 GeV. We plotted the kaon probability distributions below and above 40 GeV in figures 5.5 and 5.6 respectively. We can see that there are many positively identified kaons below 40 GeV, while the number is much smaller above 40 GeV. For momentum below 40 GeV, we selected positively identified kaons with a *KPROB* cut of 0.13. For momentum above 40 GeV, We chose a *KPROB* cut of 0.1 which is below the *apriori* probability to reject candidates which are positively identified as non-kaons.

Since the DISC was set to tag K^- mesons for the negative beam, we required its kaon tagging information to select non-kaon induced triggers. The requirement was one of our standard analysis cut listed in table 5.1. Because our kaon tagging efficiency was only about 40% as mentioned in section ?.? 2.7.4, there is about 4% of kaons in the non-kaon triggers. There is also about 2% anti-protons in the non-kaon triggers. We took the non-kaon triggers as our π^- triggers with small contaminations from K^- and $\bar{p}$ beam particles.

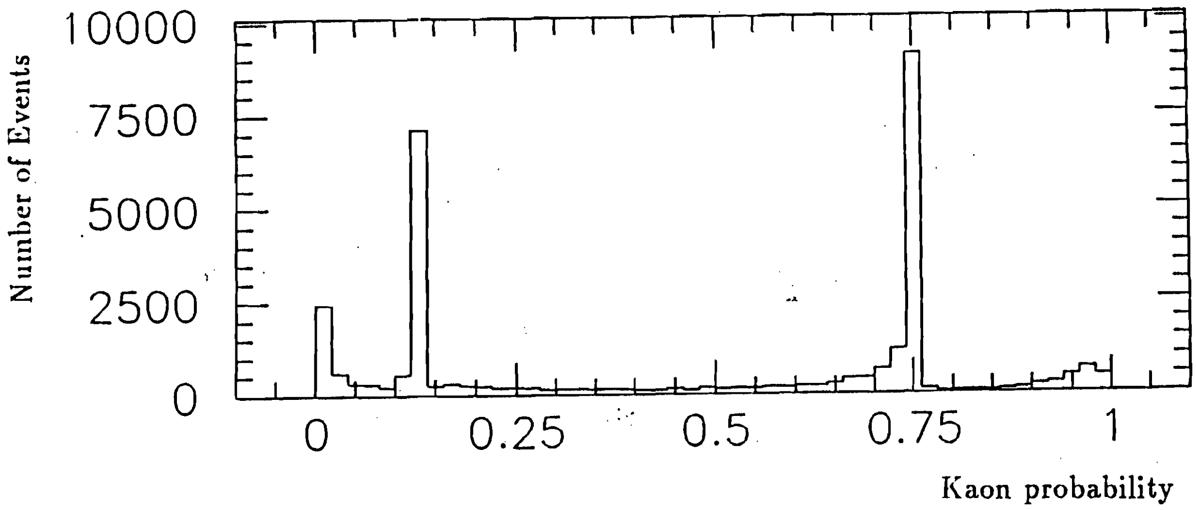

Figure 5.5: The Čerenkov probability distribution for kaons with momentum between 6 and 40 GeV.

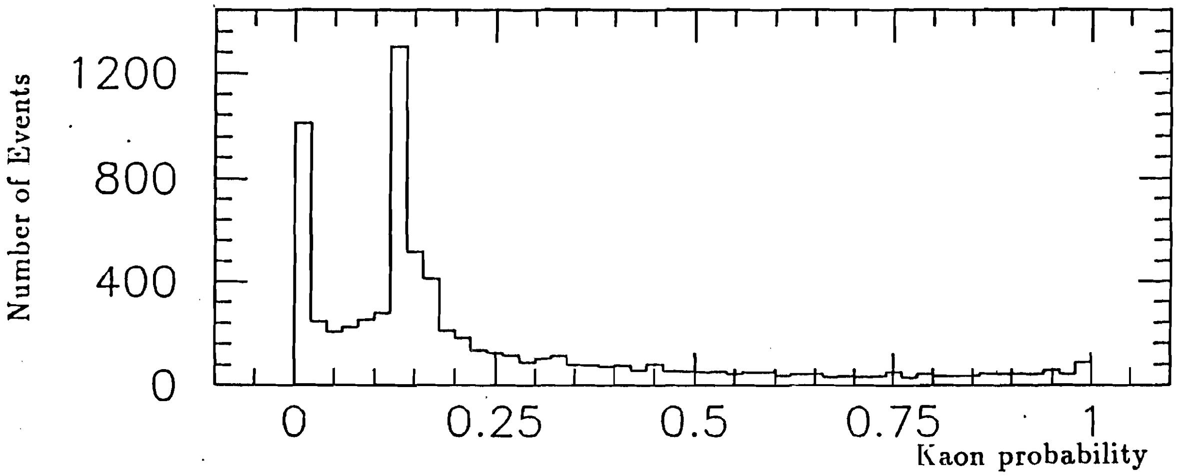

Figure 5.6: The Čerenkov probability distribution for kaons with momentum above 40 GeV.

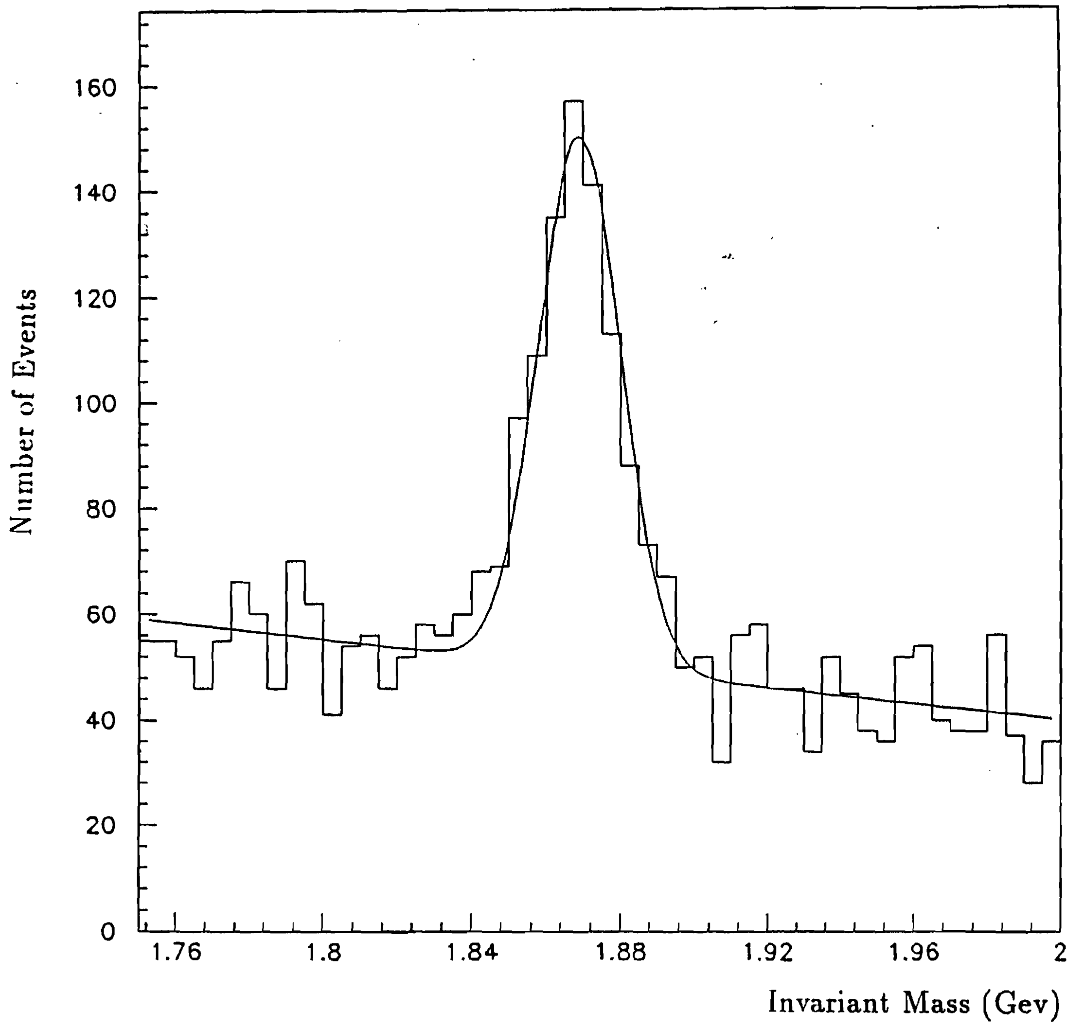

Figure 5.7: The effective mass plot of the $D^{\pm} \to K^{\mp}\pi^{\pm}\pi^{\pm}$ candidates from $\pi^{-}p$ interactions.

Using the cuts describe above, I obtained the mass plot shown in figure 5.7 with a peak at the $D^{\pm}$ mass of 1.869 GeV as expected. The finite width of the peak is due to the finite momentum resolution of the spectrometer. The contribution of the Breit-Wigner to the width is only on the order of 10^{-10} Mev since the charm lifetimes are about one picosecond, so it is negligible.

To estimate the signal, we performed a maximum likelihood fit using a gaussian signal with a linear background. The smooth curve shown in figure 5.7 is a result of this fit. We fixed the gaussian peak mass at 1.869 GeV. The peak width was fixed at 11 MeV obtained from the Monte Carlo simulation. The signal events was estimated to be 554 ± 33.

5.3 Monte Carlo

In order to study the production dynamics of charm particles, we need to find their acceptance in the spectrometer. We obtained the acceptance by simulating the charm particle production and their detection in the spectrometer. The simulation program is also called the Monte Carlo program.

Our Monte Carlo program has a generation routine and a digitization routine. The generation routine generated charm events using PYTHIA, a commonly used program in particle physics, which creates charm via quark-antiquark annihilation and gluon-gluon fusion. Then, we hadronize the produced quarks and gluons using the LUND model to obtain a list of the final state particles and their kinematic quantities This list is called the "truth-table" information. The digitization routine traces the particles in the truth-table through the spectrometer and simulates the responses of the detectors, according to the geometric acceptances, and the known electronic noises and efficiencies of various detectors. Finally, it converted the particle hit information into the hit wire numbers and the phototube pulse heights, identical in format to raw data events. The generated raw Monte Carlo events were reconstructed using PASS1, PASS2 and DST programs, went through the pair strip, the substripping program and the analysis program.

The Monte Carlo events up to this point have experienced what the data events did. Thus, the acceptance is the ratio of the number of reconstructed charm particles to the number of generated events stored as the truth-table information.

5.4 Drift Chamber Efficiency Hole

Because the E769 target had only about 2% interaction length, 98% of the beam particles went through the spectrometer without interacting with the target. The intense beam tended to deaden the central regions of the drift chambers, because of the space charge effect and the aging effect[35]. This drift chamber hole has an important effect on acceptance at high x_F. Because charm particles at high x_F tend to yield small opening angles for their decay tracks, they have a higher probability of going through the drift chamber hole, and of escaping detection than those at low x_F. Thus, it is important to include the efficiency corrections due to the hole in the Monte Carlo program.

The efficiency η for a drift chamber plane can be well parametrized by a two dimensional gaussian function,

$$\eta(x,y) = \eta_0(1 - \eta_h e^{-\frac{(x-x_h)^2}{\sigma_x^2} - \frac{(y-y_h)^2}{\sigma_y^2}}). \tag{5.4}$$

The quantity η_0 is the average plane efficiency far away from the hole. The relative depth of the hole is characterized by η_h. The limit $\eta_h = 1$ corresponds to zero efficiency at the center of the hole. The hole widths are described by σ_x (σ_y). The center of the hole is at (x_h,y_h). Thus, we can describe the hole using the five parameters: η_h, x_h, σ_x, y_h and σ_y.

For the E_T triggered events, hits at a drift chamber plane are due to the tracks produced in the target. The track density distribution can be approximately described by a gaussian with its center at (x_p,y_p), and widths of σ_1 and σ_2 in x and y respectively. Since the drift chamber efficiency is a function of position due to the hole, the hit distribution is given by

$$\begin{aligned} hits(x,y) &= C\eta(x,y)e^{-\frac{(x-x_p)^2}{\sigma_1^2} - \frac{(y-y_p)^2}{\sigma_2^2}} \\ &= C\eta_0(1 - \eta_h e^{-\frac{(x-x_h)^2}{\sigma_x^2} - \frac{(y-y_h)^2}{\sigma_y^2}})e^{-\frac{(x-x_p)^2}{\sigma_1^2} - \frac{(y-y_p)^2}{\sigma_2^2}} \end{aligned}$$

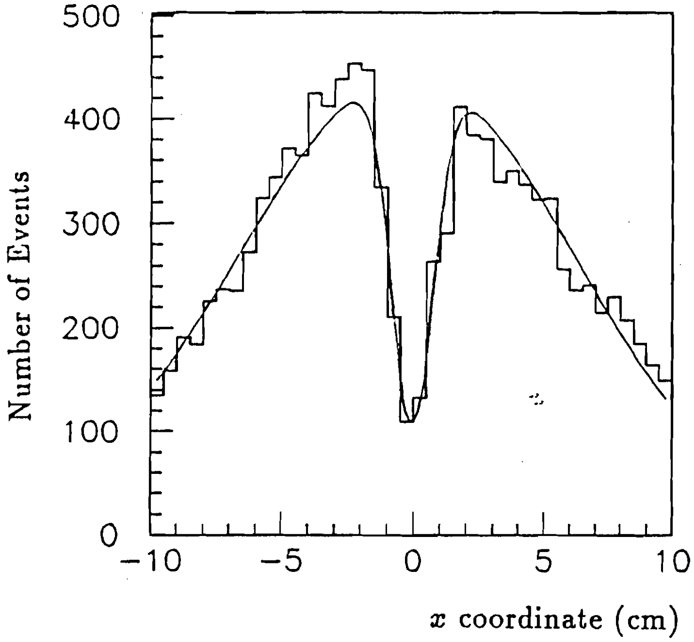

Figure 5.8: The hit distribution of the drift chamber plane D2-1x

$$= C\eta_0(e^{-\frac{(x-x_p)^2}{\sigma_1^2}-\frac{(y-y_p)^2}{\sigma_2^2}} - \eta_h e^{-\frac{(x-x_h)^2}{\sigma_x^2}-\frac{(x-x_p)^2}{\sigma_1^2}-\frac{(y-y_h)^2}{\sigma_y^2}-\frac{(y-y_p)^2}{\sigma_2^2}}). \quad (5.5)$$

where C is a constant. Because the secondary tracks have much larger angular spread than the beam tracks, the track density widths σ_1 and σ_2 are much larger than the hole widths σ_x and σ_y. Since the hit distribution center (x_p, y_p) and the hole center (x_h, y_h) are close, some of the terms in the second exponential can be neglected. More explicitly,

$$\frac{(x-x_h)^2}{\sigma_x^2} \gg \frac{(x-x_p)^2}{\sigma_1^2}$$
$$\frac{(y-y_h)^2}{\sigma_y^2} \gg \frac{(y-y_p)^2}{\sigma_2^2}.$$

The equation 5.5 becomes:

$$hits(x,y) \simeq C\eta_0(e^{-\frac{(x-x_p)^2}{\sigma_1^2}-\frac{(y-y_p)^2}{\sigma_2^2}} - \eta_h e^{-\frac{(x-x_h)^2}{\sigma_x^2}-\frac{(y-y_h)^2}{\sigma_y^2}}). \quad (5.6)$$

The hole parameters can be found by fitting the above formula to the data. To simplify this fitting process, we fit the x and y views separately. In the fit to one view, the other view was limited to a narrow region around the center of the hole. The full width 2δ was chosen much smaller than the hole width, so the projection of the hole was not obscured by the width of the slice. For example, to parametrize the hit distribution of the slice in x, we integrated $hits(x,y)$ in y from $y_h - \delta y$ to $y_h + \delta y$ to get $hits(x)$:

$$hits(x) = \int_{y_h-\delta y}^{y_h+\delta y} dy C\eta_0 (e^{-\frac{(x-x_p)^2}{\sigma_1^2}-\frac{(y-y_p)^2}{\sigma_2^2}} - \eta_h e^{-\frac{(x-x_h)^2}{\sigma_x^2}-\frac{(y-y_h)^2}{\sigma_y^2}}). \tag{5.7}$$

This expression can be simplified over its range of integration because

$$e^{-\frac{(y-y_h)^2}{\sigma_y^2}} \simeq 1.0$$

and

$$e^{-\frac{(y-y_p)^2}{\sigma_p^2}} \simeq 1.0$$

for $\delta y \ll \sigma_y \ll \sigma_2$. In other words, the exponential is nearly 1 over the range of the integration. Equation 5.7 then becomes:

$$hits(x) \quad = \quad 2C\delta y(e^{-\frac{(x-x_p)^2}{\sigma_1^2}} - \eta_h e^{-\frac{(x-x_h)^2}{\sigma_x^2}}). \tag{5.8}$$

This formula is used to determine the hole parameters in the x view. As shown in figure 5.8, the data is fit using this formula.

Because the beam was spreading out as it went through the spectrometer due to its intrinsic angular emittance and the horizontal momentum kick (in x) in the magnets, the hole tended to get larger in the downstream direction. In principle, there should be a set of parameters for each plane, but because they varied little from plane to plane within a station, it is a good approximation to use one set of averaged hole parameters η_h^i, σ_x^i, σ_x^i, x_h^i and y_h^i for the i^{th} drift chamber station where $i = 1, 4$ (there are 4 drift chamber stations).

As the beam intensity and positions changed during the run, so did the hole parameters. In order to take different running conditions into account, we evenly picked 10 tapes from a span of 3000 negative beam data tapes and obtained the their hole parameters. The variations of the hole center positions were less than 5% of the profile widths, and the fractional variations in the depths of the hole ηi_h were also less than 5%. The fractional variations in the hole widths are the largest of all. They were typically about 10%.

Drift Chamber Station	σ_x (cm)	σ_y (cm)	x_h (cm)	y_h (cm)	η_h
1	0.35	0.38	0.19	-0.69	0.77
2	0.96	0.60	0.77	-0.60	0.92
3	3.28	1.47	-2.73	-0.49	0.99
4	7.57	3.12	1.02	-0.05	1.00

Table 5.2: The standard hole parameters for the negative run from tape RI4700.

The hole parameters from tape RI4700 were close to the averaged ones and so were chosen as the standard for the negative run. They are shown in table 5.2. The widths of the hole are on the order of a centimeter. They get larger in the downstream direction. Note that σ_x is greater than σ_y. This was because the beam was bent in x direction by the magnets.

To summarize, in the Monte Carlo we parametrized the drift chamber efficiency using formula 5.4 with the hole parameters obtained from tape RI4700.

Chapter 6

Results

In this chapter, I present the x_F dependence for hadroproduction of $D^{\pm} \rightarrow K^{\mp}\pi^{\pm}\pi^{\pm}$. I explore the leading particle effect and the atomic number dependence of the x_F distribution. I also compare our results with theory and other experiments. The systematic errors due to the drift chamber hole, the E_T trigger and the Čerenkov efficiency are presented.

6.1 Effective Mass plots

We obtained a signal of 534 ± 33 decays of $D^{\pm} \rightarrow K^{\mp}\pi^{\pm}\pi^{\pm}$ as shown in figure 5.7. To obtain the x_F distribution, we divided the signal in different x_F bins with a width of 0.1. The corresponding mass plots are shown in figure 6.1. The number of signal events is listed in table 6.1. We have observed charm with a large range of x_F between 0.0 and 0.9.

x_F	0.05	0.15	0.25	0.35	0.45	0.55	0.65	0.75	0.85
# of $D^{\pm}$	118.9	179.7	122.4	88.7	39.9	11.2	9.3	0.8	1.8
Error	16.6	18.8	15.0	11.4	8.0	3.8	3.5	1.1	1.5

Table 6.1: The number of $D^{\pm}$ events in the 9 x_F bins.

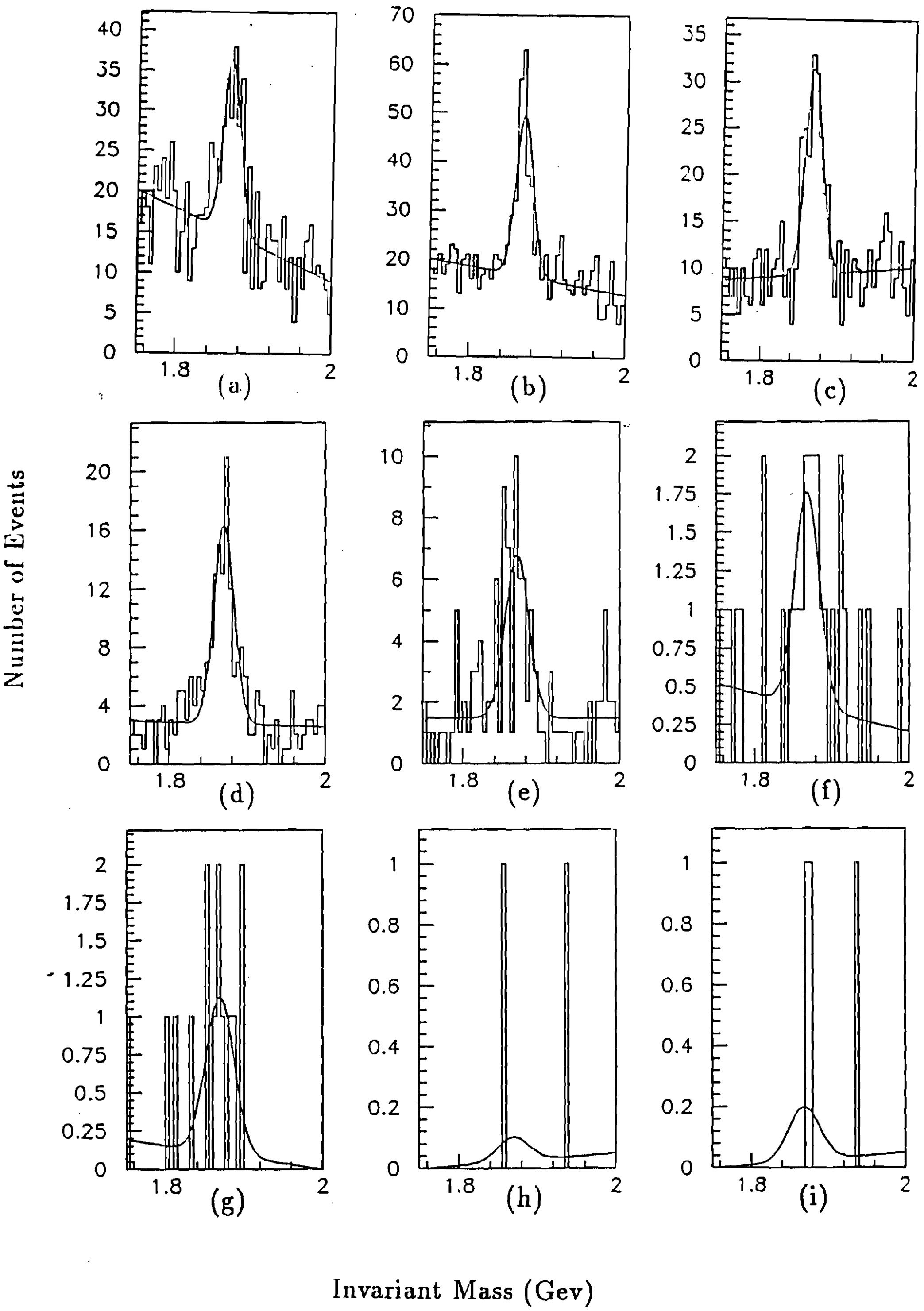

Figure 6.1: Effective mass plots of the $D^{\pm}$ at various x_F bins. (a) $0.0 < x_F < 0.1$, (b) $0.1 < x_F < 0.2$, (c) $0.2 < x_F < 0.3$, (d) $0.3 < x_F < 0.4$, (e) $0.4 < x_F < 0.5$, (f) $0.5 < x_F < 0.6$, (g) $0.6 < x_F < 0.7$, (h) $0.7 < x_F < 0.8$, (i) $0.8 < x_F < 0.9$

Note that both the signal and background decrease with x_F. Also, the widths of the gaussian signal increased with x_F from 11 MeV to 20 Mev, so we used the widths obtained from the Monte Carlo in the fit.

6.2 Acceptance

In order to obtain the x_F distribution, we need to determine the acceptance for each x_F bin from the Monte Carlo as discussed in section 5.3. The version of the Monte Carlo program we used generated the number of interactions proportionally to the thickness of the foil instead of the interaction length. To correctly calculate the acceptance integrated over all materials, we divided our target into four quadrants along the z axis. We determined the acceptance as a function of x_F for each quadrant. We also separately determined the acceptance for the interaction counter. Then, we calculated the weighted average of the acceptances from these four quadrants and the interaction counter. The weight for each quadrant is proportional to it's interaction length. For the interaction counter, the weight was taken to be proportional to the interaction length of 4.04 Be foils as determined from figure 2.9.

The acceptance for each x_F bin is listed in table 6.2. The acceptance is also plotted in figure 6.2. The result was based on 350,000 Monte Carlo events with the decay of $D^\pm \to K^\mp\pi^\pm\pi^\pm$. In order to get enough statistics for $x_F > 0.5$, about 100,000 out of these 350,000 Monte Carlo events were generated in this range.

Note that our spectrometer had a good acceptance over a large range of x_F between 0.0 and 0.9. The typical acceptance was about 4-9%. The drop in acceptance when x_F approaches 0.0 was due to the geometrical acceptance of the detector. The decline at high x_F was mainly due to the drift chamber hole and the decrease in the tracking efficiency when tracks have smaller angular spread. All errors are listed as fractions of the acceptances. Their calculations were based on the method described in the appendix A. There are enough statistics in the Monte Carlo so that the fractional statistical errors are about 2-5%. There are systematic errors due to the drift chamber hole, the E_T trigger correction and the Čerenkov correction. They are also listed in table 6.2. Their calculations are discussed in the following sections.

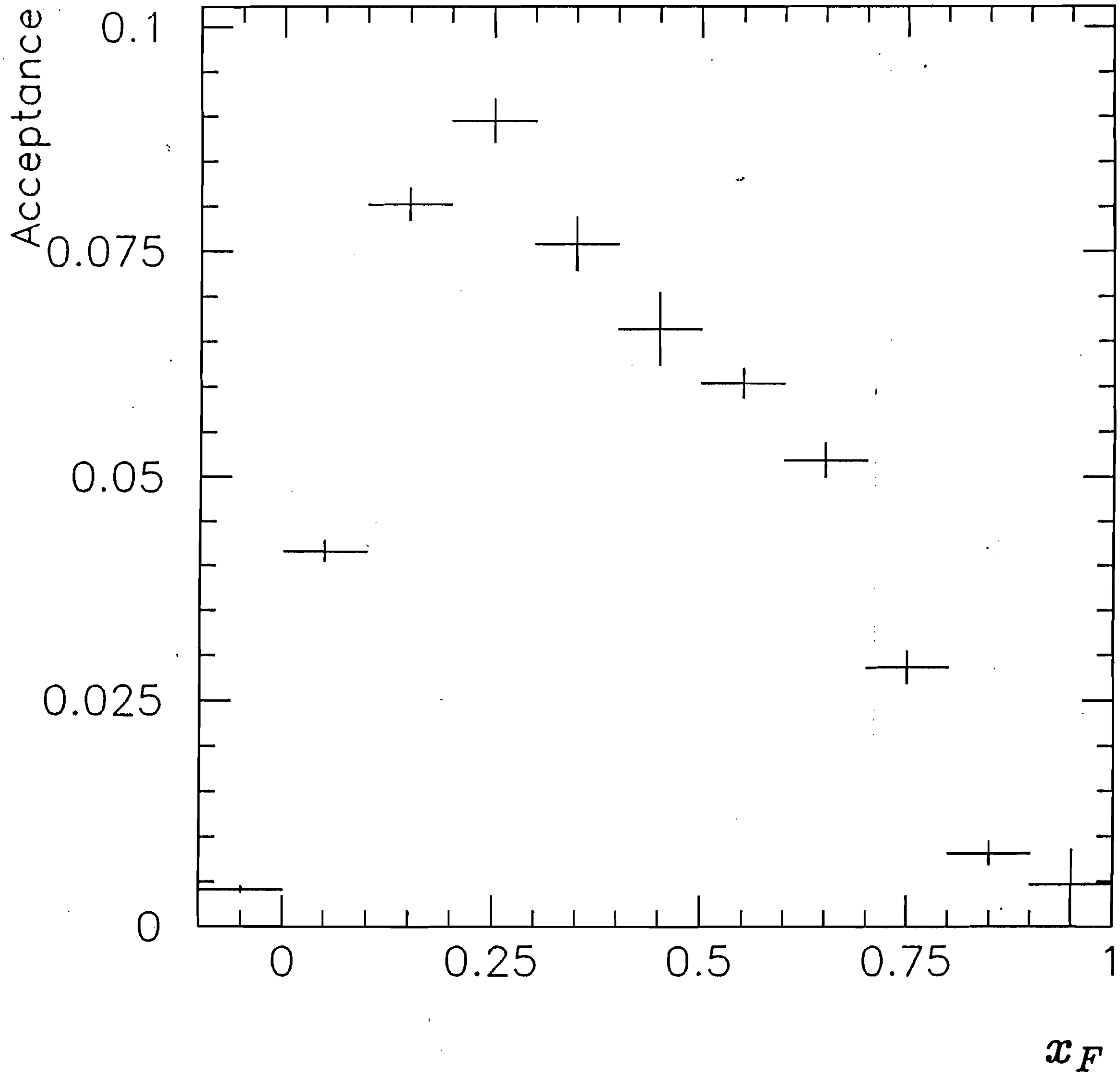

Figure 6.2: The acceptance of $D^{\pm} \rightarrow K^{\mp}\pi^{\pm}\pi^{\pm}$ as a function of x_F for $x_F > -0.1$.

x_F	Acceptance	Fract. Stat. Error	Fract. Systematic Error		
		MC	DC hole	E_T	Čerenkov
-0.05	0.0041	8.8%	2.6%	4.7%	- %
0.05	0.0416	2.8%	1.8%	2.5%	4.5 %
0.15	0.0803	2.2%	1.1%	4.0%	3.9 %
0.25	0.0896	2.8%	1.2%	3.7%	2.9 %
0.35	0.0759	3.9%	1.6%	4.5%	1.9 %
0.45	0.0664	6.6%	2.5%	2.7%	1.1 %
0.55	0.0604	2.7%	3.0%	4.0%	1.0 %
0.65	0.0519	3.7%	4.1%	11.6%	0.7 %
0.75	0.0286	6.2%	5.4%	10.5%	0.1 %
0.85	0.0082	15.7%	3.4%	7.1%	0.0 %
0.95	0.0047	80.9%	7.6%	-%	-%

Table 6.2: The Acceptance in x_F with statistical and systematic errors.

6.3 Drift Chamber Efficiency Hole Correction

Since the drift chamber hole parameters varied during the run and we were using a single set of hole parameters for the entire negative run, there is a systematic error in the acceptance due to the uncertainties of the hole parameters. The standard deviations of the hole parameters were taken as the uncertainties. As I discussed in section 5.4, the fractional uncertainties of the hole center positions and the depth of the hole were less than 5%, while the fractional variations of the hole widths were typically about 10%. Therefore, we only consider the uncertainties of the hole widths.

We generated 50,000 Monte Carlo events to evaluate the systematic error. It was calculated as the change in the acceptance when σ_x and σ_y were varied by one standard deviation. We found that the variations did not produce an observable change in the acceptance with the available statistics, so we used 10 standard deviations. Since σ_x and σ_y increased and decreased with the beam intensity, we varied them simultaneously. A decrease of 10 standard deviations corresponds to no hole, while an increase of 10 standard deviations corresponds to a hole of 2 times the normal size. Using the Monte Carlo, we obtained the acceptances for both cases. For a given x_F, if the acceptances are η_0 and η_2 for the zero hole and the big hole respectively, the systematic error was taken to be $0.1 \times (\eta_0 - \eta_2)/2$.

The systematic error is listed for each x_F range in table 6.2 and 6.4. The errors are typically between 2-7% except those (a little over 10%) with x_F between 0.6 to 0.8. They are still negligible compared with the statistical errors in the data, as discussed in section 6.6.

6.4 The E_T trigger correction

We have studied the charm efficiency of the E_T trigger as a function of x_F. We found that an increase in E_T trigger threshold (E_T^{th}) resulted in little decrease in the acceptance at low x_F but a dramatic decrease at high x_F. We can understand this from energy conservation. Both charm and non-charm contribute to the transverse energy E_T. The charm contribution is independent of x_F, because the transverse momentum of charm is independent of its longitudinal momentum. However, at high x_F, charm takes a large fraction of the total energy in an event, so there is not much energy left for non-charm particles to contribute to E_T. As a result, an increase in x_F can result in a dramatic decrease in the non-charm contribution, and hence, the total E_T. This is why we observed a dramatic decrease in the acceptance at high x_F for an increase in E_T^{th}. It is important that the Monte Carlo simulates the effect of the E_T trigger.

We found that the Monte Carlo yielded a lower average E_T than the data did. Figures 6.3 (a) and (b) show the E_T distributions for $D^\pm \rightarrow K^\mp\pi^\pm\pi^\pm$ obtained from the interaction triggers for both data and Monte Carlo. We can see that the two distributions have about the same widths, but their mean E_T values differ by 1.5 GeV with 6.5 GeV for the data and 5.0 GeV for the Monte Carlo.

In order to measure the charm efficiency of the E_T trigger from data, we made a mass plot including the signals from the decay $D^0/\bar{D}^0 \rightarrow K^\mp\pi^\pm$ in addition to the signal from the decay $D^\pm \rightarrow K^\mp\pi^\pm\pi^\pm$ mentioned above. In adding the two mass plots, the mass of the $D^0/\bar{D}^0 \rightarrow K^\mp\pi^\pm$ candidates was shifted by 4 MeV so that both mass peaks for $D^0/\bar{D}_0$ and $D^\pm$ candidates fall at the same mass. The plot is shown in

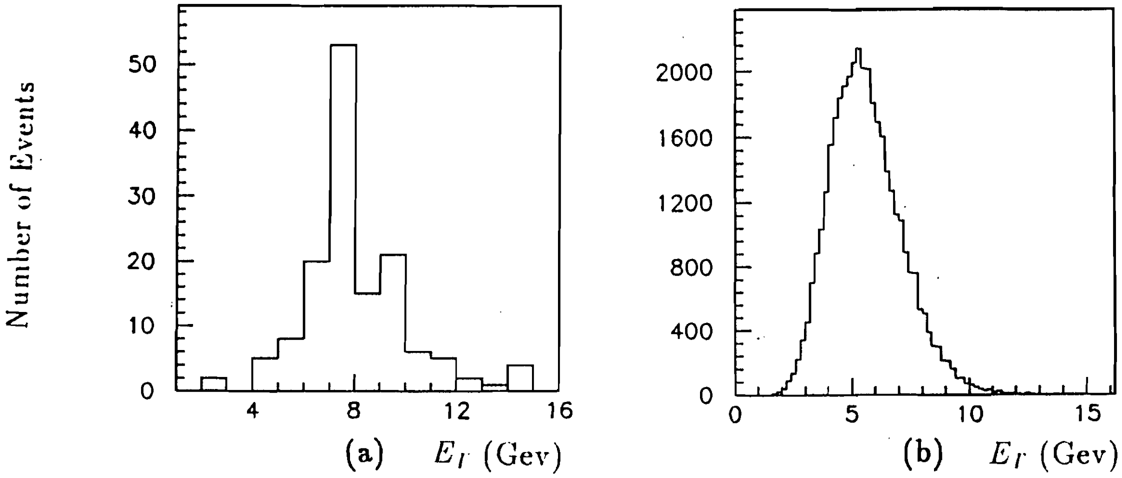

Figure 6.3: The E_T distribution of the data (a) and Monte Carlo (b)

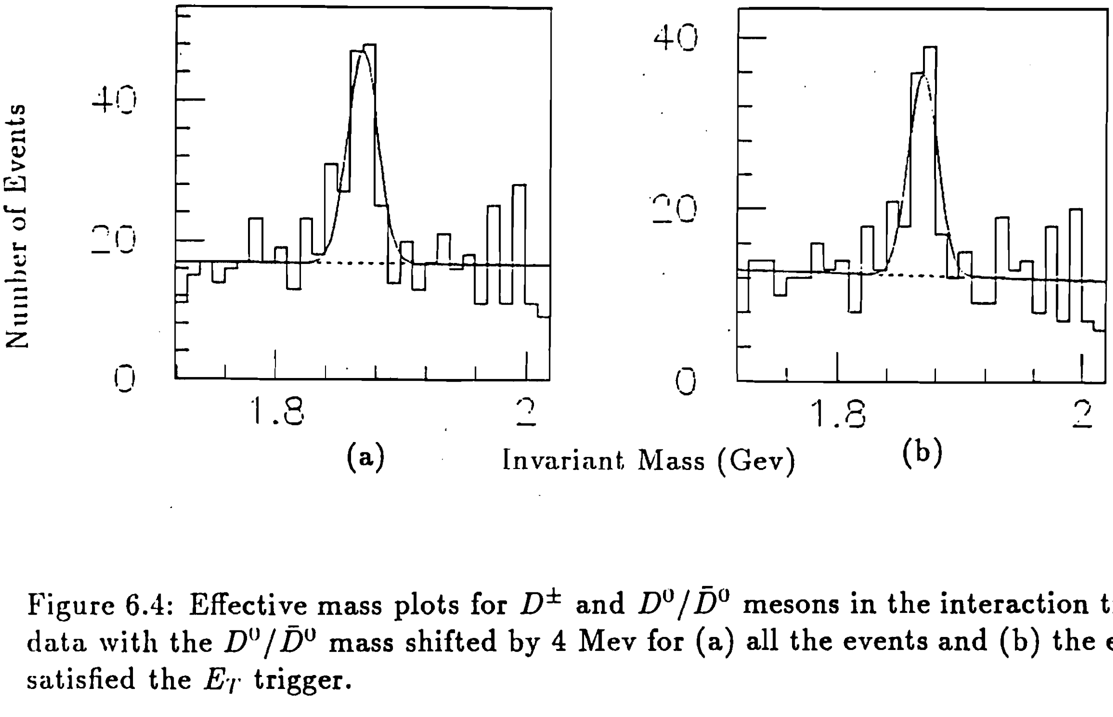

Figure 6.4: Effective mass plots for $D^{\pm}$ and $D^0/\bar{D}^0$ mesons in the interaction trigger data with the $D^0/\bar{D}^0$ mass shifted by 4 Mev for (a) all the events and (b) the events satisfied the E_T trigger.

figure 6.4 (a) from the event sample induced by the interaction triggers. The reason for including $D^0/\bar{D}^0$ decay was to increase statistical significance. The mass plot for the subset of this sample which passed the E_T trigger set at 5.5 Gev is shown in figure 6.4 (b). The efficiency is the number of charm events in (b) divided by that in (a). It was calculated to be 78±8%. The same study applied to the Monte Carlo yielded an efficiency of only about 30%. To correct for this discrepancy in getting the acceptance, we lowered the E_T^{th} in the Monte Carlo so that it yields the same charm efficiency as measured from the data. The Monte Carlo E_T^{th} was determined to be 4.0 GeV with an uncertainty of ±0.2 GeV. This uncertainty is due to ± 8% in the measured charm efficiency. This is consistent with the mean E_T difference between the data and Monte Carlo.

x_F	$\eta_{E_T>4.0GeV}(AnalysisCuts)$	$\eta_{E_T>5.5GeV}(AnalysisCuts)$
0.05	4.91 ± 0.15%	5.16 ± 0.21%
0.15	8.48 ± 0.22%	8.86 ± 0.29%
0.25	8.65 ± 0.27%	9.05 ± 0.38%
0.35	6.74 ± 0.32%	7.03 ± 0.47%
0.45	4.90 ± 0.38%	5.91 ± 0.62%
0.55	3.44 ± 0.43%	3.42 ± 0.69%
0.65	2.35 ± 0.45%	1.85 ± 0.69%
0.75	2.01 ± 0.56%	1.50 ± 0.97%

Table 6.3: The Comparison of Analysis Efficiencies for the E_T trigger thresholds of 4.0 and 5.5 GeV.

The shift in E_T^{th} not only has to yield the correct E_T efficiency η_E, but also it has to give the correct analysis efficiency. In other words, the events with $E_T > 4.0$ GeV must resemble the events with $E_T > 5.5$ GeV in terms of analysis selection criteria such as SDZ, DIP, $RATIOD$, $RATIOP$, $KPROB$.

To study the effect of the E_T^{th} shift on analysis efficiency, we express the charm acceptance (η) as the product of the E_T efficiency (η_{E_T}) and the analysis efficiency

(η_A)[1] for $E_T > E_T^{th}$. More explicitly,

$$\begin{aligned}
\eta &= \frac{N(E_T > E_T^{th})}{N(E_T > 0)} \times \frac{N(E_T > E_T^{th}.and.(AnalysisCuts))}{N(E_T > E_T^{th})} && (6.1)\\
&= \eta_{E_T} \times \eta_A && (6.2)
\end{aligned}$$

I studied the dependence of η_A on E_T^{th} for E_T^{th} at 4.0 and 5.5 GeV based on 250,000 Monte Carlo events of $D^{\pm} \rightarrow K^{\mp}\pi^{\pm}\pi^{\pm}$. The results are shown in table 6.3. For a given x_F, the two efficiencies are the same within errors, so the shift in E_T^{th} does not affect the analysis efficiency η_A. Therefore, the events with $E_T > 4.0$ GeV do assemble those with $E_T > 5.5$ GeV as far as the analysis cuts are concerned.

The systematic error in the acceptance was taken as $(\eta(E_T > 3.8GeV) - \eta(E_T > 4.2GeV))/2$ because E_T^{th} is 4.0 ± 0.2 GeV. It is shown in tables 6.2 and 6.4.

6.5 Čerenkov efficiency correction

As I discussed in section 5.3, we discovered that there was an up to 15% between the Monte Carlo and the data in the kaon Čerenkov probability distribution. We had to correct this effect in obtaining the acceptance. In principle, we could improve the Monte Carlo simulation of the Čerenkov counters. However, this was difficult because it involved accurate knowledge of the mirror reflectivities, phototube efficiencies, trajectory bend angles due to the magnetic field in C1 and so on. Instead, we used a different approach. We first measured the kaon Čerenkov efficiencies for different momentum ranges using the abundant decay mode $\phi \rightarrow K^+K^-$ for both data and Monte Carlo. They are shown in figure 6.5. The discrepancies of the data and Monte Carlo efficiencies were typically 10% but could be as large as 15%. Then, to get the acceptance, we weighed the Monte Carlo events by a correction factor depending on the kaon momentum. This correction factor (or weight) was calculated as the ratio of the data efficiency to the Monte Carlo efficiency.

The systematic error associated with this correction was estimated using the uncertainty on each weight. Again, I used the technique of varying each weight by

---

[1] It combines geometric, tracking and analysis cut efficiency.

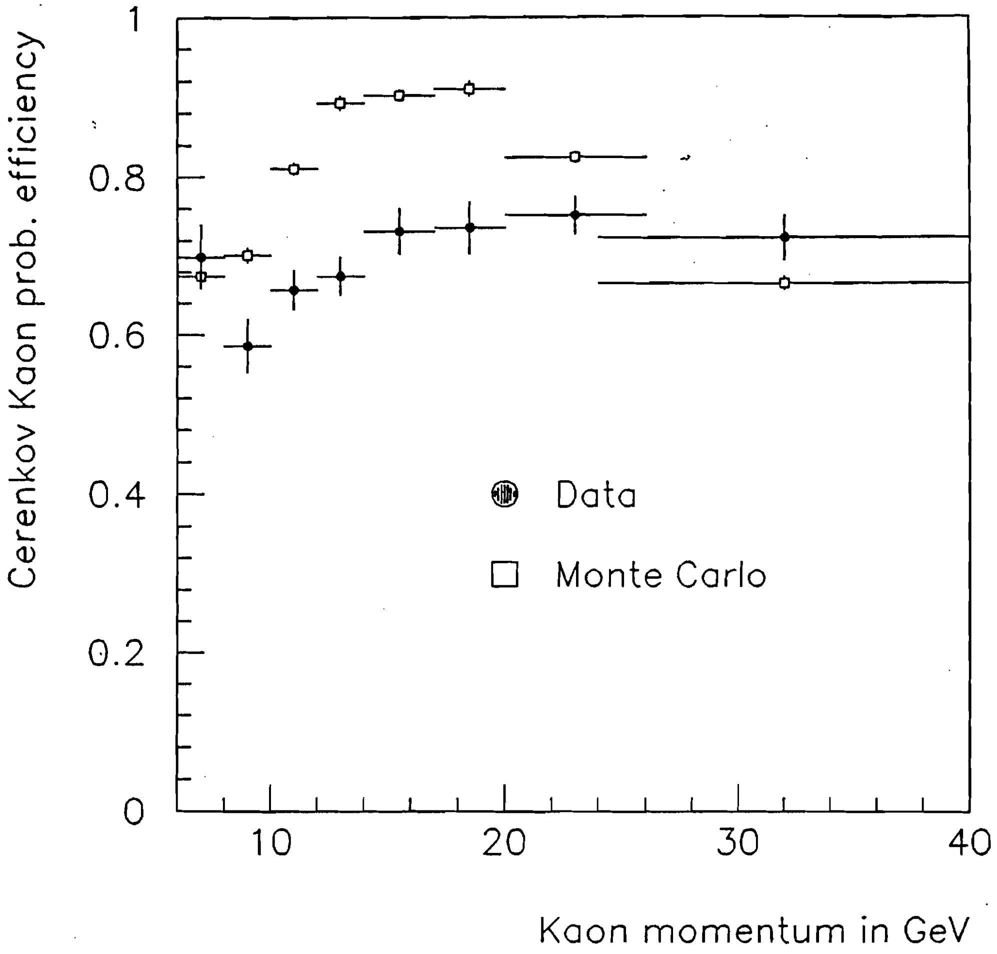

Figure 6.5: The kaon Čerenkov probability cut (> 0.13) efficiency as a function of kaon momentum.

$\pm\sigma_{weight}$. Then, I take $(\eta(weight + \sigma_{weight}) - \eta(weight - \sigma_{weight}))/2$ as the systematic error due to the Čerenkov correction. The systematic error for each x_F is listed in tables 6.2 and 6.4. They are generally small compared to other errors.

x_F	$d\sigma/dx_F$ Arb. Unit	Fract. Stat. Error Data	MC	Fract. Sys. Error DC hole	E_T	Čerenkov	Tot. Error
0.05	2856.4	13.9%	2.8%	1.8%	2.5%	4.5%	15.1%
0.15	2238.5	10.5%	2.2%	1.1%	4.0%	3.9%	12.1%
0.25	1366.7	12.2%	2.8%	1.2%	3.7%	2.9%	13.3%
0.35	1169.0	12.8%	3.9%	1.6%	4.5%	1.9%	14.2%
0.45	600.8	20.0%	6.6%	2.5%	2.7%	1.1%	21.0%
0.55	185.2	34.0%	2.7%	3.0%	4.0%	1.0%	35.0%
0.65	178.7	37.2%	3.7%	4.1%	11.6%	0.7%	38.0%
0.75	26.9	139.0%	6.2%	5.4%	10.5%	0.1%	140.0%
0.85	216.0	85.0%	15.7%	3.4%	7.1%	0.0%	86.0%

Table 6.4: The x_F distribution with statistical and systematic errors.

6.6 The x_F Distribution

We have obtained the number $S(x_F)$ of signal events for decay $D^{\pm} \rightarrow K^{\mp}\pi^{\pm}\pi^{\pm}$ and the acceptance $\eta(x_F)$ as a function of x_F. The acceptance corrected number of events $N(x_F)$ for each x_F bin is given by:

$$N(x_F) = \frac{S(x_F)}{\eta(x_F)}. \tag{6.3}$$

and

$$\frac{d\sigma}{dx_F} = CN(x_F) \tag{6.4}$$

where C is a constant. Since we are interested in the distribution in x_F, the constant C is not important. From the number of signal events integrated in all four materials and the acceptance, we obtained a differential cross section $d\sigma/dx_F$ as shown in figure 6.6. The errors shown in the plot are statistical errors only because they dominate over the systematic errors in the acceptance. The values of $N(x_F)$ are also listed in table 6.4. The fractional errors in $N(x_F)$ due to data statistics, Monte Carlo statistics and systematic effects are also listed in table 6.4.

Note that $d\sigma/dx_F$ falls rapidly with x_F. For instance, an increase in x_F from 0.1 to 0.8 results in an decrease in $d\sigma/dx_F$ by a factor of 25. Thus, there is little refractive charm production.

The x_F distribution $d\sigma/dx_F$ has been traditionally parameterized by the semi-empirical expression:

$$\frac{d\sigma}{dx_F} = C(1-|x_F|)^n \tag{6.5}$$

where C is a constant. The form of this expression was originally suggested using the counting rules[1] and Reggie pole theory[12]. It is supposed to work well at high x_F. The parameter n shows how fast $d\sigma/dx_F$ decreases with x_F. Thus, we can compare the n values with other experiments. This is discussed in section 6.8.

n	χ^2/DOF	x_F range
3.21 ± 0.24	1.13	0.0-0.9
3.35 ± 0.35	1.26	0.2-0.9
3.18 ± 0.25	1.30	0.0-0.7

Table 6.5: The χ^2 and parameter n for the x_F distribution of $D^{\pm}$ mesons.

We applied a least-squares fit to the distribution $d\sigma/dx_F$ using formula 6.5. The fit included all 9 data points with statistical errors only. The χ^2/DOF and n are listed in table 6.5. Note this formula fits well to the data giving a χ^2/DOF of about 1.2. Also note that this fit is stable because the n value did not change within errors when we used this formula to fit the first 7 data points and last 7 data points. The last two data points do not have a large effect in determining the n value because of their large relative errors.

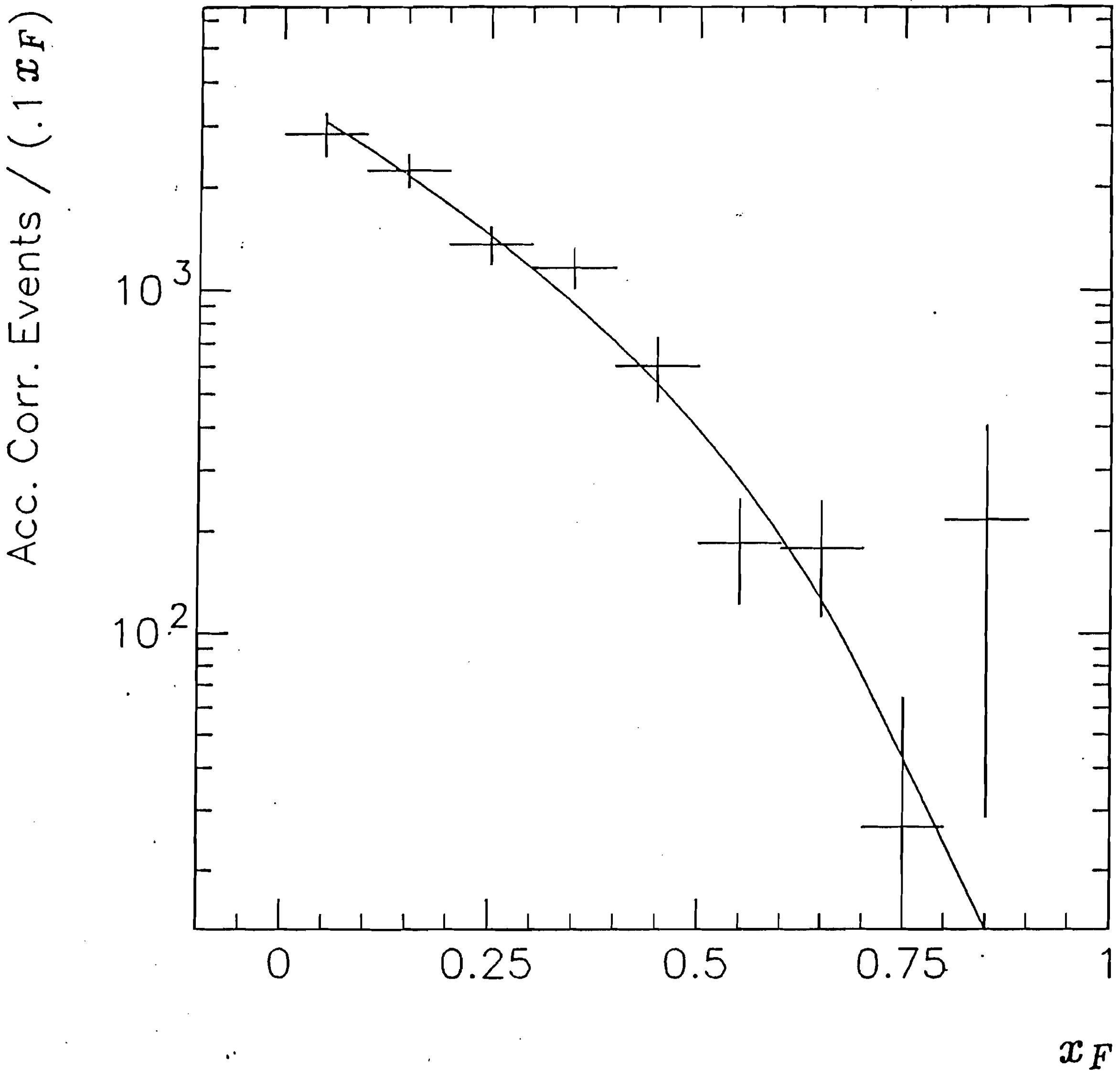

Figure 6.6: The distribution $d\sigma/dx_F$ for $D^{\pm}$ mesons

6.6.1 Leading Particle Effect

As I discussed in Chapter 1, for the charm production in $\pi^- N$ interactions, D^- is called leading because D^- can contain a d quark from the π^-, while D^+ is called non-leading because it cannot contain any quark from the π^-. Figure 6.7 and Figure 6.8 show the acceptance corrected x_F distributions for the D^- (leading) and the D^+ (non-leading) respectively. The values of the parameter n are listed in table 6.6.

fit parameters	$D^\pm$	D^-	D^+
n	3.21 ± 0.24	2.84 ± 0.31	3.50 ± 0.36

Table 6.6: The parameter n for the x_F distributions of $D^\pm$, D^- and D^+ mesons using $C(1-|x_F|)^n$.

We observed the leading D^- mesons with x_F up to 0.9 and the non-leading D^+ mesons only up to 0.7. The fits included all the available data points. There is an indication that the x_F distribution for the leading D^- mesons is more central than that for the non-leading D^+ mesons. However, the difference in n for these two distributions is $\delta n = n(D^+) - n(D^-) = 0.66 \pm 0.48$. To put an upper limit on the difference, $\delta n < 1.28$ at 90% confidence level. Thus, there is not a large difference between leading and non-leading production.

6.6.2 Atomic Number Dependence of the x_F Distributions

fit parameters	Be	Al	Cu	W
n	3.21 ± 0.44	2.39 ± 0.98	3.71 ± 0.60	3.85 ± 0.66

Table 6.7: The fit parameter n for the x_F distributions of $D^\pm$ mesons produced in Be, Al, Cu and W targets.

If the charm production and fragmentation are short distance phenomena, the x_F distribution should have little dependence on A, the atomic number. To test this hypothesis, we fit separately the x_F distributions for Be, Al, Cu and W. The

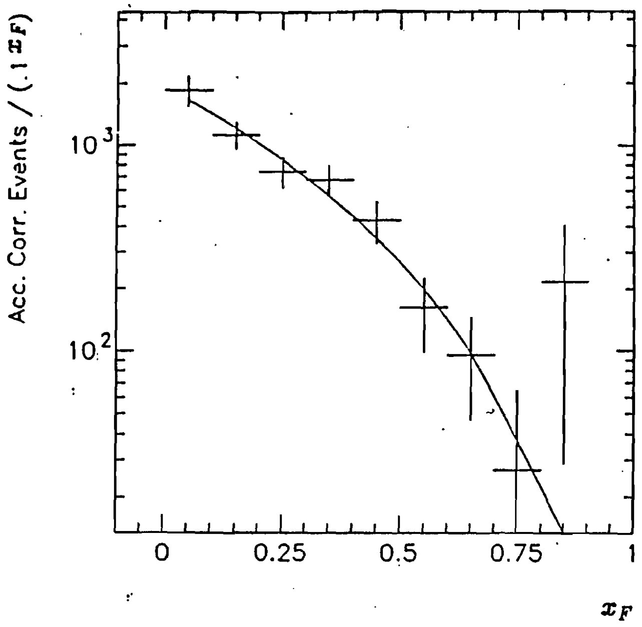

Figure 6.7: The distribution $d\sigma/dx_F$ for the leading D^- mesons

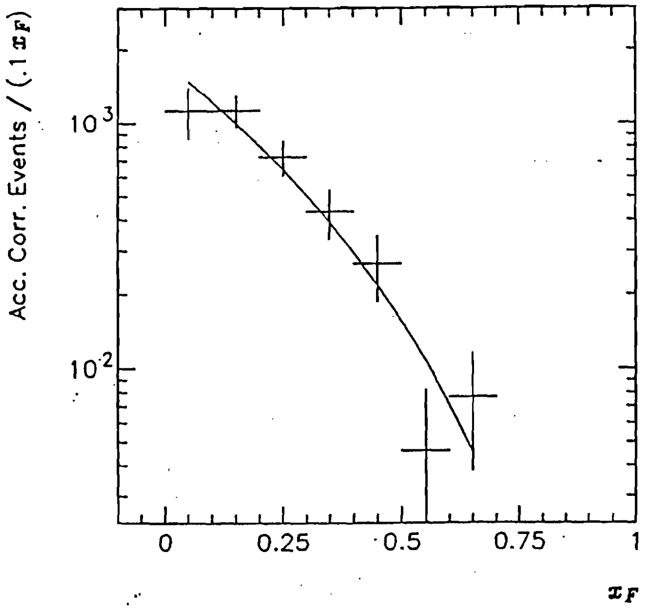

Figure 6.8: The distribution $d\sigma/dx_F$ for the non-leading D^+ mesons

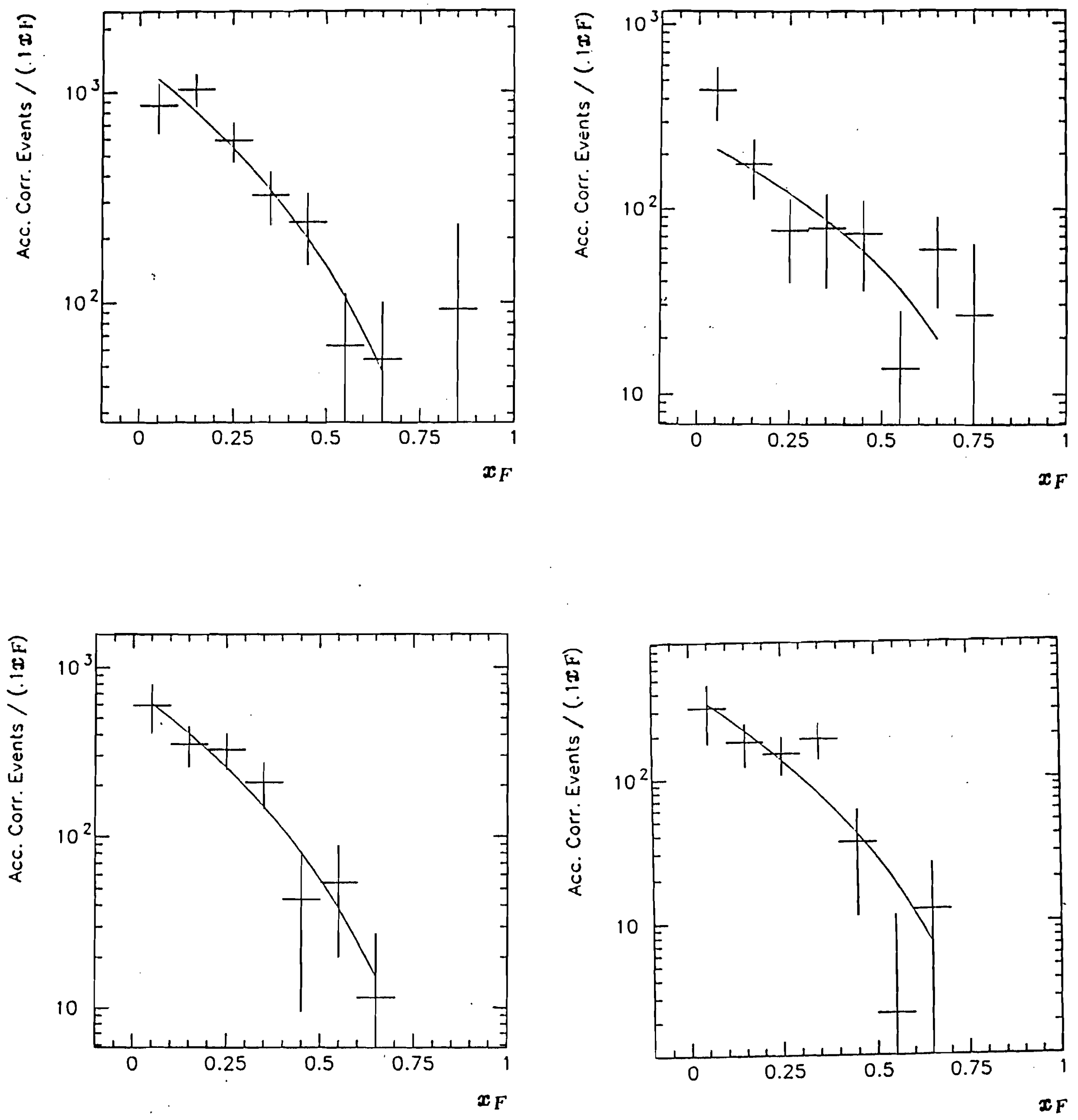

Figure 6.9: The x_F distributions fit using formula $C(1-|x_F|)^n$ in Be, Al, Cu, W targets.

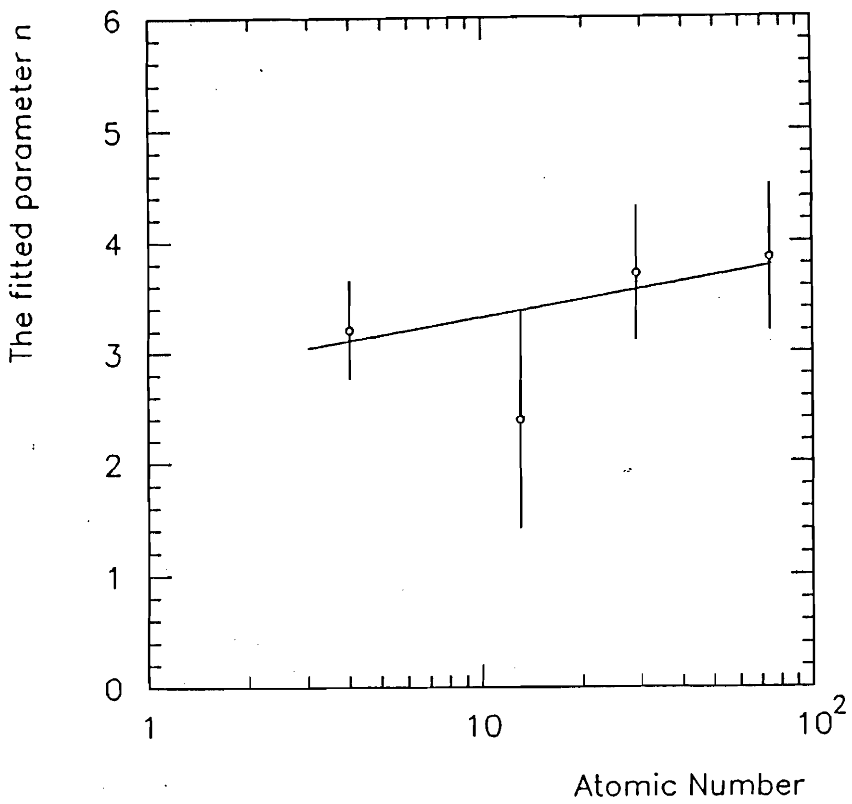

Figure 6.10: The dependence of the parameter n on atomic number A. The solid curve is a least-squares fit to the formula $n = n_0 + \alpha log A$.

distributions are shown in figure 6.9 and their n values from the fit are listed in in table 6.7. A linear least-squares fit of n values versus $logA$ gives $n = (2.79 \pm 0.33) + (0.53 \pm 0.51) logA$ with $\chi^2 = 1.20$. The plot and fit are shown in figure 6.10. Note that the error on the slope is as large as the slope itself, so the dependence on A is not significant. Thus, the charm production and fragmentation are due to short distance interactions.

6.6.3 Other Parameterizations of the x_F Distribution

As I discussed earlier in this section, the expression 6.5 is only supposed to work well at high x_F, so I attempted to use two other parameterizations given below:

$$\frac{d\sigma}{dx_F} = p_1 e^{-p_2 x_F^2 - p_3 |x_F|} \tag{6.6}$$

$$\frac{d\sigma}{dx_F} = p_1 e^{-p_2 x_F^2} (1 - |x_F|)^{p_3} \tag{6.7}$$

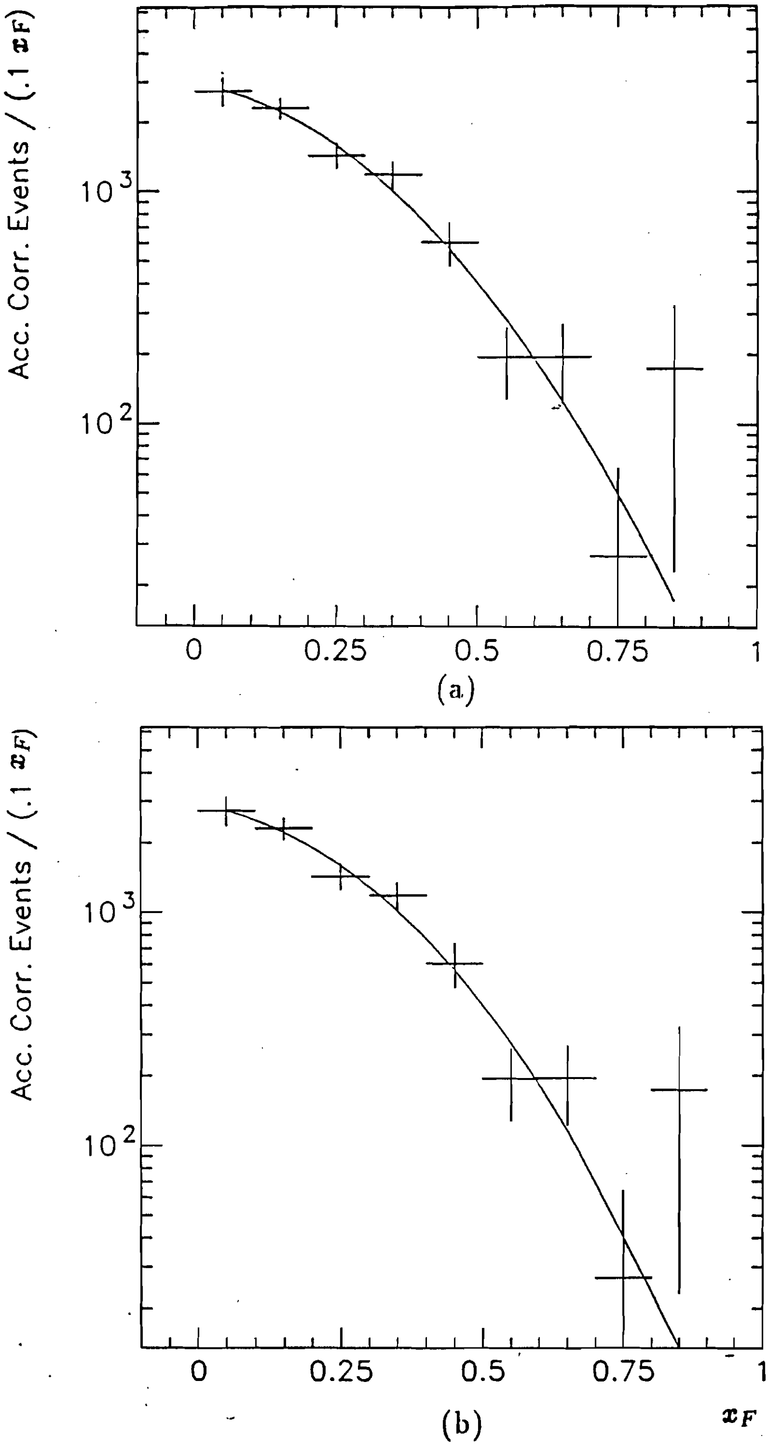

Figure 6.11: The distribution of $d\sigma/dx_F$ fit to $p_1 e^{-p_2 x_F^2 - p_3|x_F|}$ (a) and $p_1 e^{-p_2 x_F^2}(1 - |x_F|)^{p_3}$ (b) for the data

Formula	χ^2/DOF	n	p_2	p_3
$C(1-\lvert x_F\rvert)^n$	1.1	3.21 ± 0.24	-	-
$p_1 e^{-p_2 x_F^2 - p_3\lvert x_F\rvert}$	1.11	-	5.88 ± 3.56	-1.04 ± 2.24
$p_1 e^{-p_2 x_F^2}(1-\lvert x_F\rvert)^{p_3}$	1.16	-	5.28 ± 1.64	0.94 ± 0.66

Table 6.8: Results of the least-squares fit to to the data using $C(1-|x_F|)^n$, $p_1 e^{-p_2 x_F^2 - p_3|x_F|}$ and $p_1 e^{-p_2 x_F^2}(1-|x_F|)^{p_3}$ for the data.

I applied a least-squares fit to the distribution using these two formulas. The χ^2s and fit parameters are listed in table 6.8. With the given statistics, both formulas seem to give fits which are as good as formula 6.5.

6.7 Comparison with theory

To compare our result with the perturbative QCD calculations, the x_F distribution is plotted again in figure 6.12. The solid curve is the least-squares fit to the formula $C(1-|x_F|)^n$. The theoretical distribution by Dawson et al.[10] is plotted as a long dashed line with the normalization such that it gives the smallest χ^2 to the data distribution. The agreement is surprisingly good considering the the prediction used a delta function as the fragmentation function. To show the agreement quantitatively, a fit to the predicted distribution using $C(1-|x_F|)^n$ gives $n = 3.5$. This n value agrees with the measured value within one and half standard deviations, although it suggests that the predicted distribution falls more rapidly with x_F than the data does. This means that the final state charm hadrons are at least as energetic as the produced charm quarks on average. There are two possibilities. The first possibility is that the produced charm quarks can gain energy via interactions with the partons from the beam hadrons. As a result, the final state charm hadrons have higher energies than the charm quarks, e.g. $x_F > \hat{x}_F$ is possible (A symbol with a hat denotes the charm quark.). The other possibility is that the structure functions used by Dawson et al. underestimate the fraction of energetic partons.

Since the prediction using a delta function as the fragmentation function already

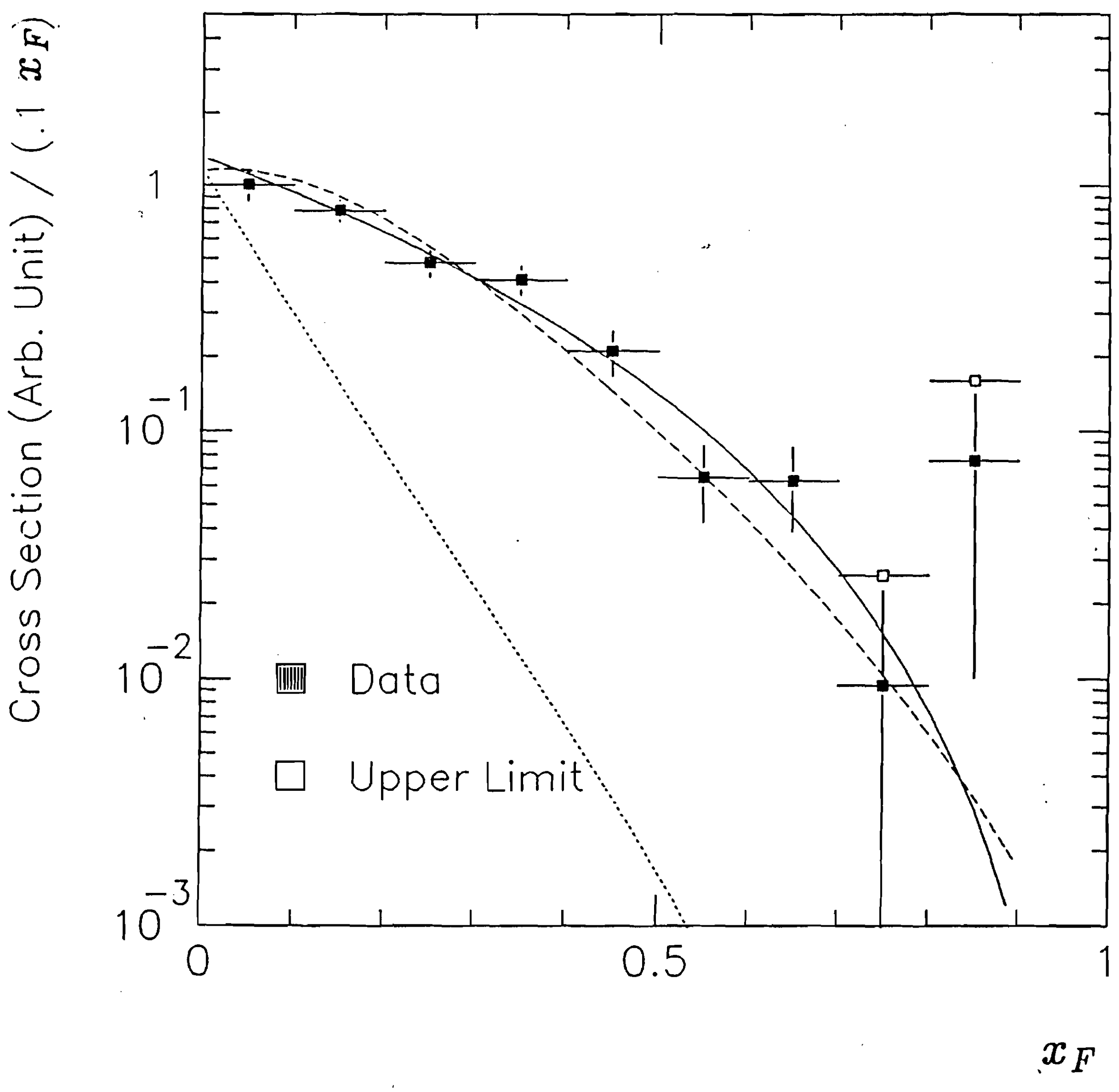

Figure 6.12: The comparison of the data $d\sigma/dx_F$ distribution with the theoretical predictions using delta function (long dashed line)[10] and Peterson's fragmentation function (short dashed line) to describe fragmentation process. The solid curve is a least-squares fit to data using formula $C(1-|x_F|)^n$.

falls more rapidly than the data does with x_F, applications of the fragmentation functions of any other form can only increase the discrepancy. To show the discrepancy quantitatively, we modified the prediction using three fragmentation functions by Kartvelishvili, Collins and Peterson used in e^+e^- experiments[17].

We derive the $d\sigma/dx_F$ from the $d\sigma(\hat{x}_F)/d\hat{x}_F$ and the fragmentation function $D_h(\zeta)$ in the following manner. The variable ζ is the fraction of the momentum carried by the final state charm hadron, so $\zeta = x_F/\hat{x}_F \leq 1$. The number of charm quarks produced between $\hat{x}_F$ and $\hat{x}_F + d\hat{x}_F$ is proportional to $d\sigma(\hat{x}_F)$. The probability for these events to fall onto the region $(\zeta,\ \zeta + d\zeta)$ is $D_h(\zeta)d\zeta = D_h(x_F/\hat{x}_F)(dx_F)/\hat{x}_F$. Hence,

$$d\sigma(x_F) = \frac{d\sigma(\hat{x}_F)}{d\hat{x}_F} d\hat{x}_F D_h(\frac{x_F}{\hat{x}_F})\frac{dx_F}{\hat{x}_F} \tag{6.8}$$

Dividing both sides by dx_F and integrating over $d\hat{x}_F$ from x_F to 1 (ζ has to be less than 1), then,

$$\frac{d\sigma(x_F)}{dx_F} = \int_{x_F}^{1} d\hat{x}_F \frac{d\sigma(\hat{x}_F)}{d\hat{x}_F}\frac{D_h(\frac{x_F}{\hat{x}_F})}{\hat{x}_F} \tag{6.9}$$

This equation converts $d\sigma/d\hat{x}_F$ to $d\sigma/dx_F$.

We numerically calculated $d\sigma(x_F)/dx_F$ using three fragmentation functions by Kartvelishvili, Collins and Peterson used by an e^+e^- experiment CLEO[17]. The modified prediction is relatively insensitive to the choice of the fragmentation functions, we only show the one using Peterson's fragmentation function as the short dashed line in figure 6.12. We normalized the modified prediction so that its maximum is the same as that using a delta function as the fragmentation function. The inclusion of any of the three structure functions resulted in a dramatic discrepancy with the data as we expected.

6.8 Comparison with Other Experiments

We compared our measured parameter n with CERN experiments LEBC-EHS[18] and ACCMOR[36]. ACCMOR used a 230 GeV π^- beam and a Cu target. They measured $d\sigma/dx_F$ of $D^\pm \to K^\mp\pi^\pm\pi^\pm$ based on 249 events[36],[37]. The comparison with our results is very appropriate since we also used π^- beam with similar energy and Cu is one of our target materials. LEBC-EHS used a hydrogen bubble chamber and a 400 GeV π^- beam. Their results were based on 57 $D^\pm$ and $D^0/\bar{D}^0$ events.

The results are listed in table 6.9. If we assume that the x_F distribution of $D^0/\bar{D}^0$ is the same as that of $D^\pm$, our result on n for $D^\pm$ agrees with that of LEBC-EHS for their combined charm signal within one standard deviation. Our result also agrees with that of ACCMOR within one and half standard deviations. I also compared our result from π^--Cu collisions with that of ACCMOR. Again, there is a good agreement.

Experiment (target)	All D	Leading	Non-leading
n (E769)(Be,Al,Cu,W) n (E769) (Cu)	3.21 ± 0.21 3.71 ± 0.60 $D^\pm$	2.84 ± 0.31 - D^-	3.50 ± 0.36 - D^+
n (LEBC-EHS)	3.8 ± 0.63 ($D^\pm$ and $D^0/\bar{D}^0$)	$1.8\pm^{0.6}_{0.5}$ (D^- and $\bar{D}^0$)	$7.9\pm^{1.6}_{1.4}$ (D^+ and D^0)
n (ACCMOR) (Cu)	$3.77\pm^{0.28}_{0.27}$ $D^\pm$	$3.23\pm^{0.30}_{0.28}$ (D^- and D^0)	$4.34\pm^{0.36}_{0.35}$ (D^+ and $\bar{D}^0$)

Table 6.9: Results for n using the formula $C(1-|x_F|)^n$ fit to the data from different experiments.

For π^- ($\bar{u}d$) beam, both D^- ($\bar{c}d$) and D^0 ($c\bar{u}$) mesons are leading because they can contain valence quarks from π^-s, while D^+ ($c\bar{d}$) and $\bar{D}^0$ ($\bar{c}u$) are not leading. However, the D^0 mesons are not leading when they come from the decay of D^{*+} mesons, since D^{*+} mesons are not leading. The non-leading D^0 mesons are about 27% of the total[36]. Thus, when we consider the leading D^0 mesons, this non-leading component of D^0 mesons should be excluded. As shown in table 6.9, both LEBC-EHS and ACCMOR combined the $D^\pm$ and $D^0/\bar{D}^0$ to study the leading particle effect. LEBC-EHS observed a large leading particle effect. Their n values for leading and non-leading D mesons differ by about 6. We did not observe a significant leading particle effect. However, in the ACCMOR results, the non-leading D^0 mesons were not excluded from the leading D^0 mesons. If we assume that the x_F distribution for $D^\pm$ and D^0 mesons are the same, and the effect of non-leading D^0 mesons is small, then they did not observe a significant leading particle effect either.

6.9 Conclusion

We have measured the x_F distribution based on the largest (to date) event sample of $D^\pm \to K^\mp\pi^\pm\pi^\pm$ produced in π^-N collisions. We observed no dramatic dependence of the distribution on atomic number. This is consistent with the perturtative QCD expectation that the charm production is due to the short range interactions of the partons. Our result is consistent with the theoretical prediction using a delta function as the fragmentation function. It appears that the fragmentation in hadroproduction is much different than in e^+e^- collisions and/or the structure functions used by Dawson et al. underestimate the fraction of energetic partons. We measured the n values for the leading (D^-) and non-leading (D^+). Our results are consistent with those measured by ACCMOR[36] but are inconsistent with the large difference in n ($\delta n = 6.1$) reported by LEBC-EHS[18].

Appendix A

Error Analysis for Correlated Data Samples

A.1 Introduction

One of the common problems we constantly deal with in particle physics is to extract number of signal events by fitting an effective mass plot with a known signal and background shape. Suppose we have $N_1 \pm \sigma_{N_1}$ signal events to start with where σ_{N_1} is the error due to the fit. The number of signal events pass (fail) a cut is N_2 (N_3). The efficiency ϵ of this cut would be N_2/N_1. However, it is tricky to evaluate the error on ϵ. Naively, N_1 is the total number of tries. The number N_2 should follow the binomial distribution with probability ϵ, so the error on N_2 would be $\sqrt{\epsilon(1-\epsilon)N_1}$ which leads to the error on the efficiency $\sigma_\epsilon = \sigma_{N_2}/N_1 = \sqrt{\epsilon(1-\epsilon)/N_1}$. However, the problem is complicated by the fact that there is an error on N_1 from the fit, so it is not a fixed number as in the case of the binomial distribution.

A.2 Error Analysis

In reality, we only know the signal and background shape, N_i [1] can only be determined from the fit to be within some errors. The binomial nature of the problem does not

---

[1] Subscript i is assumed to go from 1 to 3 in the following text unless it is denoted otherwise.

change, because the true numbers of signal events b_i are there and the only additional problem is that we have uncertainties in counting N_i. In order to find the error σ_ϵ, let me start from scratch and express N_i in terms of its true number of events b_i, the variation due to the binomial distribution δb_i and the variation due to the fit δc_i:

$$N_1 = b_1 + \delta c_1 \tag{A.1}$$

$$N_2 = \overline{b_2} + \delta b_2 + \delta c_2 \tag{A.2}$$

$$N_3 = \overline{b_3} + \delta b_3 + \delta c_3 \tag{A.3}$$

and

$$N_1 = N_2 + N_3 \tag{A.4}$$

$$b_1 = \overline{b_2} + \overline{b_3} \tag{A.5}$$

From the binomial distribution,

$$\delta b_2 = -\delta b_3 \tag{A.6}$$

so,

$$\delta c_1 = \delta c_2 + \delta c_3 \tag{A.7}$$

Note that there is no statistical variation on N_1, because N_1 is the number we start with and b_1 is a fixed number.

Let me explore the expectation values of the squares and products of the variations of δc_i and δb_i. From the binomial distribution:

$$\sqrt{\overline{\delta b_2^2}} = \sqrt{\overline{\delta b_3^2}} = \sqrt{\epsilon(1-\epsilon)b_1} \tag{A.8}$$

$\sqrt{\overline{\delta c_i^2}}$ can be determined from the fit. Because the fit is independent of the statistical fluctuations, then,

$$\overline{\delta c_j \delta b_i} = 0 \tag{A.9}$$

where i, j = 1, 3.

$$\overline{\delta c_2 \delta c_3} = 0 \tag{A.10}$$

because N_2 and N_3 do not share any common events, the errors caused by the fit should not be correlated. Equation A.10 and equation A.7 lead to

$$\overline{\delta c_1 \delta c_i} = \overline{\delta c_i^2} \tag{A.11}$$

A.3 Application

Now, I can use the tools developed in the last section to determine σ_ϵ. Let me first express the variation of the efficiency $\delta\epsilon$ in terms of δc_i and δb_i. Then I will take the mean square root.

The efficiency ϵ should be

$$\epsilon = \frac{\overline{b_2}}{b_1} \tag{A.12}$$

and its variation is expressed as:

$$\begin{aligned}\delta\epsilon &= \frac{N_2}{N_1} - \frac{\overline{b_2}}{b_1} \\ &= \frac{b_2 + \delta b_2 + \delta c_2}{b_1 + \delta c_1} - \frac{b_2}{b_1}.\end{aligned} \tag{A.13}$$

Keeping the first order terms, equation A.13 becomes:

$$\delta\epsilon = \frac{\delta b_2 + \delta c_2 - \epsilon\delta c_1}{b_1}. \tag{A.14}$$

Take the square mean of equation A.14:

$$\begin{aligned}\sigma_\epsilon^2 &= \overline{\delta\epsilon^2} \\ &= \frac{\overline{(\delta c_2 + \delta b_2)^2} + \epsilon^2\overline{\delta c_1^2} - 2\epsilon\overline{\delta c_1(\delta c_2 + \delta b_2)}}{b_1^2}\end{aligned} \tag{A.15}$$

$$
\begin{aligned}
&= \frac{(1-2\epsilon)\overline{\delta c_2^2} + \epsilon^2\overline{\delta c_1^2} + \overline{\delta b_2^2}}{b_1^2} \\
&= \frac{(1-2\epsilon)\overline{\delta c_2^2} + \epsilon^2\overline{\delta c_1^2} + \epsilon(1-\epsilon)b_1}{b_1^2} \\
&= \frac{(1-2\epsilon)\overline{\delta c_2^2} + \epsilon^2\overline{\delta c_1^2} + (1-\epsilon)b_2}{b_1^2}. \qquad \text{(A.16)}
\end{aligned}
$$

The final expression A.16 was obtained by dropping out some null cross terms (using equations A.9 and A.11).

In the extreme cases, when $\epsilon = 1$, the equation A.16 vanishes as expected, because $b_1 = b_2$, $N_1 = N_2$, $\sqrt{\overline{\delta c_1^2}}=\sqrt{\overline{\delta c_2^2}}$. When $\epsilon = 0$, the equation A.16 becomes $\overline{\delta c_2^2}/b_1^2$ which is what we expect. Since b_i is not known, equation A.12 and A.16 have to be evaluated by replacing b_1 with N_1 and $\overline{b_2}$ with N_2.

A.4 Discussion

The approach discussed in this memo is conceptually very simple. It has been very useful for the systematic error analysis due to E_T trigger, Čerenkov efficiency and the drift chamber efficiency hole for E769.

Bibliography

[1] A. Kernan and G. VanDALEN, *Charm and beauty production in strong interactions* , *Physics Reports* **106, No.6** 297 (1984)

[2] S.P.K. Tavernier, *Charmed and bottom particle production in hadronic interactions* , *Rep. Prog. Phys.* **50** 1439-1489 (1987)

[3] R.J. Morrison, *Photo- and hadroproduction of charm and beauty* , *AIP Conference Proceedings* **196** 239 (1989)

[4] R.J. Morrison and M.S. Witherell, *D MESONS* , *Annu. Rev. Nucl. Part. Sci.* **39** 183 (1989)

[5] H.M. Georgi, S.L. Glashow, M.E. Machacek, D.V. Nanopoulos, *Charmed Particles from Two-Gluon Annihilation in Proton-Proton Collisions* , *Annals of Physics* **114** 273-289 (1978)

[6] B.L. Combridge *Associated production of heavy flavour states in pp and $p\bar{p}$ interactions: some QCD estimates* , *Nuclear Physics* **B151** 429-456 (1979)

[7] V. Barger and F. Halzen, and W.Y. Keung, *Central and diffractive components of charm production* , *Physics Review D* **25** 112-119 (1982)

[8] R.K. Ellis and C. Quigg, A Pinacoteca of Cross Sections for Hadroproduction of Heavy Quarks **FN-445**, 2013.000

[9] P. Nason, S. Dawson, R.K. Ellis, *The total cross section for the production of heavy quarks in hadronic collisions* , *Nuclear Physics* **B303** 607-633 (1988)

[10] P. Nason, S. Dawson, R.K. Ellis, *The one particle inclusive differential cross section for heavy quark production in hadronic collisions* , *Nuclear Physics* **B327** 49-92 (1989)

[11] R.K. Ellis, The Status of Perturbative QCD FERMILAB-Conf-88/161-T.

[12] R. Feynman, *Very high-energy collisions of hadrons* , *Phys. Rev. Lett.* **23**, 1415 (1969).

[13] J.F. Owens, *Phys. Rev.* **D30**, 943 (1984).

[14] A.D. Martin, R.G. Roberts, and W.J. Stirling, *Phys. Rev.* **D37**, 1161 (1988).

[15] E.L. Berger, *Heavy flavor production*, ANL-HEP-CP-88-26.

[16] G. Altarelli, M. Diemoz, G. Martinelli, P. Nason, *Total cross sections for heavy flavour production in hadronic collisions and QCD* , *Nuclear Physics* **B308** 724-752 (1988)

[17] D. Bortoletto et. al., *Charm production in nonresonant* e^+e^- *annihilations at* $\sqrt{s} = 10.55 Gev$, *Physical Review D* **37** 1719 (1988)

[18] M. Aguilar-Benitex et. al., *Inclusive properties of D mesons produced in 360 GeV* $\pi^- p$ *interactions* , *Phys. Lett.* **161B** 400 (1985)

[19] M. Aguilar-Benitex et. al., *D-Meson production from 400 Gev/c* $p-p$ *interactions evidence for leading di-quarks ?* , *Phys. Lett.* **B201** 176 (1988)

[20] P. Karchin et.al. *IEEE NS-32* **612** (1985)

[21] D. Bartlett et. al., *Performance of the Cherenkov counters in the Fermilab tagged photon spectrometer facility* , *Nucl. Instr. Meth.* **A260**, 55 (1987).

[22] J. Appel V.K. Bharradwaj, M.P.Cain, D.O. Caldwell, B.H. Denby, A.M. Eisner, U.P. Joshi, R.G. Kennett, A. Lu, R.J. Morrison, D.R. Pfost, H.R. Stuber, D.J. Summers and S.J. Yellin, *A large area liquid scintillation multiphoton detector* , *Nucl. Instr. Meth.* **228**, 283 (1985).

[23] J. Appel, P. Mantsch, M. Streetman, R. Robertson, *Hadron calorimetry at the Fermilab tagged photon spectrometer facility* , *Nucl. Instr. Meth.* **A243**, 361 (1986).

[24] D. J. Summers, *A Study of the Decay $D^0 \rightarrow K^-\pi^+\pi^0$ in High Energy Photoproduction*, Ph.D., Thesis, UC Santa Barbara, (1984)

[25] J. R. Raab, *Lifetime Measurements of the Three Charmed Pseudoscaler D-Mesons*, Ph.D. Thesis, University of California at Santa Barbara, 1987.

[26] T. E. Browder, *A Study of D^0 - $\overline{D^0}$ Mixing*, Ph.D. Thesis, University of California at Santa Barbara, 1988.

[27] M. C. Gibney, *Photoproduction of Charmed Baryons*, Ph.D. Thesis, University of Colorado 1989.

[28] Robert Jedicke *E769 - Hadronic Production of Charm* , *Physics in Canada* 105-113 July (1989)

[29] D. Errede, M. Sheaff, H. Fenker, L. Lueking, P. Mantsch, *Design and Performance Characteristics of the E769 Beamline Transition Radiation Detector*, FERMILAB-Conf-88/180-E.

[30] D. Errede, M. Sheaff, H. Fenker, P. Mantsch, *A High Rate Transition Radiation Detector for Particle Identification in a Hadron Beam*, FERMILAB-Conf-89/170-E.

[31] P. Duteil, L. Gilly, R. Meunier, J. P. Stroot and M. Spighel, *High resolution gas Čerenkov Counter - DISC* , *The Review of scientific instruments* **35** 1523-1524 (1964)

[32] M. Benot, J. Litt and R. Meunier, *Cherenkov counters for particle identification at high energies* , *Nucl. Instr. Meth.* **105** 431-444 (1972)

[33] D. J. Summers, *Reconstruction of a strip geometry calorimeter using stepwise regression* , *Nucl. Instr. Meth.* **228** 290 (1985).

[34] C. Gay, S. Bracker, *The E769 multiprocessor based data acquisition system* , *IEEE Transactions on Nuclear Science,* **34** 1047 (1987)

[35] Thomas Ferbel, *Experimental Techniques in High Energy Physics*, page 79 (1987)

[36] S. Barlag et. al., *Production Properties of* D^0*,* D^+*,* D^{*+} *and* D_s^0 *in 230 Gev/c* π^- *and* K^-*-Cu Interactions* to appear in Zeitschrift für Physik C.

[37] S. Kwan, *New experimental results in hadronic charm production AIP Conference Proceedings* , **196** 262 (1989)